



3D Numerical Simulation of Scour Erosion Around An Obstacle

Wei Zhang

► To cite this version:

Wei Zhang. 3D Numerical Simulation of Scour Erosion Around An Obstacle. Fluids mechanics [physics.class-ph]. Université Paris-Est, 2019. English. NNT : 2019PESC2092 . tel-03889593

HAL Id: tel-03889593

<https://theses.hal.science/tel-03889593>

Submitted on 8 Dec 2022

HAL is a multi-disciplinary open access archive for the deposit and dissemination of scientific research documents, whether they are published or not. The documents may come from teaching and research institutions in France or abroad, or from public or private research centers.

L'archive ouverte pluridisciplinaire **HAL**, est destinée au dépôt et à la diffusion de documents scientifiques de niveau recherche, publiés ou non, émanant des établissements d'enseignement et de recherche français ou étrangers, des laboratoires publics ou privés.



École Doctorale SIE

Laboratoire d'Hydraulique Saint-Venant

Thèse

Présentée pour l'obtention du grade de DOCTEUR

DE L'UNIVERSITE PARIS-EST

par

ZHANG Wei

3D Numerical Simulation of Scour Erosion

Around an Obstacle

Spécialité : Mécanique des fluides

Soutenue le 13 Septembre 2019 devant le jury composé de:

GUILLOU Sylvain	Université de Caen Normandie	Rapporteur
THUAL Olivier	INP - Université de Toulouse	Rapporteur
GONDRET Philippe	FAST - Université Paris-Sud	Examineur
CHEVALIER Christophe	IFSTTAR - Ecole des ponts ParisTech	Examineur
PHAM-VAN-BANG Damien	INRS – Université du Québec	Directeur de thèse
NGUYEN Kim Dan	Laboratoire d'Hydraulique Saint-Venant	Co-Directeur de thèse
Uh ZAPATA Miguel	Centro de Investigación en Matemáticas	Co-encadrant



Thèse effectuée au sein du Laboratoire d'Hydraulique Saint-Venant

De l'Université Paris-Est

6, quai Watier

BP 49

78401 Chatou cedex

France

Financements: CSC (China Scholarship Council)

ENPC (École des Ponts ParisTech)

Acknowledgements

I would like to express my sincere appreciation to my supervisors Prof. Damien PHAM-VAN-BANG, Dr. Xin BAI, Prof. Kim Dan NGUYEN and Dr. Miguel UH ZAPATA for their continuous guidance, advice, support and last but not the least, their transfer of knowledge.

I would like to thank China Scholarship Council (CSC) and Ecole des Ponts ParisTech, which gave me this very great opportunity for the PhD study in France and gave me the scholarship during three years. Special thanks go to the administration and supporting staffs who have provided continuous maintenance and update on the high performance computers at Électricité de France Recherche & Développement (EDF R&D).

I also thank all my colleagues, friends and staff from Saint-Venant Hydraulics Laboratory, in particular Adrien BOURGOIN, Athanasios MOKOS, Camille JOURDAIN, Daniel MILANO, Dena KAZERANI, Florian CORDIER, Konstantin KUZNETSOV, Marissa YATES, Marina OUKACINE, Minh Hoang LE, Pablo TASSI, Roberto FRAU, Steven ALLSOP, Sofiane MARTEL, Thomas FONTY, and Vincent VIDAL for their assistance and good moment, especially at the café corner.

I also thank the interns involved in this topic, Qinjun FU, for the discussions and help in direct numerical simulations of channel flow; and Jonathan BRANS, for the report of numerical modelling of 2D flow around an obstacle.

Finally, I am thankful to my entire family, for their sacrifice, continuous support and understanding during the course of this study.

Abstract

The foundations of offshore wind turbines and bridge piers impact the surrounding flow and the sediment transport around the obstacles. This will then cause structural instability. To better understand this phenomenon, this work is built on a newly developed code (NSMP3D) using an unstructured finite volume method (UFVM) to simulate the flow and the scour process around a circular cylinder. A sigma-coordinate system is employed in order to obtain an accurate representation of the evolution of the free surface or of the interface between fluid and sediment. To avoid the checkerboard problem caused by collocated grid, a momentum interpolation scheme is used by introducing face-normal velocities at the mid-points of cell faces. Required by Large Eddy Simulation (LES), a central scheme combined with semi-implicit Adams-Bashforth scheme are proposed in this model to get second-order accuracy in time and in space. A pressure-correction projection method is employed to decouple the velocity and pressure fields.

First, this work validates second-order accuracy, numerical stability and computational efficiency and capacity of the numerical model using several benchmark test cases. The proposed model has been used for simulating 3D turbulent open-channel flows, 2D and 3D lid-cavity flows, standing wave in a closed basin, and 3D turbulent flows around a vertical cylinder. The proposed model is able to correctly reproduce the characteristic flow features in all test cases. Second, simulation of channel flow driven by suspended sediment is conducted to study the interaction of sediments and turbulence. With the increase of the settling velocity, flow turbulence is less able to keep the sediments in suspension, and the flow in the channel tends towards the laminar solution. Finally, large eddy simulations of flows around a vertical cylinder for free-slip bed, rigid bed and live bed cases are carried out. Bed erosion is simulated by solving the sediment continuity equation using a mass-conservative sand-slide algorithm and a bedload transport rate, which is based on a description of physical processes (Engelund & Fredsøe, 1976). The mean velocity profile and shear stress validate the accuracy of this model. Horseshoe vortex and lee-wake vortex shedding structure are simulated and compared with reference. The formation and the temporal development of the scour hole and other topographic bed features are successfully reproduced.

Keywords: Large Eddy Simulation (LES), Turbulent flow, free surface flow, local scour

Résumé

Les fondations des éoliennes en mer et des piliers de pont ont un impact sur l'écoulement environnant et le transport des sédiments autour des obstacles, ceci entraîne une instabilité structurelle. Pour mieux comprendre ce phénomène, ce travail présente un code nouvellement développé (NSMP3D) utilisant la méthode des volumes finis non structurés (UFVM) pour simuler l'écoulement et le processus d'affouillement autour d'un cylindre circulaire. Un système de coordonnées sigma est utilisé afin d'obtenir une représentation précise de l'évolution de la surface libre ou de l'interface entre le fluide et le sédiment. Pour éviter le problème de damier causé par une grille co-localisée, un schéma d'interpolation de moment est utilisé en introduisant des vitesses normales au niveau des points centraux des faces des cellules. Nécessaire par la Simulation des grandes échelles (SGE), un schéma centré combiné à un schéma semi-implicite Adams-Bashforth est proposé dans ce modèle pour obtenir une précision de second ordre en temps et en espace. La méthode de projection avec correction de pression est utilisée pour découpler les champs de vitesse et de pression.

Premièrement, ce travail valide l'exactitude du second ordre, la stabilité numérique, l'efficacité et la capacité de calcul du modèle numérique à l'aide de plusieurs cas de tests de référence. Le modèle proposé a été utilisé pour simuler des écoulements 3D à canaux ouverts turbulents, des écoulements 2D et 3D à cavités de couvercles, des ondes stationnaires dans un bassin fermé et des écoulements 3D turbulents autour d'un cylindre vertical. Le modèle proposé est capable de reproduire correctement les caractéristiques de l'écoulement pour tous les cas de test. Deuxièmement, une simulation du débit du chenal entraîné par les sédiments en suspension est réalisée pour étudier l'interaction des sédiments et de la turbulence. Avec l'augmentation de la vitesse de sédimentation, la turbulence de l'écoulement est moins en mesure de maintenir les sédiments en suspension et l'écoulement dans le canal tend vers la solution laminaire. Enfin, de grandes simulations d'écoulement tourbillonnaire autour d'un cylindre vertical sont respectivement effectuées pour les caisses à lit libre, à lit rigide et à lit vivant. L'érosion du lit est simulée en résolvant l'équation de la continuité des sédiments en utilisant un algorithme de glissement de sable conservateur de la masse et un taux de transport de charge du lit basé sur une description des processus physiques (Engelund & Fredsøe, 1976). Le profil de vitesse moyen et la contrainte de cisaillement valident la précision de ce modèle. La structure de délestage de vortex en fer à cheval et de vortex lee-wake sont simulées et comparées à la référence. La formation et le développement temporel

du trou de lavage et des autres caractéristiques du lit topographique sont reproduits avec succès.

Mots-clés: Simulation des Grandes échelles (SGE), Écoulement turbulent, écoulement à surface libre, affouillement local

Table of Contents

TABLE OF CONTENTS	VII
LIST OF FIGURES	VII
LIST OF SYMBOLS	XII
CHAPTER 1 INTRODUCTION	1
1.1. MOTIVATIONS AND OBJECTIVES	1
1.2. METHODOLOGIES OF THE STUDY	4
1.3. STATE OF ART	5
1.3.1. <i>Flow around a vertical cylinder on the flat bed</i>	5
1.3.2. <i>Sediment transport in the channel flow</i>	12
1.3.3. <i>Local scour around a cylinder on a mobile bed</i>	15
1.3.4. <i>Numerical modelling for scouring around a cylinder</i>	19
1.4. ORGANIZATION OF THE MANUSCRIPT	22
CHAPTER 2 NUMERICAL METHODS	25
2.1. GOVERNING EQUATIONS	25
2.1.1. <i>Non-dimensional scaling</i>	25
2.1.2. <i>Unstructured finite volume method</i>	26
2.1.3. <i>Projection method reconstruction using Adams-Bashforth scheme</i>	30
2.1.4. <i>Boundary condition</i>	31
2.1.5. <i>Parallelization</i>	33
2.2. NUMERICAL SIMULATION OF TURBULENCE	34
2.3. SIGMA-TRANSFORMATION CONFIGURATION	37
2.3.1. <i>Sigma-coordinate</i>	37
2.3.2. <i>Equations in sigma-coordinate</i>	38
2.4. SEDIMENT BED DEFORMATION	39
2.4.1. <i>Continuity equation for sediment</i>	39
2.4.2. <i>Bedload formula</i>	40
2.4.3. <i>Sand-slide model</i>	41
2.4.4. <i>Morphological update routine</i>	42
2.5. CONCLUSION	43

CHAPTER 3 VALIDATIONS OF THE HYDRAULIC MODEL	45
3.1. 3D PURE ADVECTION PROBLEM.....	45
3.1.1. <i>Cosine-Bell test</i>	46
3.1.2. <i>Zalesak's sphere test</i>	47
3.2. 2D AND 3D TAYLOR-GREEN DECAYING VORTEX.....	49
3.3. LID-DRIVEN CAVITY FLOW	51
3.4. STANDING WAVE IN A CLOSED BASIN	55
3.5. WAVE PROPAGATION OVER A SUBMERGED BAR	61
3.6. CHANNEL FLOW	63
3.6.1. <i>2D laminar channel flow</i>	63
3.6.2. <i>Turbulent channel flow</i>	66
3.7. SPEED-UP TEST.....	70
3.8. CONCLUSION.....	71
CHAPTER 4 3D SIMULATIONS OF SCOUR AROUND AN OBSTACLE.....	73
4.1. FLOW AROUND A CYLINDER ON FLAT BED WITH RIGID SURFACE.....	73
4.1.1. <i>2D simulation of flow around a cylinder at low Reynolds number</i>	73
4.1.2. <i>3D simulation of flow around a cylinder at moderate Reynolds number</i>	78
4.2. FLOW AROUND A CYLINDER ON FLAT BED WITH FREE SURFACE	86
4.2.1. <i>Small Froude number case</i>	86
4.2.2. <i>Large Froude number case</i>	90
4.3. FLOW AROUND A CYLINDER WITH SCOUR EROSION	93
4.3.1. <i>Horseshoe vortex system</i>	94
4.3.2. <i>Near wake flow</i>	96
4.3.3. <i>General erosion patterns and maximum erosion depth prediction</i>	97
4.4. CONCLUSION.....	99
CHAPTER 5 CONCLUSIONS AND PERSPECTIVES.....	101
REFERENCE.....	103
APPENDIX A. PERIODIC BOUNDARY CONDITION IN PARALLEL	
COMPUTATION.....	119
I. <i>MODIFICATION OF MEMORY STRUCTURE</i>	120
II. <i>MODIFICATION OF THE COMMUNICATION TECHNIQUE</i>	121
APPENDIX B. SUSPENDED LOAD TRANSPORT	123

<i>I. MEAN FLOW EQUATIONS.....</i>	124
<i>II. NON-DIMENSIONAL EQUATIONS</i>	125
<i>III. COMPUTATIONAL CONDITIONS.....</i>	126
<i>IV. MEAN VALUES AND TURBULENT FLUX IN THE STRATIFIED FLOWS.....</i>	127
APPENDIX C. THESIS-RELATED PUBLISHED AND REVISED PAPERS.....	135

List of figures

Figure 1.1: SeaGen (world's first commercial-scale tidal turbine commissioned in Northern Ireland's Strangford Lough in July 2008, from Marine Current Turbines Ltd.	2
Figure 1.2: Overview of the offshore wind turbine terminology, from Hoeksema (2014). 3	
Figure 1.3: An example of a bridge collapse due to scour erosion at the foundations: Loire River, Tours, 1978.....	4
Figure 1.4: Flow pattern and scour near a vertical pile, from Roulund et al. (2005).....	6
Figure 1.5: Variation in laminar horseshoe vortex number, δ is the boundary layer thickness, from Baker (1979).....	7
Figure 1.6: Mean velocity field in the vertical plane of symmetry: (a) a steady state configuration, (b) an oscillating regime configuration, (c) The evolution of the position of the critical points for case (b), from Launay (2016).	8
Figure 1.7: Flow regimes around a smooth circular cylinder, depending on the number of Reynolds, from Sumer and Fredsøe (1997).	9
Figure 1.8: sketch of hairpin vortex structures, from (Nezu et al., 1994).....	11
Figure 1.9: Single moving particle on a sloping bed. F_D is the combination of drag force and lift force, $W\sin\beta$ is the gravity force component tangential to the bed, u_τ is the friction velocity and u_b is the mean velocity of a particle, assumed to have the same direction as friction velocity, from Roulund et al. (2005).....	13
Figure 1.10: Three modes of particle transport are usually distinguished: bed-load, saltation and suspension, from McKnight and Hess (2000).	14
Figure 1.11: Development of local scour depth with time and flow velocity around a cylinder, from Melville and Chiew (1999).	15
Figure 1.12: Schematic sketch of a clear-water scour hole formation under the effect of the horseshoe vortex, from Dargahi (1990).	17
Figure 2.1: 3D sketch of geometry entities (a) 2D schematic variables stored in the cell center for collocated grid (b) Horizontal neighbor cells, and (c) Vertical neighbor cells.	27
Figure 2.2: 2D sketch of geometry entities.	27
Figure 2.3: The description of ghost cell on a solid boundary (a) general boundary cell (b) corner boundary cell	31

Figure 2.4: Configuration of the overlapping subdomains for the MPI, from Uh Zapata et al. (2014).	34
Figure 2.5: Vertical mesh before and after the sigma-transformation	37
Figure 2.6: Sand-slide algorithm: (a) an unstructured triangular bed mesh, and (b) definition of quantities used to adjust the computed bed slope.	42
Figure 2.7: Flow chart for the numerical model.	43
Figure 3.1: 3D cosine bell and Zalesak's sphere for advection term.	47
Figure 3.2: 3D contour for $\varphi = 0.9$ and the contour levels for the slice plane at $z = -0.5/\sqrt{2}$ for different resolutions.	48
Figure 3.3: Analytical and the numerical solution at the line located at $x = -0.5/\sqrt{2}$	49
Figure 3.4: Spatial (a) and temporal (b) accuracy plots. As the slopes show the position of 1 st and 2 nd accuracy order of numerical schemes.	50
Figure 3.5: Iso-surface of the Z-component of vorticity at different time.	50
Figure 3.6: Profile of horizontal midsection velocity (u) and vertical midsection velocity (w) at $Re = 100$.	52
Figure 3.7: Profile of horizontal midsection velocity (u) and vertical midsection velocity (w) at $Re = 400$.	53
Figure 3.8: 3D cavity driven flow at $Re = 1000$. (a) Unstructured mesh with refinement resolution in the corner; (b) 2D streamlines; (c) Streamwise velocity; (d) Vertical velocity; (e) 3D streamlines; (f) Profile of midsection velocity distribution.	54
Figure 3.9: Domain discretization and initial free-surface profile for the standing wave problem in a closed basin.	56
Figure 3.10: Comparison between numerical and analytical solutions of water level for: $t = T/8$, $t = T/2$, $t = 5T/8$ and $t = T$.	58
Figure 3.11: Comparisons of the free surface elevation at $(x,y) = (2.25m, 2.25m)$ and $(x,y) = (0.25m, 0.25m)$ between analytical solutions and numerical results with hydrostatic and non-hydrostatic models.	59
Figure 3.12: Comparison between numerical and analytical solutions of velocity and hydrodynamic pressure fields in the vertical section for: $t = T/8$, $t = T/2$, $t = 5T/8$ and $t = T$.	60
Figure 3.13: Comparison of the velocity and pressure between the analytical solutions (solid lines) and numerical results (dotted lines) at the position $(x,y) = (2.25m, 2.25m)$ in four different time instances (T is the period).	61
Figure 3.14: Sketch of the geometry for the Beji and Battjes test.	61

Figure 3.15: Comparisons between numerical and experimental surface elevations at $x = 10.5m$; $x = 12.5m$; $x = 13.5m$; $x = 14.5m$; $x = 15.7m$; $x = 17.3m$.	63
Figure 3.16: Mesh description for 2D Channel flow.	65
Figure 3.17: Steady streamwise velocity vector field for 2D channel flow.	65
Figure 3.18: 2D laminar channel flow: (a) Streamwise velocity profile at $x = 2.5$, $y = 0$; (b) Shear stress profile.	66
Figure 3.19: Mean streamwise velocity distribution in wall units by direct numerical simulation.	67
Figure 3.20: Iso-surface of Q -criterion field showing direct simulation of turbulent structure in the channel flows.	67
Figure 3.21: Large eddy simulation of mean streamwise velocity distribution in wall units.	69
Figure 3.22: Large eddy simulation of the turbulent channel flow: (a) Streamwise turbulence intensity using coarse mesh and (b) Reynolds stress	69
Figure 3.23: Large eddy simulation of the turbulent channel flow: (a) Iso-surface of Q -criterion field showing turbulent structure and (b) Instantaneous velocity profile.	70
Figure 3.24: Performance of the solitary wave propagation in a channel problem using different number of processors and mesh resolutions.	71
Figure 4.1: Bubble characteristics for $Re_D = 40$.	74
Figure 4.2: Evolution of (a) Reattachment length and (b) Strouhal number.	75
Figure 4.3: Time averaged pressure coefficient at different Reynolds numbers.	76
Figure 4.4: Instantaneous plot of the vortex shedding at $Re_D = 200$.	77
Figure 4.5: Mean velocity on a free slip bed at different streamwise positions (x/D) at $Re_D = 3,900$: (a) streamwise (u/U) and (b) spanwise (v/U) velocities.	77
Figure 4.6: Sketch of the geometry of the computational domain and specification of the boundary conditions.	78
Figure 4.7: (a) Detailed view of the HV coherent structure; (b) and 3D streamlines.	79
Figure 4.8: Streamline patterns in the upstream comparing the LES numerical results with experiment of Lin et al. (2003) at a time interval of $0.0769T$, where T is the period of the breakaway cycle.	81
Figure 4.9: Detailed view of the coherent structure with a HV system on a rigid bed.	82
Figure 4.10: Instantaneous streamlines on the longitudinal section upstream the cylinder at five instants in time for the rigid bed case.	83

Figure 4.11: Mean flow streamlines on the longitudinal section behind the cylinder for the rigid bed case. The direction of the flow is indicated by the arrows.	84
Figure 4.12: Mean flow streamlines on the vertical cross-sections behind the cylinder for the rigid bed case.	84
Figure 4.13: Mean streamlines on different horizontal planes for the rigid bed case.....	85
Figure 4.14: Non-dimensional bed shear stress distribution at $Re_D=46,000$	86
Figure 4.15: Velocity magnitude and streamlines for unsteady flow simulation using a free surface (left) and a rigid surface (right) for $Fr=0.075$, $Re_D=3032$ and $h/D=1.0$	87
Figure 4.16: Numerical simulation of the water surface elevation between front and side (0 to 90°) and between front and back (0 to 180°) as a function of the time using $Fr=0.075$, $Re_D=3032$ and $h/D=1.0$	88
Figure 4.17: Velocity streamlines at the back of the cylinder and water surface elevation in the horizontal and vertical direction (amplified 50 times) at different times using $Fr=0.075$, $Re_D=3032$ and $h/D=1.0$	89
Figure 4.18: Comparison of the relative variation of differential water surface elevation of cylinder relative water elevation between the numerical model and the experimental results with large Froude numbers.	91
Figure 4.19: Numerical simulation of the water surface elevation between front and side (0 to 90°) and between front and back (0 to 180°) as a function of the time using $Fr=0.44$, $Re_D=18,500$ and $h/D=1.06$	91
Figure 4.20: Velocity streamlines at the back of the cylinder and water surface elevation in the horizontal and vertical direction (amplified 5 times) at different times using $Fr=0.44$, $Re_D=18,500$ and $h/D=1.06$	92
Figure 4.21: Detailed view of the deformed mesh close to the cylinder with scouring. ...	93
Figure 4.22: Visualization of the main necklace vortices inside the scour hole for the live bed case.	95
Figure 4.23: Horseshoe vortex system in the scour hole development around the cylinder in front of the cylinder.	96
Figure 4.24: 3D streamlines of the mean flow for the live bed case.	97
Figure 4.25: 3D streamlines of the mean flow for the live bed case.	97
Figure 4.26: Scour development simulation results at time $t = 30s$, $t = 120s$, $t = 300s$ and $t = 750s$	98
Figure 4.27: Numerical (Num.) and experimental (Exp.) results of the scour depth evolution at the (a) upstream, and (b) downstream side of the cylinder for the live bed case.	99

Figure A.1: Memory structure in the original MPI code.	119
Figure A.2: Memory structure in the original MPI code.	120
Figure A.3: New memory structure for the ghost cells with potential periodic boundary.	121
Figure A.4: Schematic of Communication in original NSMP3D.	122
Figure A.5: Scheme plot of Communication process with periodic boundary condition.	122
Figure B.1: Schematic representation of the model of a turbidity current. The model preserves the most essential features of turbidity currents, i.e. the flow is entirely driven by the suspended sediments and the settling of sediments self-stratifies the flow, from Shringarpure et al. (2012).	123
Figure B.2: Mean velocity profiles in wall units. The red color corresponds to log law.	128
Figure B.3: (a) Profiles of the ratio of sediment turbulent flux to settling flux (b) profiles of Reynolds stress.	129
Figure B.4: Turbulence intensity: (a) u_{rms} ; (b) v_{rms} ; (c) w_{rms}	131
Figure B.5: Sediment concentration surface at middle value ($\bar{c} = 1.0$).	131
Figure B.6: Sediment concentration profile.	132
Figure B.7: (a) Streamwise velocity fluctuations. (b) Bed-normal velocity fluctuations. (c) Fluctuations in the concentration of sediment. Results for case 6 ($V_z = 0.026$) at $z^+ \approx 12$	133
Figure B.8: Iso-surface of $Q = 400$ for case 3 ($V_z = 0.005$) and case 6 ($V_z = 0.026$).	134

List of symbols

Roman Symbols

A	(i) area of a cell; (ii) reference point for Rouse equation
A^+	damping coefficient
c	sediment concentration
C_l, C_d, C_p	lift, drag and pressure coefficient
C_s	Smagorinsky constant
d	particle diameter
D	diameter of a cylindersssss
$dran$	random number between 0 and 1
f	vortex frequency
f_e	external forces
F_l, F_d	lift, drag force
Fr	Froude number
g	gravitational acceleration
H	reference length
h	channel depth
l_{sg}	sub-grid length scale
l_w	distance to wall from the center of a control volume
p	pressure
p_{EF}	percentage of particles in motion
q_b	bedload transport rate
Re	Reynolds number
Re_D	cylinder Reynolds number
Re_τ	friction velocity Reynolds number
St	Strouhal number
U_f^*	intermediate face normal velocity
u, v, w	streamwise, wall-normal and spanwise components of the velocity
u_b	mean velocity of a particle
U_f	face normal velocity
u_τ	friction velocity

V	(i) reference velocity; (ii) volume of a cell
V_z	settling velocity
x, y, z	streamwise, wall-normal and spanwise spatial coordinates
z_b, z_s	bottom, free surface coordinate

Greek Symbols

α	angle between flow velocity and steepest bed slope
$\alpha_{s,max}$	maximum particle concentration
β	(i) amplification factor for viscosity; (ii) angle of steepest bed slope
β_s	angle of repose of the sediment
Δ	averaged spacing of a cell
δ	boundary layer thickness
δ_{ij}	Kronecker delta
$\Delta x^+, \Delta y^+, \Delta z^+$	wall units in x, y, z direction
ζ	Rouse number
η	(i) sediment material porosity; (ii) free-surface level
θ	Shields number
θ_c	critical Shields number
θ_{c0}	critical Shields number in horizontal, 0.05
κ	Von Karman constant
μ	dynamic viscosity of fluid
μ_d	dynamic friction coefficient, 0.51
μ_s	static friction coefficient, 0.63
μ_{ss}	dynamic viscosity of solid phase
ν	Kinematic viscosity of fluid
ρ	fluid density
ρ_s	particle density
τ	Shear stress
φ	(i) the material angle of repose; (ii) Channel slope
ϕ	angle between the bed shear stress and the steepest bed slope

Conventions

$\bar{\cdot}$	filtered variable in LES regions
$\langle \cdot \rangle$	time averaged or statistical mean
\cdot^+	variable normalized in wall units
\cdot'	fluctuations from the mean
\sim	Dimensionless quantities
\cdot_∞	far-field free-stream variables

Acronyms / Abbreviations

AB2	Second-order Adams-Bashforth Scheme
BICGSTAB	Biconjugate Gradient Stabilized Method
CFD	Computational Fluid Dynamics
CFL	Courant-Friedrichs-Lewy number
DNS	Direct Numerical Simulation
EWEA	European Wind Energy Association
FVM	Finite Volume Method
HV	Horseshoe Vortex
LES	Large Eddy Simulation
NSMP3D	Navier-Stokes Multi-Phase three-Dimensional code
PPE	Pressure Poisson Equation
RAN21	Renewable Energy Policy Network for the 21 st Century
RANS	Reynolds Averaged Navier-Stokes
RHS	Right Hand Side of an equation
RK2	Second-order Rugga-Kutta Scheme
SGS	Sub-Grid Stress

Chapter 1

Introduction

1.1. Motivations and Objectives

In recent years, the world has become increasingly aware that renewable energy and energy efficiency are not only the key for addressing climate change, but also for creating new opportunities for economic development and helping billions of people without modern energy services. At the same time, the technology of extracting renewable energy from natural environment becomes popular. Modern renewable energy technology dates back to the late 20th century and is estimated to provide 10.4% of global total final energy consumption as of 2016. REN21 (2018) reported that the current European target is to provide 20% of the Europe's energy from renewable sources by 2020, among which, France was given a target to meet 23% of the energy demand from renewable sources. An estimated 17 countries generated more than 90% of their electricity with renewable sources in 2017.

Extracting energy from the marine environment is possible using following several methods: one can extract wave energy, tidal energy (both marine and fluvial) or extract the kinetic energy from the wind using offshore wind turbines. Among these methods,

1) Extraction of wind energy is one of the most efficient and inexpensive technologies. By 2017, there are 15.8 GW of installed offshore wind power capacity in the Europe. Wind energy now accounts for 18% of Europe's total installed power generation capacity (EWEA, 2017).

2) Tidal energy is highly predictable and this advantage gives tidal energy development an important potential for further electricity generation (Bahaj and Myers, 2003; Watchorn and Trapp, 2000). World energy council (2016) reported three tidal stream commercial projects accounting for 17 MW of the capacity, two are in Scotland and one in France.

The horizontal axis turbine and the cross axis turbine are the main types of marine current and offshore wind convertors. The former is of the propeller type with a horizontal axis, which is more reliable in predictable flows and usually more suitable for installation in shallow waters (20-30m water depth). Figure 1.1 shows the horizontal axial turbines in the SeaGen project in Northern Ireland in July, 2008. The cross axis turbines are of Darrieus type with a vertical axis which can operate in either direction and in both shallow and deep waters (greater than 50m depth). Both the horizontal and cross axis turbines have a significant anchorage in the seabed. Figure 1.2 shows a typical offshore wind turbine with the lower 6m of total 25m high structure slides over the top of the monopole. A J-tube is inserted to insure the scour security in the upstream side of the piles.



Figure 1.1: SeaGen (world's first commercial-scale tidal turbine commissioned in Northern Ireland's Strangford Lough in July 2008, from Marine Current Turbines Ltd.

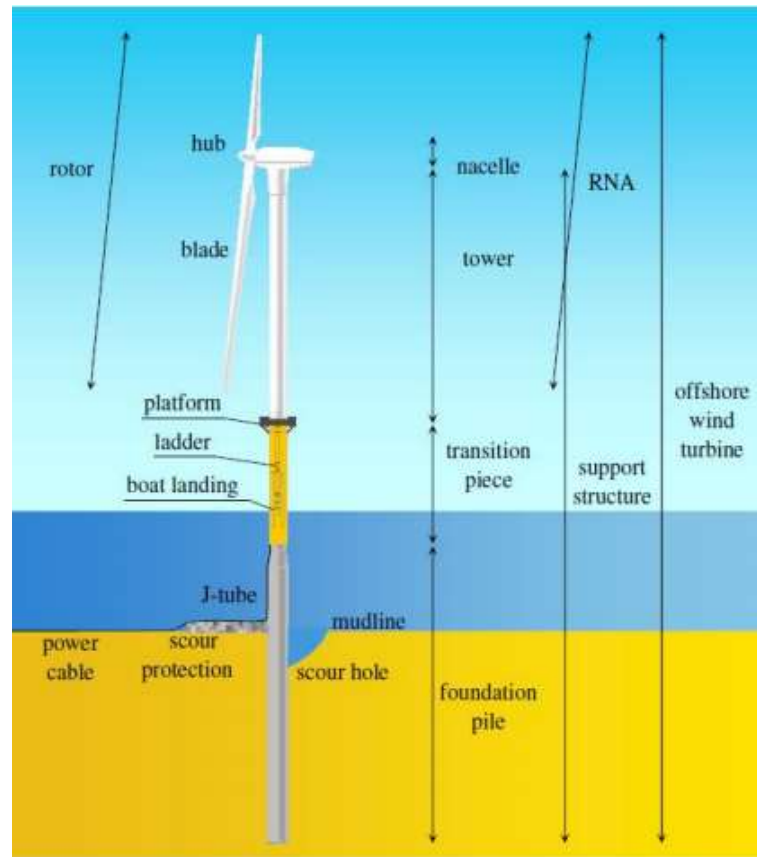


Figure 1.2: Overview of the offshore wind turbine terminology, from Hoeksema (2014).

The foundations of the offshore turbines have impacts on the surrounding morphodynamic flow and on the sediment transport around the pile which may cause structural instability. This impact has been recognized as an engineering issue. In order to avoid this phenomenon, some solutions adopted by engineers such as increasing the depth of the foundations or the pile's diameter (Matutano et al., 2013). However, these solutions are not economic.

To date, no clear information exists on the mechanisms causing the edge scour development around scour protections at offshore wind turbine foundations. More generally, the scour phenomenon encountered around marine current turbines piles and offshore wind turbines piles is similar to the one observed around the bridge piers in rivers, such as the collapse of the Wilson bridge in 1978 (see Figure 1.3). Bridge scour is one of the three main causes of bridge failure (the others being collision and overloading). It has been estimated that 60% of all bridge failures result from scour and other hydraulic-related causes (Huber, 1991). It is the most common cause of highway bridge failure in the United States, where 46 of 86 major bridge failures resulted from scour near piers from 1961 to 1976 (Levy & Salvadori, 2002).

Thus, an improvement in the scour understanding and predictions will bring advances in the design of fluvial or estuarine civil engineering (Sumer, 2014). Moreover, an accurate and efficient model, capable to solve the three-dimensional turbulent flow for localized engineering applications, is in great need.



Figure 1.3: An example of a bridge collapse due to scour erosion at the foundations:
Loire River, Tours, 1978.

Based on this background, this PhD thesis work is part of Soils, Structures and Hydraulics: Expertise and Applied Research (SSHEAR) project funded by the ANR, which is an agency intended to focus research projects on the economic and societal priorities fixed by the government. The agency funds the project and allows partnerships between different national or international organizations. For the SSHEAR project, the partners are the French Institute of Science and Technology for Transport, Spatial and networks (IFSTTAR), the laboratory FAST (CNRS), the French National Railways Company (SNCF), Cofiroute (a Vinci Group subsidiary), the Technology Research Institute (IRT Railenium) and the CEREMA. The project aims to improve our knowledge and practices on scour erosion at the foundation of transport structures.

1.2. Methodologies of the study

In this work, a numerical code called Navier-Stokes Multi-Phase three-Dimensional (NSMP3D) was used to study the 3D phenomenon of local scour of sediment transport, which was newly developed at Saint-Venant Hydraulics Laboratory (LHSV). This code is written in *Fortran90* and it is built on the successes of the 2D code (Chauchat et al, 2013; Uh

Zapata et al., 2018). It solves the Navier-Stokes equations on a collocated grid and combines the finite volume method with the sigma-transformation method. It is written in sequential or in parallel with the MPI library that can run on the multiple processors such as high performance computer (EDF Athos, Intel Xeon E 22000 CPUs).

The interest to develop this code can be explained by different reasons:

- 1) It is preferable to work on an open source code for facilities and economic reasons.
- 2) Few models gather the method of unstructured FVM and the sigma-transformation, which allows to work on free surface flow or flow over mobile bed with complex geometry.
- 3) A two-dimensional model is not sufficient to capture the phenomenon responsible for scour erosion. The long computation necessity has restricted the development of three-dimensional code, but now, both the computing power and the turbulence modelling led to reduce the computational time and enable the development of such a new model.

1.3. State of art

This part aims to describe the basic principles and different modes of sediment transport around an obstacle and the previous research of the phenomenon of scour erosion around an obstacle.

1.3.1. Flow around a vertical cylinder on the flat bed

The flow pattern will change when it encounters a solid object such as an offshore wind turbine pile or a bridge pier. There will be a three-dimensional flow separation in front of the pier, mainly due to the strong adverse pressure gradient induced by the structures presence. This flow separation generates streamlines contraction on each side of the object, leading to flow acceleration around the solid body. A boundary layer at the solid structure forms and the lee-wake vortices (usually under vortex-shedding form) are generated in the structure wake. In front of the pile, a plunging flow impacts the sediment bed similar to a jet, generating the formation of a horseshoe vortex (HV) near the bed. Figure 1.4 attempts to represent the flow pattern occurring when a flow encounters an obstacle, which is characterized by Roulund et al. (2005):

- 1) Horseshoe vortices in front of the pile;

- 2) Vortex shedding in the separation zone and wake flow downstream of the pipe;
- 3) Water surface roller and down in front of the pile.

These characters will be discussed as following subsections.

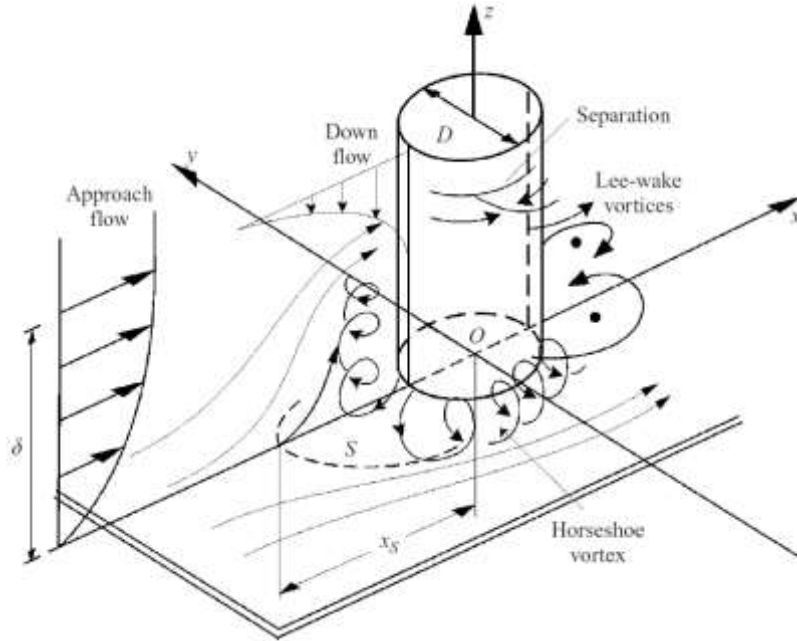


Figure 1.4: Flow pattern and scour near a vertical pile, from Roulund et al. (2005).

1.3.1.1. Oscillating Horseshoe vortex (HV) upstream of a cylinder

Different regimes can be observed upstream of the cylinder depending on the cylinder Reynolds number:

$$Re_D = \frac{\rho u_\infty D}{\mu}, \quad (1.1)$$

where D is the cylinder diameter, u_∞ is the far-field free-stream velocity, ρ is the fluid density and μ is the dynamic viscosity of the fluid. Baker (1979) is one of the first to investigate experimentally three-dimensionality of the formation of vortex around an obstacle in order to explain the erosion that occurs around the base of a cylinder. He firstly identified three steady system composed of 2, 4 and 6 vortices (Figure 1.5) according to the Reynolds number and the boundary layer thickness. The horseshoe vortex exists at the minimum achievable Reynolds number at 1000. With the increase of Re_D and δ , the number of the horseshoe vortex increases and the appearance of a chaotic system shows from a regular oscillatory motion to an unsteady irregular behavior.

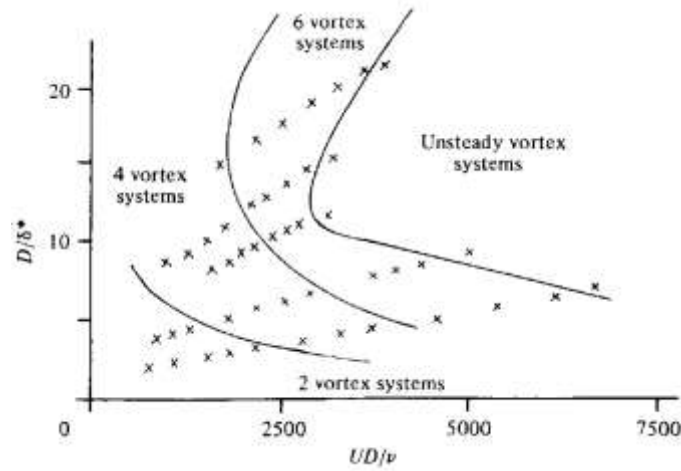


Figure 1.5: Variation in laminar horseshoe vortex number, δ is the boundary layer thickness, from Baker (1979).

Baker (1979) also realized the unsteady phenomenon of vortex shedding formed when the flow encounters a cylinder. He studied the oscillation of a laminar horseshoe vortex system, classifying them into two types: a) the oscillation due to an oscillation of the entire separated flow system upstream, and b) the oscillation due to an oscillation of the vortex core of the primary vortex. These hypotheses were used to identify the frequency of the different oscillation and the parameters to which the frequency was sensitive. Launay (2016) showed that the characteristics of the HV system only depend on three non-dimensional parameters: Reynolds number, the confinement rate of the boundary layer (h/δ), and the ratio of the wet part of the upstream face of the obstacle (W/h). The oscillation of the horseshoe vortex system at the configuration: $Re_D = 4271$, $h/\delta = 2.70$, $W/h = 0.79$ was shown in Figure 1.6a while $W/h = 1.23$ in Figure 1.6b. Four vortex cores are shown in the mean velocity field with colored streamlines representing the magnitude of the velocity, where blue is for vortex centers, red for counter-rotating vortex centers and yellow for saddle points. The green line represents the cut of the disengagement surface in the plane of symmetry. The HV system is oscillating, but the number of HV system remains the same and the vortex centers remain on the pseudo-shear layer, starting at the point of detachment and ending at the position of the main vortex V1. The areas of the saddle points show the same characteristics as the vortex centers, showing that this oscillating movement is well observed by the entire structure of the HV system. The movement of the critical points in Figure 1.6c shows a regular back and forth of the main vortex V1 upstream.

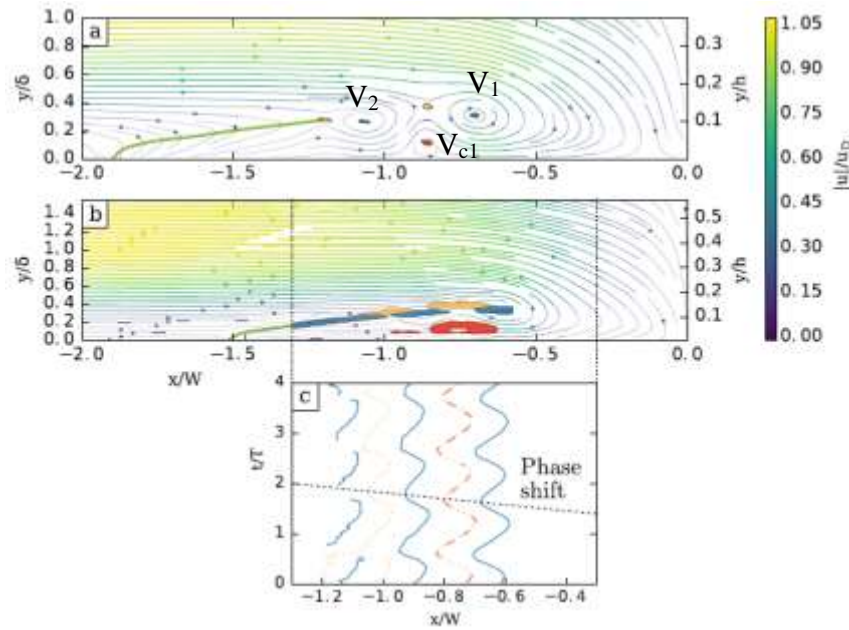
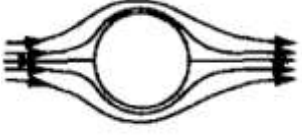
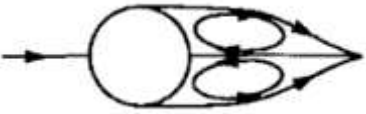



Figure 1.6: Mean velocity field in the vertical plane of symmetry: (a) a steady state configuration, (b) an oscillating regime configuration, (c) The evolution of the position of the critical points for case (b), from Launay (2016).

1.3.1.2. Vortex shedding in the near wake downstream of a cylinder

The unsteady phenomenon of vortex shedding formed can also be observed downstream of the cylinder. The periodic vortex detachment behind the obstacle, alternating each side, creates a vortex path called the von Kármán vortex street. Williamson (1989) realizes a synopsis of the different data known at that time on the formation of vortices downstream of a cylinder on a flat bed. Different regimes can be observed downstream of the cylinder depending on the Reynolds number as Figure 1.7.

(a)		No separation Creeping flow	$Re_D < 5$
(b)		A fixed pair of symmetric vortices	$5 < Re_D < 40$
(c)		Laminar vortex street	$40 < Re_D < 200$


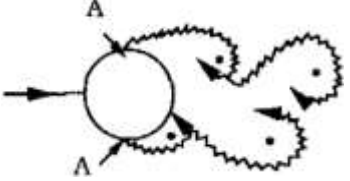
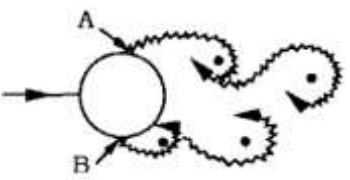
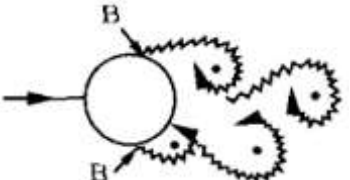
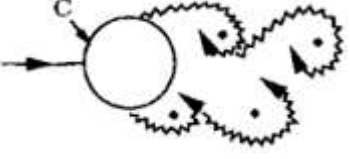

(d)		Transition to turbulence in the wake	$200 < Re_D < 300$
(e)		Wake completely turbulent. A: Laminar boundary layer separation	$300 < Re_D < 3 \times 10^5$ Subcritical
(f)		A: Laminar boundary layer separation B: Turbulent boundary layer separation; the boundary layer partly laminar partly turbulent	$3 \times 10^5 < Re_D < 3.5 \times 10^5$ Critical (Lower transition)
(g)		B: Turbulent boundary layer separation; the boundary layer partly laminar partly turbulent	$3.5 \times 10^5 < Re_D < 1.5 \times 10^6$ Supercritical
(h)		C: Boundary layer completely turbulent at one side	$1.5 \times 10^6 < Re_D < 4 \times 10^6$ Upper transition
(i)		C: Boundary layer completely turbulent at two sides	$Re_D > 4 \times 10^6$ Transcritical

Figure 1.7: Flow regimes around a smooth circular cylinder, depending on the number of Reynolds, from Sumer and Fredsøe (1997).

The vortex alternately detaches from either side of the symmetry plane. Thus, we can determine a vortex frequency (f) changing as a function of Reynolds number. The Strouhal number allows us to normalize this frequency with the flow velocity and the cylinder diameter given as below:

$$St = \frac{fu_\infty}{D}. \quad (1.2)$$

The change in pressure around the cylinder is characterized by the pressure coefficient C_p defined as:

$$C_p = \frac{p - p_\infty}{\frac{1}{2} \rho u_\infty^2}, \quad (1.3)$$

where p_∞ are the far-field free-stream pressure. Streamwise and spanwise forces applied to the cylinder are used to define respectively the lift coefficient (C_l) and the drag coefficient (C_d).

$$C_l = \frac{F_l}{\frac{1}{2} \rho U_\infty^2 A}, C_d = \frac{F_d}{\frac{1}{2} \rho U_\infty^2 A}, \quad (1.4)$$

where F_l is the lift force, F_d is the drag force, and A is the projected area of the cylinder normal to the flow.

When the frequency of the vortex shedding matches the resonance frequency of the structure, the structure will begin to resonate and the structure's movement can become self-sustaining. The failure of Tacoma Narrows Bridge (1940) and the collapse of three towers at Ferry bridge power station (1968) during high winds are examples caused by vortex shedding (Othmar H et al., 1941). Due to the periodic feature of the vortex shedding process, the lift force, drag force and pressure on the cylinder should share the same oscillating period.

Braza et al. (1986) present the numerical results for these coefficients for a Reynolds number Re_D ranging from 100 to 1000. Williamson (1989) performed experiments in a wind tunnel and investigated the discontinuities observed on the Strouhal Reynolds curve and showed that they are due to the phenomenon of oblique vortex shedding. The detaching vortex downstream of the cylinder differs from the mode called parallel vortex shedding and created waves are oblique. He explains that this phenomenon is caused by the different boundary conditions used by various authors, such as the boundary conditions used in towing tank or in a wind tunnel.

1.3.1.3. The turbulent structures around a cylinder

Vortices are often viewed as “the sinews and muscles of turbulence”. Most local vortex identification criteria are based on the kinematics implied by the velocity gradient tensor, ∇u , thereby making them Galilean invariant. Q -criterion is one of the most popularly used local criteria to show the main coherent structures present in the flow (Zhou et al, 1999). The Q -criterion defines a vortex as a coherent fluid region with positive second invariant ($Q > 0$) of the velocity gradient tensor, $A_{ij} = \partial u_i / \partial x_j$, $Q = 1/2(|\Omega_{ij}|^2 - |S_{ij}|^2) > 0$ that is the region where the magnitude of vorticity tensor, $\Omega_{ij} = 1/2(\partial u_i / \partial x_j - \partial u_j / \partial x_i)$, prevails over the magnitude of strain-rate tensor S_{ij} .

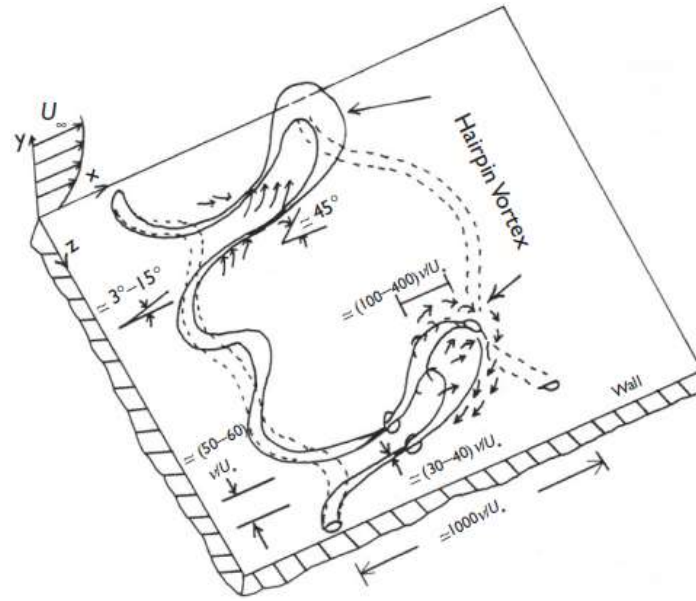


Figure 1.8: sketch of hairpin vortex structures, from (Nezu et al., 1994).

Hairpins and coherent structures have been studied and noticed in data since the 1930s, and have been since cited in thousands of scientific papers and reviews. Figure 1.8 sketches hairpin structures with a pair of counter-rotating quasi-streamwise vortices near the wall, which is a central flow feature in the development of the turbulent wall layer (Robinson, 1991). First, the long quasi-streamwise legs of the hairpin structures particularly explain the near-wall low-speed streaks. Second, passage of a rapidly lifting hairpin head and the strong pumping of fluid between the hairpin legs create a burst event with associated second quadrant velocity fluctuations. Third, Near-wall shear layers can be explained as the result of the low-speed near-wall fluid pumped up between the vortex legs encountering the high-speed free-stream fluid. Last, the spanwise spacing of low-speed streaks is associated with the spanwise width of the hairpin legs, and the characteristic 30° to 50° angle seen in the structure of wall turbulence is associated with the angle at which hairpins incline with respect to the wall. These structures are independent of the generating conditions of the wake and have a shallower inclination than the vorticity vectors (Chakraborty et al., 2005).

1.3.1.4. Free-surface flows around a cylinder

The interface with the air of the flow around a cylinder is qualified as surface free. In general, there is a run-up in front of the cylinder and a depression around the side edge and at the back of the cylinder on top (Figure 1.4). In experimental results (Graf & Yulistiyanto, 1998; Johnson & Ting, 2003), it has been observed that the free surface exhibits a variation

near the cylinder. The Froude number (Fr) of the flow mostly influences the free surface elevation close to the cylinder.

$$Fr = \frac{u}{\sqrt{gh}}, \quad (1.5)$$

where h is the channel depth, g is the gravitational acceleration. The higher the Froude number, the bigger is the observed effect on the flow around a cylinder. This number compares the kinetic energy of the fluid with its potential energy of gravity, or still the velocity of the fluid with that of the surface waves. In low Froude number channel flow, usually $Fr < 0.5$, the surface deformations are very small, thus the free surface is usually approximated as a free slip rigid-lid. In this case, the rigid-lid free-surface acts like a wall and restrain the surface-normal velocity component. Despite the limitations of the assumption, previous numerical studies have shown that a rigid free-slip wall approximation allows the prediction of many of the phenomena seen in experiments with wave-fewer interfaces (Broglia et al., 2003; Pan & Banerjee, 1995). However, for supercritical flow ($Fr > 1$), the surface-normal turbulent intensity had a tendency to increase and the effects of the surface deformation could no longer be neglected (Komori et al., 1989, Nezu et al., 1994). Thus, an accurate representation of the physical free surface is necessary.

Now the process of the sediment bed erosion in the channel flow is first illustrated in section 1.3.2 before to address the erosion around an obstacle in Part 1.3.3.

1.3.2. Sediment transport in the channel flow

1.3.2.1. The threshold of the sediment

In the channel flow, sediment transport is usually caused by the bottom friction, induced by near-bed shear flow, through particle inter granular interactions and fluid turbulent suspension (Hsu, 2004). When a flow passes over a sediment bed, shear stress is generated and can be determined from the fluid friction velocity:

$$\tau = \rho u_\tau^2, \quad (1.6)$$

where τ is the shear stress, u_τ is the fluid friction velocity. For a given solid particle, if the shear stress exceeds a threshold value, the particle is destabilized, mobilized, and the sediment transport begins. The destabilizing force generated by the flow on the particle is proportional to τd^2 , where d is the medium diameter of the particles deposited on the bed.

Shields number (Shields, 1936) is used to compare this destabilizing force with the stabilizing forces that correspond to the grains weight $\propto (\rho_s - \rho)gd^3$ as:

$$\theta = \frac{u_\tau^2}{(s-1)gd_{50}}, \quad (1.7)$$

where θ is the Shields number, $s = \rho_s/\rho$ is the specific gravity of the sediment grains, ρ_s is the particle density and g is the gravitational acceleration.

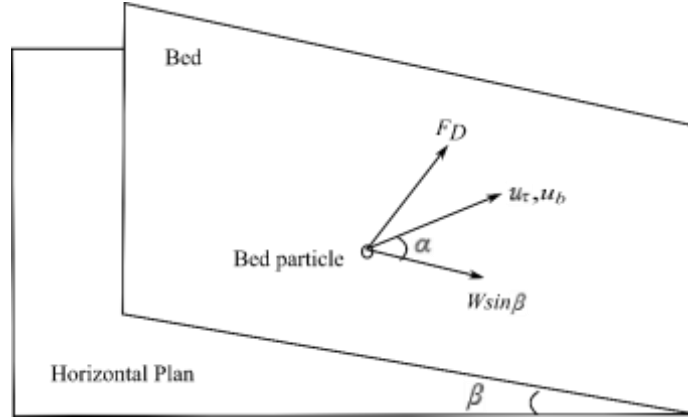


Figure 1.9: Single moving particle on a sloping bed. F_D is the combination of drag force and lift force, $W \sin \beta$ is the gravity force component tangential to the bed, u_τ is the friction velocity and u_b is the mean velocity of a particle, assumed to have the same direction as friction velocity, from Roulund et al. (2005).

For a given particle type, its threshold of motion is given by the critical Shields number θ_c with relationship to the bed slope (Engelund & Fredsøe, 1976):

$$\theta_c = \theta_{c0} \left(\cos \beta \sqrt{1 - \frac{\sin^2 \alpha \tan^2 \beta}{\mu_s^2}} - \frac{\cos \alpha \sin \beta}{\mu_s} \right), \quad (1.8)$$

where θ_{c0} is the critical Shields number for a horizontal bed, μ_s is the static friction coefficient. In practice, one can consider that $\theta_{c0} = 0.05$ (Fredsøe & Deigaard, 1992). The grains mobilization is facilitated if they are placed on an inclined sediment bed. β is defined as the angle of steepest decent calculated from the longitudinal bed elevation gradient as follows:

$$\beta = \tan^{-1} \|\nabla_H(z_b)\| = \tan^{-1} \left| \frac{\partial z_b}{\partial x}, \frac{\partial z_b}{\partial y} \right|, \quad (1.9)$$

where ∇_H is the horizontal gradient operator. β should be smaller than the angle of repose of the sediment β_s . For $\beta > \beta_s$, a pile of grains become unstable and avalanches mobilizing a

few layers of grains on the bed surface is triggered. These avalanches will continue until the angle of the slope is again equal to or lower than β_s . α is the angle between the flow-velocity vector u_b at the top of bed-load layer and the direction of the steepest bed slope. Figure 1.9 shows the simple schematic of α and β .

$$\cos \alpha = \frac{\nabla_H(z_b) \cdot u_b}{\|\nabla_H(z_b)\| \|u_b\|}. \quad (1.10)$$

1.3.2.2. The different modes of sediment transport

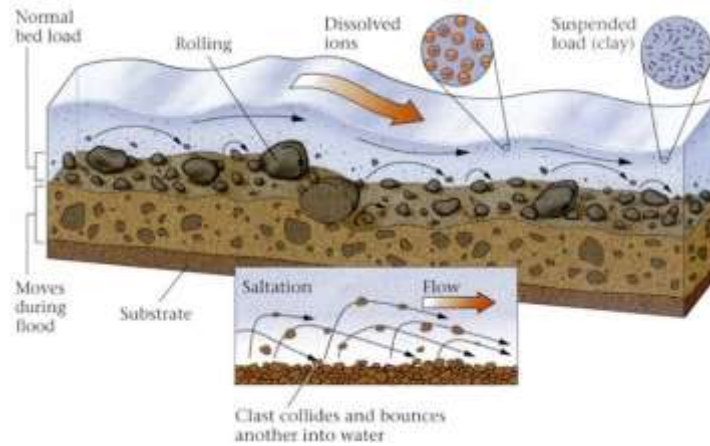


Figure 1.10: Three modes of particle transport are usually distinguished: bed-load, saltation and suspension, from McKnight and Hess (2000).

Usually, shown as Figure 1.10, three modes of particle motion are distinguished: (1) Rolling and sliding motion (2) saltation motion; and (3) suspended particle motion.

The bedload transport occurs when the local shields number exceeds critical shields number ($\theta > \theta_c$), and corresponds to the grains movement of rolling and sliding and in continuous contact with the sediment bed (McKnight and Hess, 2000). The saltation occurs when the bed-shear velocity and the local shields number decrease. The particles motion is made of successive jumps in the flow direction. Unlike bedload, the contact with the bed is not continuous but rather punctual. The jump height reached by a grain generally is within the order of magnitude of its diameter. It is generally included in the bedload definition and these two modes of transport are usually considered as a single type of particle motion. The distinction is therefore only made between bed load and suspended load. Indeed, for the bed load, the fluid puts the grains into motion horizontally whereas the suspension of the particles is acting in the vertical direction.

The suspended load occurs when the bed-shear velocity exceeds the fall velocity of the particles, the sediment particles will be lifted to a level, at which the upward turbulent forces will be of higher order than the submerged weight of the particles. Once lifted, the particles are not deposited again on the bottom. It is usually described by Rouse number (Van Rijn, 1984) :

$$\zeta = \frac{V_z}{u_\tau}, \quad (1.11)$$

Where V_z is the settling velocity of the particles in the still water. When settling velocity is smaller than friction velocity ($\zeta \ll 1$), the flow is intense enough to keep the particles in suspension. This phenomenon concerns only the smallest particles, light enough to be transported by flow turbulent velocity fluctuations.

1.3.3. Local scour around a cylinder on a mobile bed

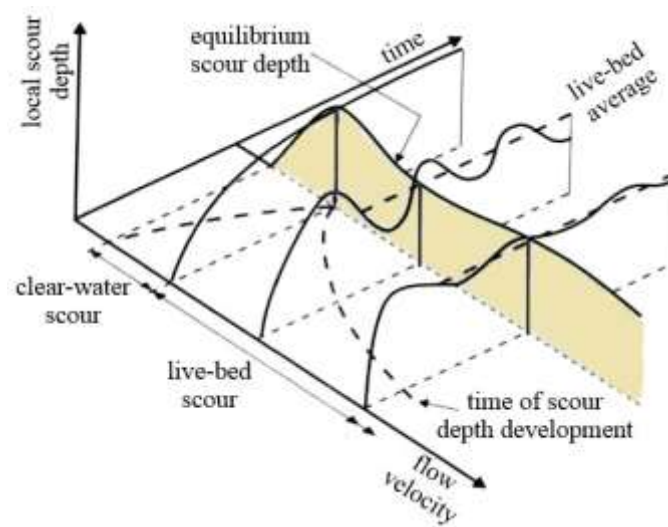


Figure 1.11: Development of local scour depth with time and flow velocity around a cylinder, from Melville and Chiew (1999).

The origin of the scouring process was attributed to the formation of the necklace-like horseshoe vortex system when the flow encounters an obstacle. A lot of research has been carried out, both experimentally and numerically to characterize the formation of these vortices. The lee-wake vortices and the horseshoe vortex (HV) lead to a local increase of the fluid bed shear stress and cause the local scour around the pier.

Local scouring is classified into the clear-water or live bed conditions depending on whether sediment transport occurs upstream of the cylinder. If the upstream flow does not erode sediment ($\theta < \theta_c$), then the scouring situation at the obstacle corresponds to clear water: the scour depth increases monotonously. Oppositely, when sediment transport (bed-load or suspended load) occurs upstream of the structure, the scouring is in the lived-bed condition. In this case, the scour hole is under dynamic equilibrium between erosion and deposition from sediment transport upstream: the scour depth presents oscillation with time.

In both cases, local scour is triggered by the horseshoe vortex at the base of the cylinder, provided that local shear stresses exceed the critical shear stress of the sediment ($\theta > \theta_c$) (Ettema et al., 2011). As the scour hole deepens, the erosive strength of the horseshoe vortex decrease until an equilibrium condition. Figure 1.11 shows the typical time evolution of the equilibrium scour depth observed in laboratory experiments of these two types of scours (Melville and Chiew, 1999). In the clear-water case, the concept of equilibrium is not clear and is still a matter of controversy (Lança et al., 2013). Whereas some authors support that equilibrium is reached randomly finite time (Melville and Chiew, 1999; Kothyari et al., 2007) and other researchers agreed that equilibrium can be reached only asymptotically and suggest that equilibrium scour depth should be estimated by extrapolation of scour depth time evolution to infinity (Sheppard et al, 2004). Manes and Brocchini (2015) proposed the relationship between the scaling of the equilibrium scour depth and the phenomenological theory of turbulence for the first time. In live bed condition, equilibrium conditions are dictated by a balance between ingoing and outgoing sediment fluxes (Melville and Chiew, 1999) and is reached very rapidly and the corresponding scour depth oscillates due to the passage of bed-forms. In both cases, the equilibrium depth corresponds to the elevation difference between the deepest point of the scour hole and the interface of the undisturbed sedimentary bed. In laboratory, under well-controlled conditions, the scour depth is of order of the pile diameter.

The detailed study of the interactions between the horseshoe vortex and the scour erosion was made by Dargahi (1990), under a clear-water regime with Reynolds number $Re_D = 39,000$.

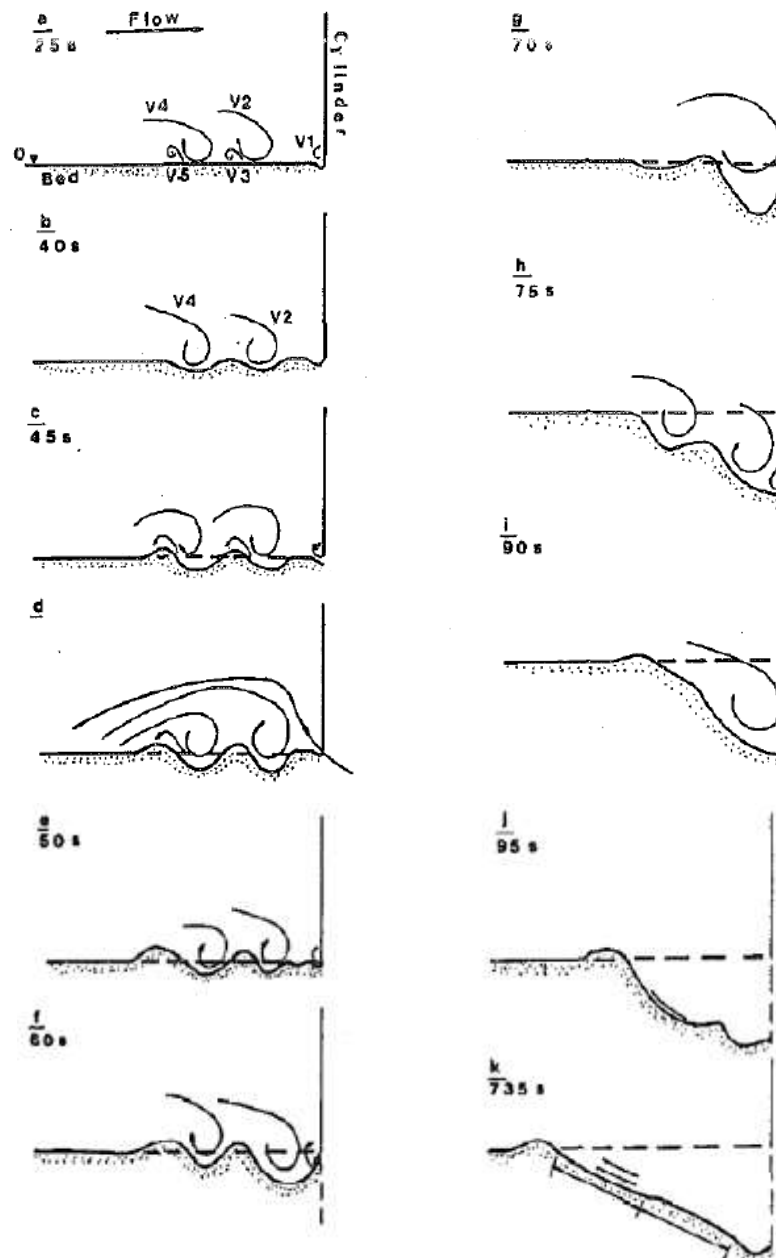


Figure 1.12: Schematic sketch of a clear-water scour hole formation under the effect of the horseshoe vortex, from Dargahi (1990).

The first scour triggered by the horseshoe vortex (V1) appears in the wake of the cylinder at the base of the pile (Figure 1.12). The scour occurs simultaneously under the other vortices (V2, V3, V4, V5) soon. Subsequently, the erosion pits forms under V2 and V4 and extend rapidly towards the upstream face of the cylinder. The sediment is eroded under the effect of V2 and V4 and fed into V3 and V5. The sediment trapped is then deposited in the form of two sediment bumps (see Figure 1.12c). The position of V1 is almost fixed over time, while the vortices V2, V3, V4 and V5 were oscillating back and forth in the plane of symmetry. As a result, the erosion holes generated by V2 and V3 and the deposition zones vary spatially

over time. When the scour depressions at the sides of the cylinder deepen, the side slopes develop into the scour hole and the whole sediment process becomes very unstable. The instability causes a further increase in rate of the transport. The depth increase of the scour hole related to V2 has an influence on the hydrodynamics. The V1 and V2 vortices are merging (Figure 1.12f and Figure 1.12g) and the slope of the associated erosion hole has a concave shape near the cylinder. The depressions under vortices V2 and V4 develop into two small slopes (Figure 1.12h). With the time development, the system tends to a single erosion hole with two different slopes of similar length (Figure 1.12k). These two slopes are the result of the two main vortices: V2 and V4. If V3 and V5 are still present, their intensity and importance for long time are greatly reduced. Zhao et al. (2010) investigated the local scour around a submerged vertical cylinder in steady currents by the experiment and numerical study. The pattern of the scour, the evolution of the scour and the HV states in the scour hole are shown. However, the detailed relationship between HV and scouring is not present.

Concerning the live bed case, the scour dynamics is also affected by the HV system and the vortex shedding, however the literature does not show a thorough investigation of the interaction between these coherent structures and the erosion dynamics such as the study by Dargahi (1990) for the clear-water scour case. To date, not to mention that the actual engineering is under complex configurations, even the case of scour around a cylinder in a steady flow is not fully understood. Comprehensive studies on the variables controlling the maximum scour depth have been conducted since the state-of-the-art paper by Breusers et al. (1977). Sumer et al. (1992) studied the scour around a vertical pile under waves or tidal condition. Debnath & Chaudhuri (2010) focused on the local scour around cylinder for clay and clay-sand mixed beds by experiments. Graf & Istiarto (2002) studied the relationship between turbulence intensity in the cylinder wake and transmission intensity of the sediment. It is found that the increase of turbulence intensity could enhance the erosion and transmission intensity of the sediment. It has recently been observed that, in a clear-water case, the vortex-shedding erosion triggering condition is weaker than that for the HV. In that case, for a small range of flows, the erosion is mainly related to the vortex-shedding downstream of the cylinder but not the horseshoe vortex in front of it (Lachaussee et al., 2018).

1.3.4. Numerical modelling for scouring around a cylinder

Due to the spatial scale of real situation or the complex physics involved in sediment transport process near structures and the capacity of computing power, traditional numerical efforts devoted to the geophysical flow problems, are usually confined into 2D modelling and hydrostatic approaches (Wu, 2004; Horvat et al., 2015). These models can provide rough estimation for future scenarios but lack the capability to handle with 3D real conditions of near-field flows at large scale, at tri-dimensionality and the non-hydrostatic expense. By definition, they are not able to capture vertical velocity effect or 3D coherent structures of the flows, which are fundamental to explain scouring processes (Dargahi, 1990). In addition, their turbulence model are mainly based on Reynolds averaging method which is not well-suited for capturing large coherent structure (Zhu et al., 2013). With the development of high performance computer, nowadays Large Eddy Simulation (LES) has been largely used to simulate high turbulent geophysical flows by massive parallel (Huang et al., 2018; Steijl and Barakos, 2018; Capuano et al., 2017).

In order to tackle these difficulties with actual performance of computing, this work proposes an accurate, robust and efficient solver for the incompressible Navier-Stokes equation using LES in collocated (non-staggered) unstructured grids. It's well-known that a collocated grid arrangement for incompressible flows could generate unrealistic pressure oscillations, so-called checkerboard problems, due to the pressure and velocity coupling, unless a treatment by a Momentum Interpolation Method (MIM) would be used (Rhie and Chow, 1983; Zang et al., 1994). In the past few years, finite volume methods with collocated unstructured grid have been used for both steady and unsteady flow (Kim and Choi, 2000; Jan and Sheu, 2007; Dalal et al., 2008; Liang et al., 2013). In these works, the mass fluxes were calculated by introducing a face-normal velocity, defined at the mid-point of each cell face. These mass fluxes or face-normal velocities are interpolated from the cell centers and later corrected using the pressure gradient, which is obtained by using a least squares technique. Depending on the applications, both first order interpolation (Mahesh et al., 2004; 2006; Davidson, 1996) and second order interpolation (Kim and Choi, 2000; Jan and Sheu, 2007; Dalal et al., 2008; Ducros et al., 2000) could be used.

The numerical description of scour is still difficult as any mathematical problem with flow-structure interaction in moving (sediment bed and free surface) boundaries. One well-known difficulty with regard to scour studies is the local description of flow properties close

to singularities (Baker, 1979; Dargahi, 1990; Kirkil et al., 2008; Kirkil & Constantinescu, 2010, 2015; Nishioka & Sato, 1974; Park, et al., 1998; Williamson, 1989). Indeed, due to the presence of obstacles, the flow forms a Horseshoe Vortex system upstream and a boundary layer detachment as well as complicated vortex shedding at the wake of the structure. These features significantly affect the scour as it evolves around the cylinder. Another difficulty arises when free-surface deformation could modify flow properties near the local problem.

Due to the progress in the availability of computational power, numerical studies on scour around a vertical cylinder are now well documented. However, the development of accurate and efficient models for the scour process is still very challenging when the motivation is to compute sediment transport by water directly or with a minimum of empirical parameter. First, hydrodynamic and sediment transport models are coupled such that a closure equation for the bedload estimation is required. Second, the sand-slide processes play an important role during the formation of a scour hole, thus the local bed slope and friction angle of the bed material should be incorporated in the model. Third, a mesh adaptation around the cylinder boundary is required to capture the bed deformation (Khosronejad et al., 2011, 2012). Finally, turbulence models are obviously necessary to simulate the coherent structures of flow fields with the presence of a HV system. These factors must be overcome to if better models are to be obtained.

Roulund et al. (2005) presented a major advance in simulating local scour around a vertical cylinder by using a structured finite volume code to solve the Reynolds Average Navier-Stokes (RANS) equations with a $k-\omega$ turbulence closure (where k is the turbulent kinetic energy and ω is the specific dissipation rate). Overall, their numerical results coincide with their experimental data and the study serves as reference to many studies in a lot of existing studies (Baykal et al., 2014, 2017; Stahlmann, 2013; Zhou, 2017). The work of Kirkil et al. (2008) and Kirkil & Constantinescu (2010, 2015) applied a Large-Eddy Simulation (LES) to analyze the coherent structure of flow fields with the presence of a HV system upstream and a wake region behind a vertical cylinder. However, their simulations started from an equilibrium hole obtained from experimental results such that no scour evolution was analyzed. Khosronejad et al. (2011, 2012) developed a Fluid-Structure Interaction Curvilinear Immersed Boundary (FSI-CURVIB) method with a $k-\omega$ closure model. Their work has shown that the bluntness of the pier significantly influences the predictive capabilities of models. Link et al. (2012) used a detached-eddy simulation (DES) to simulate scour hole evolutions around circular and rectangular piers. Kim et al. (2017) studied scour erosion around two cylinders using LES coupled with a morphodynamic model

in a Lagrangian framework (immersed boundary method to track the sediment and fluid interface). More recently, new technique appeared to study the sediment particle: Nagel (2018) used a Eulerian two-phase model to study the live bed erosion around a cylinder, while Liu et al. (2018) used LES-DEM technical to simulate the sediment saltation in a rough-wall turbulent boundary layer. They showed the flow structures behind the cylinder at equilibrium scour hole. In this work, a 3D numerical study is present on local scour around a vertical cylinder using the Engelund & Fredsøe (1976) bedload formula in Roulund et al. (2005), which is classified as a live bed case (Melville & Chiew, 1999). A second-order unstructured finite-volume model combined with a sigma-coordinate system is applied to describe the dynamic shape of the sediment-water interface. In order to prevent the bed slope from exceeding the angle of repose in the sediment material, a mass conservative sand-slide model is developed. Large Eddy Simulation is applied in order to simulate the HV-system structure at the base of a vertical cylinder. Large-scale coherent structures in the presence of an HV system in the near-bed region as well as vortex shedding in the wake region are observed and discussed here. Table 1.1 provides highlights on the present study by giving an overview of different terms handled in the aforementioned studies.

Table 1.1 List of methods used in scouring simulations of different references

Reference	Numerical model	Turbulence model	Sand slide model	Water-sediment interface	Re _b	Physical phenomenon
Roulund (2005)	Structured finite volume method (FVM)	RANS (k- ω)	Updated particle velocity	Multigrid mesh	4.6×10^4	Scour hole evolution (Live bed erosion)
Kirkil (2008, 2010, 2015)	Structured finite volume method (FVM)	LES	Fixed bed(no)	Fixed bed(no)	1.6×10^4	HV System No scour evolution
Khosronejad (2012)	Unstructured finite volume method (UFVM)	RANS (k- ω)	Mass-conservative	FSI-CURVIB	4.95×10^4	Scour hole evolution (Live bed erosion)
Link et al. (2012)	Structured finite volume method (FVM)	DES	No	Lagrangian model	3.15×10^4	Scour hole evolution (Clear-water erosion)
Kim et al. (2017)	Structured finite volume method (FVM)	LES	No	Lagrangian model	4.0×10^4	Scour hole evolution (Clear-water erosion)
Baykal et al. (2014, 2017)	Structured finite volume method (FVM)	RANS (k- ω)	Updated particle velocity	Multigrid mesh	1.7×10^4	Scour hole evolution (Clear-water erosion)
Zhou (2017)	Structured finite volume method (FVM)	RANS (k- ω)	Mass-conservative	Dynamic mesh deformation	4.6×10^4	Scour hole evolution (Live bed erosion)
Nagel (2018)	Structured finite volume method (FVM)	RANS (k- ω)	No	Two-phase model	4.6×10^4	Scour hole evolution (Live bed erosion)
Current work (2019)	Unstructured finite volume method (UFVM)	LES	Mass-conservative	Sigma transformation	4.6×10^4	HV System Scour evolution (Live bed erosion)

The originality of this work is based on the construction of Projection Methods (PM) using Adams-Bashforth scheme formulation, in combining the momentum interpolation method (MIM) for determining face-normal velocity with central schemes for both advection and diffusion terms. MIM allows us to overcome checkerboard problems in pressure and velocity fields. In addition, the approximation of the cross diffusion terms is improved to handle non-orthogonal, unstructured grids with moderate skewness by introducing an additional correction term. By this way, we can get the second-order accuracy in space and in time, required by LES, for simulating flows at moderate Reynolds numbers. The current paper reports the first known investigation of both scour evolution and coherent structure using an unstructured finite volume method.

1.4. Organization of the manuscript

This work contributes to the knowledge improvement of the interactions between offshore wind turbine or bridge pier and its environment, and is organized as follows.

Chapter 2 focuses on the numerical methodology of a three-dimensional solver using unstructured finite volume method (UFVM) for Navier-Stokes equations. The non-dimensional scaling and the discretization schemes using LES on 3D unstructured collocated grid are presented. Projection method is used to decouple velocity and pressure, and Adams-Bashforth scheme is used for time stepping. Equations in sigma-transformation coordinate, different boundary conditions and parallel methods are also demonstrated. Then, a sediment bed deformation model using the Engelund & Fredsøe (1976) bedload formula in Roulund et al. (2005) is presented. In order to prevent the bed slope from exceeding the angle of repose in the sediment material, a mass conservative sand-slide model is developed.

Parts of these methods are published in Uh Zapata et al. (2019) in Appendix C1.

NSMP3D has been validated by several test cases in Chapter 3 to check the accuracy orders of the used numerical techniques and its ability in turbulent flow simulations. The test case of 2D decaying vortex shows that NSMP3D has second order of accuracy in space and in time, which permits simulations of free-surface and non-hydrostatic flows at high Reynolds numbers and different Froude numbers. The test case of lid-driven cavity flows shows that NSMP3D can provide the results equivalent to those obtained from previous numerical studies with capturing well the secondary vortices. The test case on standing waves in closed basin prove the capacity of NSMP3D in computing with accuracy free-surface and

non-hydrostatic flows, while the test case of wave propagation over a submerged bar can examine the performance of our algorithm in modelling wave deformation over uneven bottoms. At last, speed-up test case is used to test the parallel performance of the proposed model.

Parts of these results are under minor revision in Zhang et al. (2019b) in Appendix C2.

Chapter 4 presents a 3D numerical study on local scour around a vertical cylinder using the Engelund & Fredsøe (1976) bedload formula in Roulund et al. (2005), which is classified as a live bed case (Melville & Chiew, 1999). In order to prevent the bed slope from exceeding the angle of repose in the sediment material, a mass conservative sand-slide model is developed. Large Eddy Simulation is applied in order to simulate the HV-system structure at the base of a vertical cylinder. Large-scale coherent structures are observed and discussed here in the presence of an HV system in the near-bed region as well as vortex shedding in the wake region. The discussions on large-scale coherent structures with the presence of the HV system in the near-bed region and vortex shedding in wake region are given here.

Parts of these results are published in Zhang et al. (2019a) in shown in Appendix C3.

Appendix A presents the technology on the coding about the periodic boundary condition in parallel computation. The modifications of the memory structure and the communication technique from previous code are described.

Appendix B presents dilute turbidity currents in an inclined channel flow driven by suspended sediments. The suspended sediments under the influence of gravity drive the flow in the channel and simultaneously settle towards the bed. The interaction of sediments and turbulence lead to (i) skewing of the streamwise driving force towards the bed, and (ii) stable stratification that damps bed-normal momentum and mass transport. With increasing the settling velocity, flow turbulence is less able to keep the sediments in suspension, and the flow in the channel tends towards the laminar solution.

Chapter 2

Numerical Methods

2.1. Governing equations

In Computational Fluid Dynamics (CFD), the Navier-Stokes equations for incompressible flow express the conservation laws of mass and momentum in fluid flows. Within an incompressible volume of fluid, the governing equations of motion are:

$$\nabla \cdot \mathbf{u} = 0, \quad (2.1)$$

$$\frac{\partial \mathbf{u}}{\partial t} + \nabla \cdot (\mathbf{u}\mathbf{u}) = -\frac{1}{\rho} \nabla p + \nabla \cdot \left(\frac{\mu}{\rho} \nabla \mathbf{u} \right) + \mathbf{f}_e, \quad (2.2)$$

where $\mathbf{u} = (u, v, w)$ is the velocity components in three directions (x, y, z) in Cartesian coordinate. P is the pressure, μ is dynamic viscosity, and \mathbf{f}_e is any other external forces. The pressure is given by $P = p_a + \rho g(\eta - z) + p$, where g is the gravitational acceleration, p_a is the atmospheric pressure, η is the free-surface elevation, p is the non-hydrostatic pressure component. In this work, we always consider $p_a = 0$. The flow field for an incompressible fluid including viscous and turbulence effects can be fully described by solving above two equations numerically.

2.1.1. Non-dimensional scaling

Using dimensionless parameters such as Reynolds number and Froude number, similar flow patterns in different fluid flow situations can be easily predicted using numerical simulation and allow the comparison between similar flow physics carried out at different scales and with different fluid properties.

In order to obtain the non-dimensional equations, the following substitutions are made by using reference velocity V and length H .

$$u = \tilde{u}V, x = \tilde{x}H, t = \tilde{t} \frac{H}{V}, p = \rho \tilde{p}V^2, f_e = \rho \tilde{f}_e \frac{V^2}{H}, \quad (2.3)$$

where variables with tilde are the dimensionless quantities. Introducing the substitution above into Eq.(2.2), take x direction as example, the following equation can be obtained.

$$\frac{V^2}{H} \frac{\partial \tilde{u}}{\partial \tilde{t}} + \frac{V^2}{H} \left(\tilde{u} \frac{\partial \tilde{u}}{\partial \tilde{x}} + \tilde{v} \frac{\partial \tilde{u}}{\partial \tilde{y}} + \tilde{w} \frac{\partial \tilde{u}}{\partial \tilde{z}} \right) = -\frac{V^2}{H} \frac{\partial \tilde{p}}{\partial \tilde{x}} + \frac{\mu V}{\rho H^2} \left(\frac{\partial^2 \tilde{u}}{\partial \tilde{x}^2} + \tilde{v} \frac{\partial^2 \tilde{u}}{\partial \tilde{y}^2} + \tilde{w} \frac{\partial^2 \tilde{u}}{\partial \tilde{z}^2} \right) + \frac{V^2}{H} \tilde{f}_{ex}. \quad (2.4)$$

As V and H are both constants once selected, the above equation can then be simplified as

$$\frac{\partial \tilde{u}}{\partial \tilde{t}} + \left(\tilde{u} \frac{\partial \tilde{u}}{\partial \tilde{x}} + \tilde{v} \frac{\partial \tilde{u}}{\partial \tilde{y}} + \tilde{w} \frac{\partial \tilde{u}}{\partial \tilde{z}} \right) = -\frac{\partial \tilde{p}}{\partial \tilde{x}} + \frac{\mu}{\rho VH} \left(\frac{\partial^2 \tilde{u}}{\partial \tilde{x}^2} + \tilde{v} \frac{\partial^2 \tilde{u}}{\partial \tilde{y}^2} + \tilde{w} \frac{\partial^2 \tilde{u}}{\partial \tilde{z}^2} \right) + \tilde{f}_{ex}, \quad (2.5)$$

with the dimensionless Reynolds number defined as

$$\text{Re} = \frac{\rho VH}{\mu} = \frac{VH}{\nu}. \quad (2.6)$$

In NSMP3D, we can also put the numerical viscosity into dimensionless variable by

$$\tilde{\nu} = \frac{\nu}{VH} = \frac{1}{\text{Re}}. \quad (2.7)$$

When running a numerical case to reproduce an experimental result, we first select the reference velocity and reference length, based on the physical kinematic viscosity, the Reynolds number can be calculated using Eq. (2.7). Then the dimensionless numerical viscosity $\tilde{\nu}$ is evaluated as $1/\text{Re}$ and other variables can be non-dimensional respectively.

2.1.2. Unstructured finite volume method

To solve Eqs. (2.1), (2.2), the NSMP3D code uses the finite volume method to discretize the governing equations. Thus, the computational domain is divided into a number of control volumes where variables as velocities and pressure are located at the center of each control volume. Then the differential forms of the governing equations are integrated over each control volume. Using the divergence theorem, the volume integral can be recast into surface integrals at cell faces in order to calculate the flux change over the whole control volume. In NSMP3D, each control volume is prism with a triangle base (see Figure 2.1).

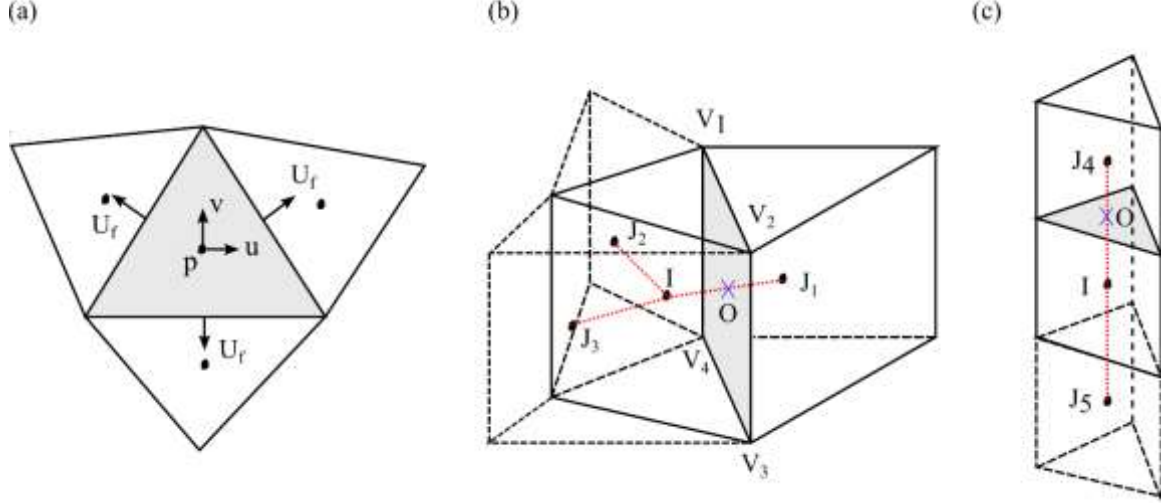


Figure 2.1: 3D sketch of geometry entities (a) 2D schematic variables stored in the cell center for collocated grid (b) Horizontal neighbor cells, and (c) Vertical neighbor cells.

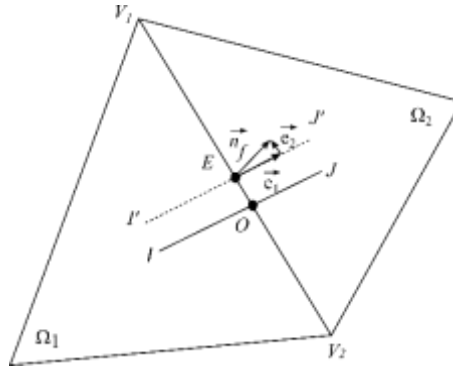


Figure 2.2: 2D sketch of geometry entities.

The integral forms of non-dimensional Navier-Stokes equations are:

$$\int_V \frac{\partial u_i}{\partial t} dV + \oint_S (u_i u_j)_f n_j dS = - \int_V \frac{\partial p}{\partial x_i} dV + \oint_S \left(\frac{1}{\text{Re}} \frac{\partial u_i}{\partial n} \right)_f dS + \int_V f_{ei} dV, \quad (2.8)$$

$$\oint_S u_i n_i dS = 0, \quad (2.9)$$

where the subscript $i, j = 1, 2, 3$ represent the three directions in the Cartesian coordinates, and the subscript f denotes the interpolated value on the cell face. V denotes the volume of the cell, S denotes the cell surface, n is the vector unit normal to each face, and $\partial u / \partial n$ represents the outward velocity normal gradient on the face shared by two cells.

To simplify, in the following section, if not specify, we ignore the tilde, which indicates the dimensionless quantities. As suggested by Kim and Choi (2000), the face normal velocity, which is defined at the center of each cell face, given by

$$U_f = (u_i)_f n_i, \quad (2.10)$$

where $(u_i)_f$ is the i^{th} component of velocity at the midpoint of face f . Substitute Eq., (2.10) into Eqs. (2.8) and (2.9), yields:

$$\int_V \frac{\partial u_i}{\partial t} dV + \oint_S (u_i)_f U_f dS = - \int_V \frac{\partial p}{\partial x_i} dV + \oint_S \left(\frac{1}{\text{Re}} \frac{\partial u_i}{\partial n} \right)_f dS + \int_V f_{ei} dV, \quad (2.11)$$

$$\oint_S U_f = 0. \quad (2.12)$$

The discretization of the governing equations is performed on triangular prism based on unstructured grids. The three-dimensional formation of geometry entities are shown in Figure 2.1.

2.1.2.1. Convection Flux

The Momentum Interpolation Method (MIM) is used to determine the face-normal velocity in the convection flux term $\oint_S (u_i)_f U_f dS$. Figure 2.2 shows the 2D formation of the geometry entities, where I, J are the centers of two cells sharing a face, and O is the intersection point between line \overline{IJ} and the sharing face, and E is the face midpoint. The value ϕ_f at the face midpoint can be obtained by second-order interpolation:

$$\phi_f = \alpha_{IJ} \phi_I + (1 - \alpha_{IJ}) \phi_J + \frac{1}{2} \overline{OE} \cdot \left(\overline{(\nabla \phi)_I} + \overline{(\nabla \phi)_J} \right), \quad (2.13)$$

where ϕ denotes velocity components, $\alpha_{IJ} = |OJ|/|IJ|$, $\overline{\nabla \phi}$ is the gradient at the cell center, which is calculated using the least squares method, similar to the case presented in Shi et al. (2013). This centered interpolation scheme insures the second order accuracy. The value at the vertical face midpoints is calculated by the same way as in 2D formation because all horizontal cell-centers are located at the same height (Figure 2.1c). Vertically, as O and E are located at the same point, thus $\overline{OE} = 0$ in Eq. (2.13).

2.1.2.2. Diffusive Flux

The normal face derivatives in the diffusive flux $\oint_s \left(\frac{1}{\text{Re}} \frac{\partial u_i}{\partial n} \right) dS$ are calculated as the original work of Kim and Choi (2000). The diffusive flux at the face midpoint is approximated by using linear interpolation of two components, principle diffusion and cross diffusion as follows:

$$\frac{\partial \phi}{\partial n} = \frac{(\phi_J - \phi_I) |\vec{e}_1|}{|\vec{IJ}|} + \frac{(\phi_{V_2} - \phi_{V_1}) \overline{V_2 V_1}}{|\overline{V_2 V_1}| |\overline{V_2 V_1}|} \cdot \vec{e}_2, \quad (2.14)$$

where \vec{e}_1 and \vec{e}_2 are the two components of the face-normal vector $\vec{n}_f = \vec{e}_1 + \vec{e}_2$ as shown in Figure 2.2. For orthogonal grid, \vec{e}_1 is the same as \vec{n}_f and the second term should always equal to zero.

By introducing the cross diffusion term, the scheme above can handle non-orthogonal, unstructured grid with a moderate skewness. For problems with high skewness grids, such as the real estuary, the approximation of the cross diffusion term still needs to be improved to insure the accuracy. Xue and Barton (2013) proposed an additional term using the value at a shifted position from cell center. As the intersection point between the line connecting two nearby cell centers and the cell face does not necessarily coincident with the face center, two projected points (I' and J') parallel to the connecting line are constructed by moving the corresponding cell centers along the distance vector (\overline{OE}). By using linear interpolation, the values of the projected points can be obtained and used to calculate the diffusion term in Eq. (2.14). While the cross-diffusion term is for treating non-orthogonality of the mesh, the added high order term can be used to ensure the diffusion from skewness of the grid, as follows:

$$\frac{\partial \phi}{\partial n} = \frac{(\phi_{J'} - \phi_{I'}) |\vec{e}_1|}{|\vec{IJ}|} + \frac{(\phi_{V_2} - \phi_{V_1}) \overline{V_2 V_1}}{|\overline{V_2 V_1}| |\overline{V_2 V_1}|} \cdot \vec{e}_2. \quad (2.15)$$

Thus,

$$\frac{\partial \phi}{\partial n} = \frac{(\phi_J - \phi_I) |\vec{e}_1|}{|\vec{IJ}|} + (\nabla \phi_J - \nabla \phi_I) \cdot \overline{OE} \frac{|\vec{e}_1|}{|\vec{IJ}|} + \frac{(\phi_{V_2} - \phi_{V_1}) \overline{V_2 V_1}}{|\overline{V_2 V_1}| |\overline{V_2 V_1}|} \cdot \vec{e}_2. \quad (2.16)$$

For 3D control volume, horizontally, the face center gradient value is similar as 2D cases. Vertically, as O and E are located at the same point and all face mid-points are vertical, thus $\overline{OE} = 0$ and $\vec{e}_2 = 0$ in the Eq. (2.15).

2.1.3. Projection method reconstruction using Adams-Bashforth scheme

The Projection Method (PM) to decouple the velocity and pressure fields, was proposed by Chorin (1968). Later, Perot (1993) showed that PM is still first-order accuracy in time. So he proposed another form of the PM by a block LU factorization of the fully discretized equations and the second order of accuracy in time would be insured by using the Crank-Nicholson scheme for diffusion terms and the Adams-Bashforth scheme for convection terms. In this work, the convection and diffusive fluxes are explicitly solved at each time step. Thus, an intermediate velocity field u_i^* can be obtained.

$$\int_V \frac{u_i^* - u_i^n}{\Delta t} dV = -\oint_S \left(u_i^{n+1/2} \right)_f U_f^{n+1/2} dS + \oint_S \left(\frac{1}{\text{Re}} \frac{\partial u_i^{n+1/2}}{\partial n} \right)_f dS + \int_V f_{ei}^{n+1/2} dV, \quad (2.17)$$

where superscript n is the variables at the discrete time t^n , and Δt is the time step.

The velocity at the next time step is calculated from

$$\int_V \frac{u_i^{n+1} - u_i^*}{\Delta t} dV = -\int_V \frac{\partial p^{n+1/2}}{\partial x_i} dV. \quad (2.18)$$

The Pressure Poisson Equation (PPE) can be obtained implicitly by taking the divergence-free condition:

$$\oint_S \left(\frac{\partial p^{n+1/2}}{\partial n} \right)_f dS = \frac{1}{dt} \oint_S U_f^* dS, \quad (2.19)$$

where $U_f^* = (u_i^*)_f n_i$ is the intermediate face-normal velocity. The resulting linear system is solved using a preconditioned Biconjugate Gradient Stabilized Method (BICGSTAB).

The Adams-Bashforth scheme formulation, the right hand side of Eq. (2.17) is given explicitly insuring second-order accuracy in time under the following form:

$$RHS^{n+1/2} = \frac{3}{2} RHS^n - \frac{1}{2} RHS^{n-1} + O(\Delta t^2), \quad (2.20)$$

where

$$RHS_i = -\oint_S (u_i)_f U_f dS + \oint_S \left(\frac{1}{Re} \frac{\partial u_i}{\partial n} \right)_f dS + \int_V f_i dV. \quad (2.21)$$

The preconditioned BICGSTAB solver was used to solve Eq.(2.19) and the pressure at time t^{n+1} is also obtained by using the Adams–Bashforth scheme:

$$\frac{\partial p^{n+1}}{\partial x_i} = \frac{3}{2} \frac{\partial p^n}{\partial x_i} - \frac{1}{2} \frac{\partial p^{n-1}}{\partial x_i} + O(\Delta t^2), \quad (2.22)$$

The obtained pressure field is then used to correct the final velocity field. The divergence free condition is enforced on the face-normal velocities, and a strong coupling between pressure and velocity is ensured:

$$u_i^n = u_i^* - dt \frac{\partial p^n}{\partial x_i}, U_f^n = U_f^* - dt \frac{\partial p^n}{\partial n}. \quad (2.23)$$

In the current study, the Courant-Friedrichs-Lewy (CFL) number is specified according to the original definition given by Kim and Choi (2000),

$$CFL = \frac{dt}{2V} \sum_f |U_f \cdot A_f|, \quad (2.24)$$

where A_f is the cell face area.

2.1.4. Boundary condition

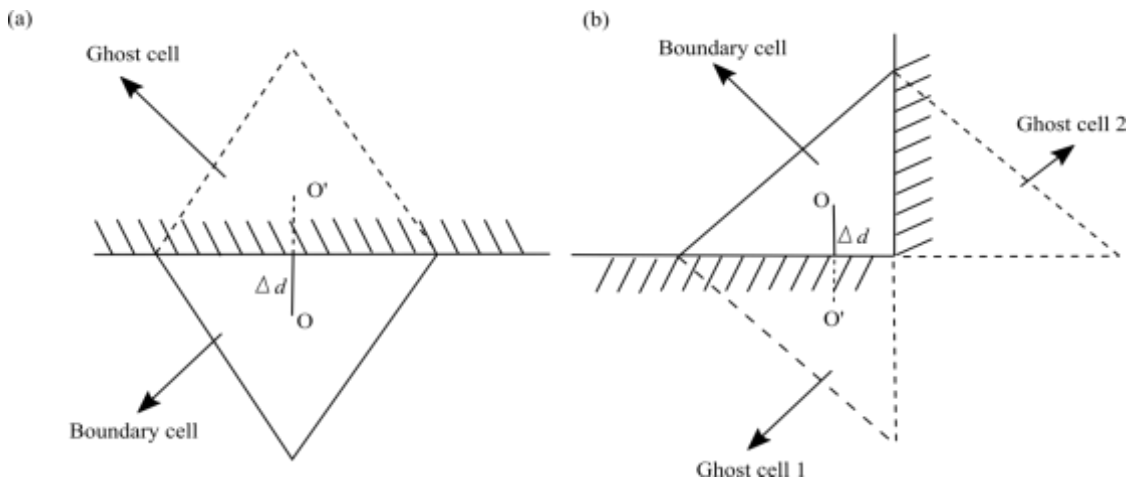


Figure 2.3: The description of ghost cell on a solid boundary (a) general boundary cell (b) corner boundary cell

A ghost cell method was used to enforce the boundary condition as Figure 2.3. For the cells on the physical boundaries, ghost cells with a distance Δd away from the physical boundaries were constructed, which corresponds to the distance between the cell-centered node and the boundary in the normal direction.

Generally, for Dirichlet boundary condition, boundary conditions are imposed on both the fictitious cells and the boundary vertex points, with $\Phi_{ghost}=2C-\Phi_c$ and $\Phi_{V,bc}=C$, where C is the constant value given by the boundary condition. For Newmann boundaries, only the fictitious cells are updated using $\Phi_{ghost}=\Phi_c$, while the values on the boundary vertex points are interpolated using only the inside cell centers. For periodic boundaries, boundary conditions are imposed on two corresponding cells respectively on inflow and outflow boundary, with $\Phi_{out,ghost}=\Phi_{in}$ and at the same time $\Phi_{in,ghost}=\Phi_{out}$.

More specifically, we have the following different boundary conditions:

1) At the rigid non-adhesive surface (free slip wall). The partial derivative of the velocity is equal to zero in tangent wall directions as $\partial u/\partial \sigma = \partial v/\partial \sigma = 0$; the vertical velocity normal to the wall is equal to zero as $w=0$; the partial derivative of the pressure is always equal to zero as $\partial p/\partial \sigma = 0$.

2) At the rigid adhesive bed (no-slip wall), the velocities are equal to zero: $u = v = w = 0$, as well as the partial derivative of the pressure: $\partial p/\partial \sigma = 0$.

3) At the free surface, the tangential stress equals zero resulting in $\partial u/\partial \sigma = \partial v/\partial \sigma = 0$; the velocity component satisfies the kinematic boundary condition, $w = \partial \eta/\partial t + u \partial \eta/\partial x + v \partial \eta/\partial y$; and the pressure condition $p = 0$ is applied when the Poisson equation is solved.

4) At inlet boundary, velocity is specified as $u = u_I$, $v = v_I$, $w = w_I$, where u_I , v_I , w_I are values set by user, and pressure condition $\partial p/\partial x = 0$ is applied.

5) At outlet boundary, $\partial u/\partial x = \partial v/\partial x = \partial w/\partial x = 0$ and $\partial p/\partial x = 0$ is applied. To avoid any wave reflection from the downstream end of computation domain, we use a combination of a sponge layer technique (Park et al., 1999) and a Sommerfeld-type radiation boundary condition. Thus, the following artificial damping terms are added to the right-hand side of horizontal momentum Eq. (2.40).

$$\left[\alpha_d \left(\frac{x^* - x_0^*}{L_x} \right)^2 \left(\frac{z_b - z}{z_b - z_s} \right) \right] u, x^* \geq x_0^*, \quad \left[\alpha_d \left(\frac{y^* - y_0^*}{L_y} \right)^2 \left(\frac{z_b - z}{z_b - z_s} \right) \right] v, y^* \geq y_0^*, \quad (2.25)$$

where x_0^* and y_0^* denote the starting point of the damping zone of length L_x and L_y at the x^* and y^* directions, respectively; z_b and z_s represent the bottom and the free surface, respectively; and the damping strength parameter, α_d , determines the damping rate. At the end of the sponge layer, the Sommerfeld-type radiation condition is used to further enhance wave absorption. We refer to Yuan and Wu (2004) for more details.

2.1.5. Parallelization

The parallelization of the finite volume discretization is based on a domain decomposition method with overlapping sub-domains. The computational domain is divided into several sub-domains of almost the same number of elements by the partitioning utility called Chaco (Lien, 2000). Each subdomain is calculated independently for a processor. The NSMP3D links cell-centered and vertex unknowns assigned by different sub-domains. Therefore, the transmission of data between processors is necessary to perform the calculations in parallel. Standard MPI is used to implement the algorithm.

To ensure efficient data communication, every sub-domain is extended to create an overlapping region with each of its neighboring sub-domains. The subdomain extension overlap is that all the elements surrounding boundary vertex points are included, see Figure 2.4. Thus, the overlapping region guarantees that all unknown variables used in the finite volume discretization scheme are included. Another advantage of these overlapping regions is that no vertex communication is needed. For communication implementation, the number of communication must be minimized in order to minimize overhead. Thus, the data changed through overlapping points are grouped in vectors to reduce communication.

The computation of the Poisson equation is an important element in an incompressible code, which consumes most of the CPU time. In particular, the referenceS (Zhao & Wang, 2012; Gorobets, 2015) talking about the technology of the parallelization of BiCGSTAB by domain decomposition is recommended .

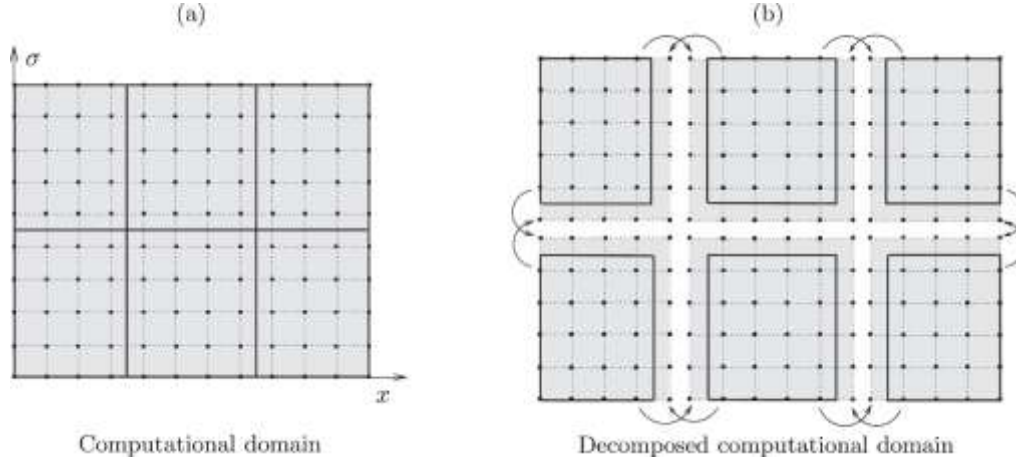


Figure 2.4: Configuration of the overlapping subdomains for the MPI, from Uh Zapata et al. (2014).

2.2. Numerical simulation of turbulence

Turbulent flow refers to the high Reynolds number flows, which are characterized by velocity fluctuations in all directions and over a large range of scales. In most CFD simulations, it is usually a computational challenging to solve the turbulent flow in full resolution because finer resolution is required for higher Reynolds numbers (Ferziger & Perić, 2002). Depending on the treatment or the averaging procedure to overcome the complexity of turbulence, numerical simulations of turbulence flows can be classified into three most used categories: the Direct Numerical Simulation (DNS), the RANS-based simulation (RANS) and the Large Eddy Simulation (LES). DNS will simulate every turbulent cascade without any assumption. The major difficulty when performing DNS resides in the fact that a three-dimensional DNS requires a number of mesh points $N^3 > Re^{9/4}$. Therefore, the computational cost of DNS is very high even at low Reynolds numbers. RANS simulates only time-averaged quantities and is designed to work outside the viscous sublayer, where viscous effects are negligible compared to inertial effects. LES is the intermediate category between DNS and RANS. Large scale effects of turbulence are solved like DNS, but small scale effects are handled with subgrid scale model.

In this study, we use the Smagorinsky subgrid scale model and the effects of Smagorinsky constants in LES are discussed. At this stage, the development is limited to the fluid phase but validated for the academic test cases, which require the implementation of the second-order schemes in time and in space, periodic boundary conditions with MPI technology.

For incompressible flow, the space-filtered Navier-Stokes equations can be written as

$$\frac{\partial \bar{u}_i}{\partial t} + \frac{\partial}{\partial x_j} \bar{u}_i \bar{u}_j = -\frac{1}{\rho} \frac{\partial \bar{p}}{\partial x_i} + \frac{\partial}{\partial x_j} \left[\nu \left(\frac{\partial \bar{u}_i}{\partial x_j} + \frac{\partial \bar{u}_j}{\partial x_i} \right) \right] - \frac{\partial \tau_{ij}^{sg}}{\partial x_j}, \quad (2.26)$$

$$\frac{\partial \bar{u}_i}{\partial x_i} = 0, \quad (2.27)$$

where the bar over quantities denotes space-filtered quantity, \bar{u}_i are the resolved components of the velocity vector, \bar{p} is the resolved pressure, and

$$\tau_{ij}^{sg} = \overline{u_i u_j} - \bar{u}_i \bar{u}_j, \quad (2.28)$$

is the Sub-Grid Stress (SGS) tensor, which are used to take in account the effect of unresolved length scales.

As suggested by Smagorinsky, the smallest turbulent eddies are almost isotropic and Boussinesq eddy viscosity assumption can be used to provide an accurate approximation of the effects of these unresolved smallest eddies. According to the Boussinesq assumption, the momentum transfer caused by turbulent eddies can be modelled with an eddy viscosity, and the relationship between the eddy viscosity and the sub-grid stress tensor can be described as:

$$\tau_{ij}^{sg} = -2\nu_t \bar{S}_{ij} + \frac{1}{3} \tau_{ii}^{sg} \delta_{ij}, \quad (2.29)$$

where δ_{ij} is the Kronecker delta, and $\bar{S}_{ij} = \frac{1}{2} \left(\frac{\partial \bar{u}_i}{\partial x_j} + \frac{\partial \bar{u}_j}{\partial x_i} \right)$ is the resolved rate-of-strain tensor.

The SGS Model should be employed to take into account the small filtered-out eddies and their interaction effect between the large resolved eddies by providing an accurate approximation of the SGS viscosity. One of the most widely used SGS models is the constant Smagorinsky model, which is as

$$\nu_t = l_{sg}^2 |\bar{S}|, \quad (2.30)$$

where $|\bar{S}| = (2S_{ij}S_{ij})^{1/2}$, and l_{sg} is the sub-grid length scale. In the near wall region, the length scale of the sub-grid scale motions cannot be described with a constant value, but will decrease as the wall is approached. Thus, a wall damping function must be implemented in addition to the standard or constant Smagorinsky SGS model to capture this boundary layer

effect. Among all of the damping functions available, the Van Driest's function is most commonly used:

$$l_{sg} = C_s \Delta \left(1 - e^{-\frac{l_w^+}{A^+}} \right), \quad (2.31)$$

where l_w^+ is the non-dimensional distance from the center of a control volume to the wall as

$l_w^+ = l_w u_\tau^+ / \nu$ and $A^+ = 26$ is the damping coefficient. Δ is the averaged spacing $\Delta = V^{1/3}$ with V being the volume of the element, and C_s is the Smagorinsky constant. Lilly (1967) provided a theoretical analysis of the decay rate of the isotropic turbulent eddies in the inertial subrange of the energy spectrum and suggested a value for C_s between 0.17 and 0.21. For channel flow, there are strong anisotropic turbulent eddies in the near wall region, Deardorff (1970) suggested an optimal value for C_s which equals to 0.1. The differences in the suggested C_s values indicates that the behavior of the small eddies are not universal as assumed in the SGS model and a more sophisticated adjustment should be performed to provide a good turbulent approximation.

To further improve the near-wall asymptotic behavior of the eddy viscosity, the following wall damping function (Pope, 2000) was proposed to use the near wall distance instead of a constant sub-grid length scale

$$l_{sg} = \kappa l_w \left(1 - e^{-\frac{l_w^+}{A^+}} \right), \quad (2.32)$$

and κ is the von Kármán constant which is usually taken as 0.4.

Although Eq.(2.32) will provide us with a good approximation of the sub-grid length scale for the Smagorinsky SGS model, l_w^+ can be difficult to obtain as the friction velocity at each location is unknown. For multi-dimension problems with complex geometries, this can pose a challenge to the simulation because it needs to be calculated at every time step. At a flow separation point or a flow reattachment point, the friction velocity can be very small or close to zero which will expand the effective region of the wall damping function leading to inaccuracy and instability.

In this thesis, the near wall damping model of Mason & Thomson (1992) is used to achieved a modified length scale. According to Mason and Thomson, the modified length scale can be described by:

$$\frac{1}{l_{sg}^n} = \frac{1}{(C_s \Delta)^n} + \frac{1}{(\kappa l_w)^n}, \quad (2.33)$$

where n is the Mason wall matching power, which in most of following LES simulations, is taken as two. Having obtained the length scale, the turbulent viscosity at every location can be calculated using Eq.(2.30).

2.3. Sigma-transformation configuration

2.3.1. Sigma-coordinate

The sigma-coordinate has been developed by Phillips (1957). It is a method that allows working on configurations meaning with varying vertical boundaries like free surface and sediment bed interface. This method is employed to link the irregular physical domain to the actual computational domain, see Figure 2.5. The conventional sigma-coordinates map the total water depth that measures from the mobile bottom to the water surface onto a fixed range $\sigma = [0, 1]$ in the computational domain.

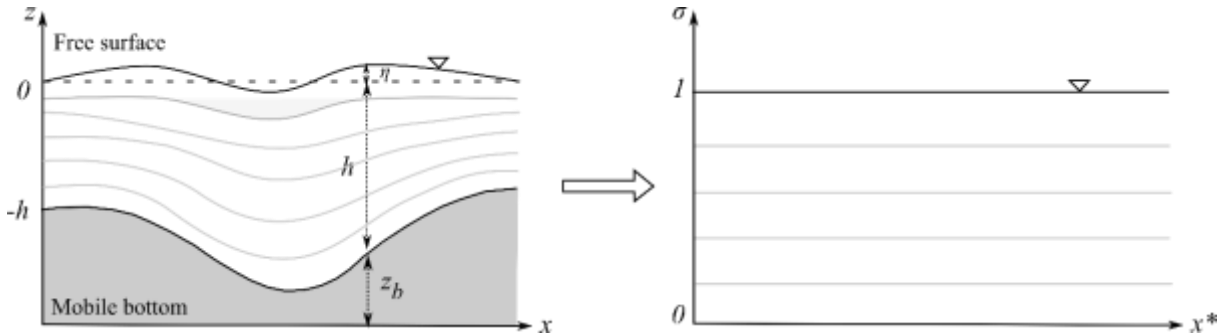


Figure 2.5: Vertical mesh before and after the sigma-transformation

The Cartesian coordinate system is then changed from (x, y, z, t) to the sigma-coordinate (x^*, y^*, σ, t^*) as followings

$$x^* = x, y^* = y, t^* = t, \sigma = \frac{z + h}{H}, \quad (2.34)$$

where $H(x^*, y^*, t^*) = h + \eta$ is the total water depth with $h(x^*, y^*)$ being the water depth and $\eta(x^*, y^*, t^*)$ being the free surface. $z = [-h, \eta]$ is the vertical coordinate for flowing water in the physical domain that has the origin $z_s = \eta$ on the free surface level and $z_b = -h$ on the bottom bed level. Using the principle of chain differentiation and the definition of the sigma

transformation (2.34), the partial differentiation of a variable $\Phi(x^*, y^*, \sigma, t^*)$ in the physical domain is transformed as follows:

$$\frac{\partial \phi}{\partial t} = \frac{\partial \phi}{\partial t^*} + \sigma_t \frac{\partial \phi}{\partial \sigma}, \quad (2.35)$$

$$\frac{\partial \phi}{\partial x} = \frac{\partial \phi}{\partial x^*} + \sigma_x \frac{\partial \phi}{\partial \sigma}, \quad \frac{\partial \phi}{\partial y} = \frac{\partial \phi}{\partial y^*} + \sigma_y \frac{\partial \phi}{\partial \sigma}, \quad \frac{\partial \phi}{\partial z} = \sigma_z \frac{\partial \phi}{\partial \sigma}, \quad (2.36)$$

where the partial derivatives of the transformation are given by

$$\sigma_t = -\frac{\sigma}{H} \frac{\partial H}{\partial t^*}, \quad (2.37)$$

$$\sigma_x = \frac{1}{H} \left(\frac{\partial h}{\partial x^*} - \sigma \frac{\partial H}{\partial x^*} \right), \sigma_y = \frac{1}{H} \left(\frac{\partial h}{\partial y^*} - \sigma \frac{\partial H}{\partial y^*} \right), \sigma_z = \frac{1}{H}. \quad (2.38)$$

2.3.2. Equations in sigma-coordinate

The Navier-Stokes equations, constructed in Cartesian coordinate, have to be modified in the transformed computational domain. Eqs. (2.1), (2.2) in the new coordinate (x^*, y^*, σ) are given by

$$\frac{\partial H}{\partial t^*} + \nabla^* H \underline{u} = 0, \quad (2.39)$$

$$\frac{\partial U}{\partial t^*} + U \nabla^* \underline{u} = -g S_\eta - \frac{1}{\rho} S_p + \nabla^* (\mu \Gamma \nabla^* U), \quad (2.40)$$

where

$$U = (Hu, Hv, Hw)^T, \underline{u} = (u, v, w)^T, \underline{w} = \sigma_t + u\sigma_x + v\sigma_y + w\sigma_z, \nabla^* = (\partial/\partial x^*, \partial/\partial y^*, \partial/\partial \sigma). \quad (2.41)$$

The right-hand side terms are given by

$$S_\eta = H \begin{pmatrix} \frac{\partial \eta}{\partial x^*} \\ \frac{\partial \eta}{\partial y^*} \\ 0 \end{pmatrix}, S_p = H \begin{pmatrix} \frac{\partial p}{\partial x^*} + \sigma_x \frac{\partial p}{\partial \sigma} \\ \frac{\partial p}{\partial y^*} + \sigma_y \frac{\partial p}{\partial \sigma} \\ \sigma_z \frac{\partial p}{\partial \sigma} \end{pmatrix}, \Gamma = H \begin{pmatrix} 1 & 0 & \sigma_x \\ 0 & 1 & \sigma_y \\ \sigma_x & \sigma_y & \sigma_x^2 + \sigma_y^2 + \sigma_z^2 \end{pmatrix}. \quad (2.42)$$

Further details of sigma-transformation applied to all the terms in N-S equations can be found in the work of Uh Zapata et al. (2014, 2016).

2.4. Sediment bed deformation

In this chapter, the basic framework of the morphodynamic model is outlined. The mathematical equation that governs the temporal variation of the sediment-water interface and a numerical model for solving this equation are presented. The numerical framework for coupling the morphodynamic model with the previously described hydrodynamic model is presented then in the subsequent section. The current work is focused on the numerical simulation of bedload transport and the suspended load is negligible. Free surface is also ignored because small Froude numbers are accounted for in our model (Roulund et al., 2005).

2.4.1. Continuity equation for sediment

The morphodynamical component modelled by the Exner-Polya equation is a solid transport discharge formula that depends on the hydrodynamical variables. The bed evolution caused by bedload transport is given by the Exner-Polya equation:

$$(1 - \eta) \frac{\partial z_b}{\partial t} + \nabla \cdot q_b = 0, \quad (2.43)$$

Here $z_b(x,y,t)$ is the local bed level, η is sediment material porosity, and q_b is the bedload transport rate depending on the hydraulic and sediment variables. The porosity of the granular material correlates to the particle arrangement (close and random) and monodispersity of materials. For really monodisperse material of identical beds, the solid volume fraction could vary between 0.54 and 0.74 depending on cubical arrangement or maximum hexahedral packing. With preparation of the sediment bed in water, the value is usually 0.6 and porosity η is taken as 0.4 (Pham Van Bang et al, 2008).

After application of the Green's theorem, the integral of the right hand side becomes

$$\iint_A \frac{z_b^{n+1} - z_b^n}{\Delta t} dS = -\frac{1}{(1 - \eta)} \sum_{j=1}^3 \int_{L_j} q_b \cdot n_j dl, \quad (2.44)$$

where A indicates a triangular element, while L_j and n_j ($j=1,2,3$) represent an edge and its corresponding unit normal vector of the triangular element. The formula to calculate q_b is presented in the following section.

2.4.2. Bedload formula

A two-dimensional bedload formula based on a description of physical processes proposed by Engelund and Fredsøe (1976) has been developed. The bedload transport rate q_b , is given by

$$q_b = \frac{1}{6} \pi d p_{EF} u_b, \quad (2.45)$$

where d is the grain size, and p_{EF} is the percentage of particles in motion on the bed surface. u_b is the mean velocity of a sediment particle in movement. With the experiment data from studies of Fernandez Luque and Van Beek (1976) and Meland and Norrman (1966), the particle velocity u_b has been determined as follows:

$$u_b = a(1 - 0.7\sqrt{\theta_c / \theta})u_\tau, \quad (2.46)$$

where θ is the Shields parameter associated with the skin friction, θ_c is the critical value of θ for the initiation of sediment motion on the bed, and a is an empirical constant. Experimental predictions are largely confirmed for $a = 10$ and a suitable choice of θ_c (Fernandez Luque & Van Beek, 1976; Meland & Norrman, 1966). The friction velocity u_τ is determined from method by Nikuradse (1933) based on bed roughness in logarithmic velocity profile:

$$\frac{\langle U \rangle}{u_\tau} = 2.5 \ln \left(\frac{z}{z_0} \right), \quad (2.47)$$

where z is the distance to the wall, and z_0 is the distance from the boundary, at which the idealized velocity given by the wall law goes to zero, $\langle \rangle$ represents time-averaged character (Rodi et al., 2013). According to Nikuradse (1933), z_0 is equal to $k_s/30$, in which k_s is the Nikuradse equivalent sand roughness.

Engelund and Fredsøe (1976) gave a semi-empirical expression for p_{EF} , when the bed shear stress exceeds the critical value so that the sediment particles on the bed will start to move.

$$p_{EF} = \left[1 + \left(\frac{\frac{1}{6} \pi \mu_d}{\theta - \theta_c} \right)^4 \right]^{-1/4}, \quad (2.48)$$

where $\mu_d = 0.51$ represents the dynamic friction coefficient corresponding to value 27° for the angle of repose of sediment material.

In this work, the bedload is assumed to move in the same direction as the tangential shear stress on the bed. The present bedload model reduces the algorithm to simple calculation as shown by Zhou (2017).

2.4.3. Sand-slide model

Without a sand-slide model, an unrealistic bed-slope which is larger than the physical value of the angle of repose will occur, and large mesh distortion especially will appear, especially around the vertical cylinder. Consequently, the sigma-transformation will lose its ability to simulate scour holes. In order to prevent the bed slope from exceeding the sediment angle of repose, a mass-conservative-based algorithm for sand-slide has been applied successfully (Khosronejad et al., 2011, 2012). The bed slope is defined by the elevation gradient between point p and any point i ($i=1, 2, 3$) of the neighbouring cell centers, see Figure 2.6(a). If the slope angle exceeds the material angle of repose, the sediment particles will slide down to the angle of repose, see Figure 2.6(b). The correction to bed elevations is given by:

$$\frac{(z_{bp} + \Delta z_{bp}) - (z_{bi} + \Delta z_{bi})}{\Delta l_{pi}} = \tan \varphi, \quad (2.49)$$

where φ is the material angle of repose, z_{bp} and z_{bi} are the bed elevations at points p and i^{th} neighbour; Δz_{bp} and Δz_{bi} are the corresponding corrections, and Δl_{pi} is the horizontal distance between these two points. The bed elevation corrections are obtained by the mass conservation as follows:

$$A_{hp} \Delta z_{bp} - \sum_{i=1}^3 A_{hi} \Delta z_{bi} = 0, \quad (2.50)$$

where A_{hp} and A_{hi} are the projection of cells p and i , respectively. Since the mesh points move only in the vertical direction, the bed cells projected onto the horizontal plane have the same cell area.

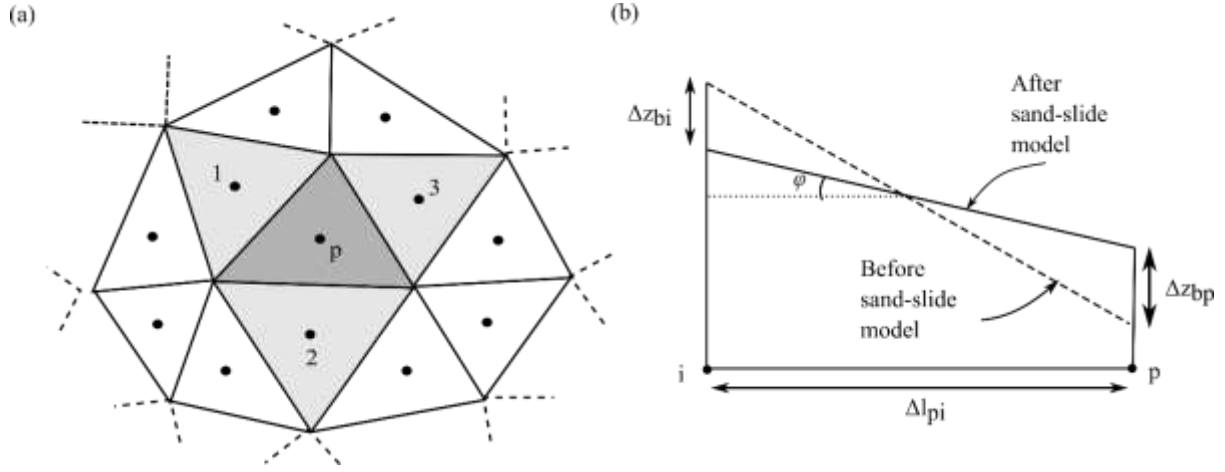


Figure 2.6: Sand-slide algorithm: (a) an unstructured triangular bed mesh, and (b) definition of quantities used to adjust the computed bed slope.

2.4.4. Morphological update routine

The procedure of calculating the scour around a cylinder in the computations was as follows:

- i. Obtain the flow field by solving the three-dimension unsteady Navier–Stokes Eqs. (2.1) and (2.2) with a LES coupled with the sigma-transformation method;
- ii. Calculate the sediment transport due to bedload using the bedload formula (2.45) proposed by Roulund et al. (2005), which is valid for low particle Reynolds numbers;
- iii. Update the new bed elevations using Exner–Polya formula (2.43) which relates the gradient of the bedload flux and time variation of the bed surface;
- iv. Check the sand-slide model. The entire bed is swept to identify bed cells at which the maximum bed slope is larger than the angle of repose. The algorithm (2.49) and (2.50) is applied iteratively until all slopes are smaller than the material angle of repose. The bed sweeping sequence during each iteration of this algorithm is alternated between the upstream-to-downstream and downstream to upstream directions. For each time steps the land-slide algorithm to converge within 6 iterations. For more details the reader is referred to Khosronejad et al. (2012).
- v. Check the mass conservation. It's critical to conserve the volume at each time step as the bed elevation and consequently the domain geometry change in a coupled hydraulic and sediment transport model. In our work, we impose global mass conservation by checking the rate of volume change associated with the bed

deformation, keeping track of the position of the triangular bed mesh at the current and previous time steps.

- vi. Return to step 1. The overall flow chart for the numerical model is shown in Figure 2.7.

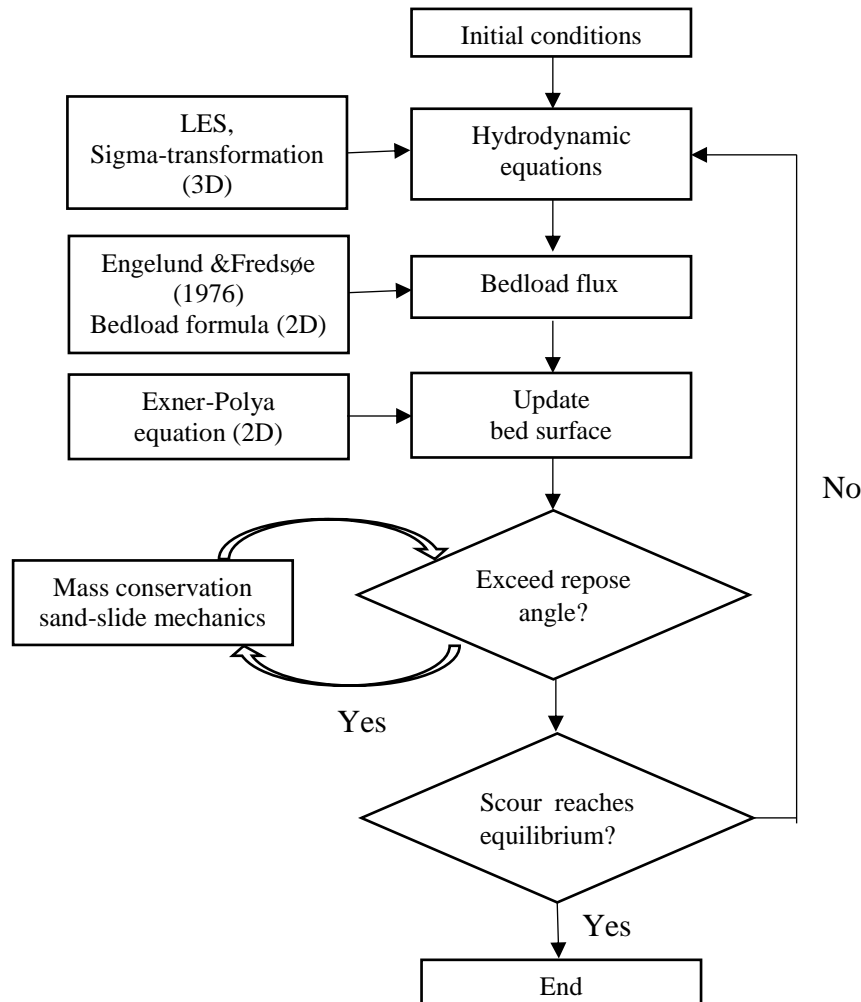


Figure 2.7: Flow chart for the numerical model.

2.5. Conclusion

In this chapter, a three-dimensional solver using unstructured finite volume method (UFVM) for Navier-Stokes equations is presented on an unstructured collocated grid. The 3D physical domain is composed of an arbitrary domain in the horizontal direction and is bounded by the irregular bottom and free surface in the vertical direction. Sigma-coordinate system, as shown in Uh Zapata et al. (2014), is extended for physical problems with free surface and mobile bed. The Momentum Interpolation Method (MIM) is used to avoid the check-board problem caused by the un-staggered grid. This is achieved by introducing face

normal velocities at the mid-points of the corresponding cell faces. The dynamic pressure is solved in an iterative approach for free surface flows.

Chapter 3

Validations of the hydraulic model

In this section, the proposed model is tested with several benchmark problems, in which analytical or experimental solutions exist to quantify the numerical error. The order of accuracy are calculated as in Zlamal (1978). They are defined as:

$$\text{order} = \frac{\log\left(\|\cdot\|_{N_1} / \|\cdot\|_{N_2}\right)}{\log(N_2 / N_1)}, \quad (3.1)$$

where $\|\cdot\|_N$ denotes the norm error with a grid resolution of reference number N . This number is used to refer the number of subdivisions in each direction. The l_∞ and l_2 norms are used in this study. The l_2 norm is given by:

$$\|e\|_2 = \left[\frac{1}{N_{cell}} \sum_{i=1}^{N_{cell}} e_i^2 \right]^{1/2}, \quad (3.2)$$

where N_{cell} is the total number of cell-cantered points and $e_i = |\Phi_{nu} - \Phi_{an}|$, where Φ_{nu} and Φ_{an} are the numerical and analytical, respectively.

3.1. 3D pure advection problem

This test aims to check the performance of the proposed scheme for a pure advection problem. We consider the 3D advection equation as:

$$\frac{\partial \varphi}{\partial t} + \mathbf{u} \cdot \nabla \varphi = 0, \quad (3.3)$$

where φ is the variable, and \mathbf{u} is a prescribed flow field. In the following, the accuracy is quantified for the analytical cases of solid-body cosine bell and Zalesak's sphere advection. The effect of the MIM scheme on smooth and discontinuous solutions is examined by comparing the test cases at different resolutions.

For all test simulations, the computational domain was set as $[-1, 1] \times [-1, 1] \times [-1, 1]$. The horizontal domain is firstly divided into $N \times N$ uniform rectangles and then each rectangle is split into two right-angled triangles to represent the non-orthogonal grids. The vertical direction is also divided into N layers. The total number of grid points are ranging from 65,536 ($N=32$) to 33,554,432 ($N=256$). A constant time stepping, $dt = 0.0001$, is used. Wall boundary condition is imposed at all boundaries.

3.1.1. Cosine-Bell test

In the cosine bell advection simulation, a cosine bell is advected using the initial condition as:

$$\varphi = \begin{cases} \cos^2(2\pi r) & r \leq 0.25, \\ 0 & \text{otherwise,} \end{cases} \quad (3.4)$$

where r represents a sphere:

$$r^2 = (x + 0.5/\sqrt{2})^2 + (y - 0.5/\sqrt{2})^2 + (z + 0.5/\sqrt{2})^2, \quad (3.5)$$

and the velocity is given as a rotation flow field, given by:

$$\mathbf{u} = \left[\frac{2\pi}{\sqrt{3}}(z - y), \frac{2\pi}{\sqrt{3}}(x - z), \frac{2\pi}{\sqrt{3}}(y - x) \right]. \quad (3.6)$$

The cosine bell is continuously advected until a full revolution is completed at $t=1.0$. Figure 3.1 shows the numerical solution at different time steps for $N=128$. Although a slight deformation is observed when the sphere moves around the domain, the central scheme exhibits a very good performance in terms of absolute error. Table 3.1 analyses the accuracy using l_∞ and l_2 norm computed for the whole domain and the numerical and analytical peak values. It shows that the numerical errors reduces as the resolution increases. Note that MIM gets closer to a second order of accuracy by increasing the grid resolution.

Table 3.1 Norm errors, numerical order of accuracy and peak values

N	l_∞ norm	Order	l_2 norm	Order	Numerical peak value	Analytical peak value	Error peak value
32	0.724E+00	-	0.268E-01	-	0.51378	0.92732	0.41353
48	0.560E+00	0.638	0.195E-01	0.797	0.77838	0.97581	0.19744
64	0.415E+00	1.044	0.134E-01	1.312	0.92961	0.99556	0.06594
96	0.236E+00	1.407	0.695E-02	1.636	1.01686	0.99680	0.02006
128	0.146E+00	1.712	0.432E-02	1.692	1.00452	0.99579	0.00520
192	0.666E-01	1.885	0.211E-02	1.704	0.99062	0.99904	0.00842
256	0.381E-01	1.941	0.131E-02	1.657	0.99887	0.99982	0.00095

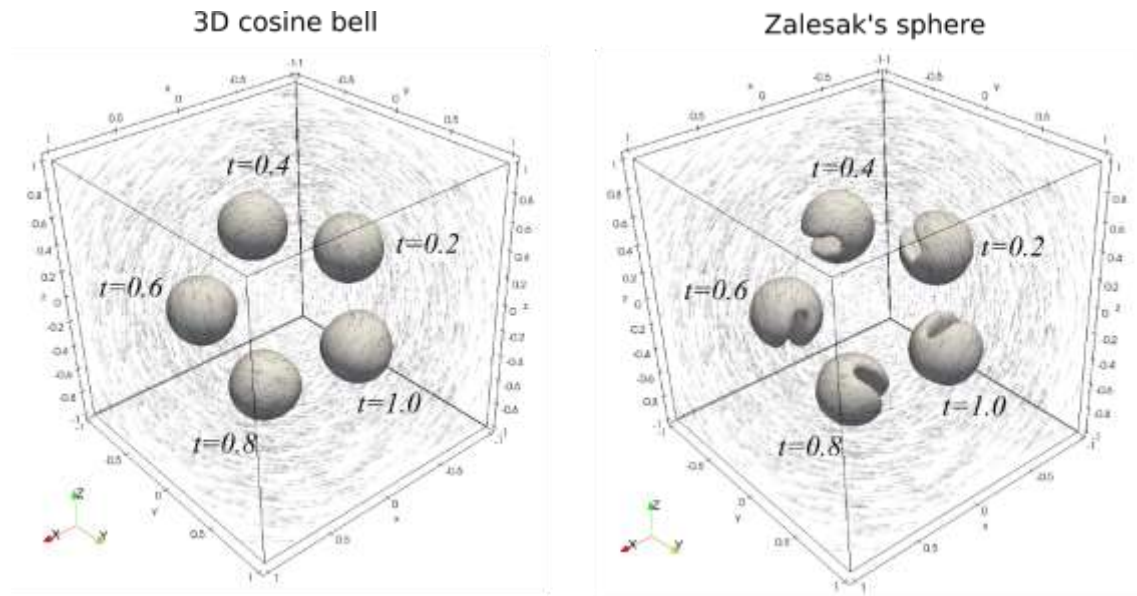


Figure 3.1: 3D cosine bell and Zalesak's sphere for advection term.

3.1.2. Zalesak's sphere test

In the previous test, the proposed scheme has shown to accurately recover an advection test case with a smooth function as the cosine bell. However, a more challenge test is the Zalesak's sphere with steep gradient (Enright et al, 2002, Zalesak, 1979). A sphere of $r=0.25$ radius with a slot of $(2/5)r$ width and $(8/5)r$ depth and undergoes a rigid body rotation. In this test case, the center location and the advection direction are the same as those used in the solid-body cosine bell advection case. The Zalesak's sphere has an initial height of $\varphi = 1$. This test case is similar that used in Kawano (2016); however, the velocity field is represented by equation (3.6) instead of a 2D vertical rotation.

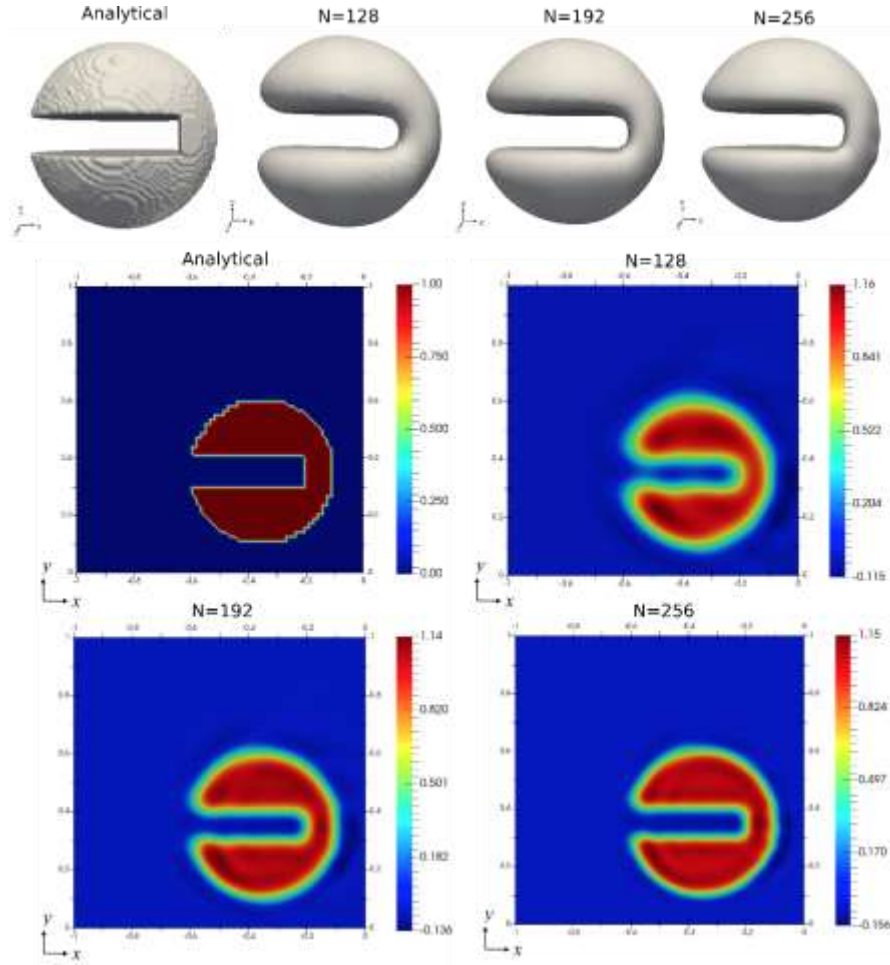


Figure 3.2: 3D contour for $\varphi = 0.9$ and the contour levels for the slice plane at $z = -0.5/\sqrt{2}$ for different resolutions.

The Zalesak's sphere completes one revolution after one unit of time. Figure 3.1 shows the evolution of the test using a grid resolution of $N=128$, and the time step $\Delta t=0.0001$. The sphere at $t=1$ coincides with its initial position. The original shape is preserved during the evolution of the Zalesak's sphere. However, the interface loses its initial shape for coarse grids (not shown here). Three different sets of grids ($N=128, 192$ and 256) were used to check the grid dependency of each method. Figure 3.2 shows the three dimensional contour for $\varphi=0.9$ and the contour levels for the slice plane $z=-0.5/\sqrt{2}$ corresponding to the initial center position of the sphere. The numerical solution away from sharp gradient regions remains close to the analytical solution. However, the solution is dispersive near sharp gradients. Figure 3.3 compares the analytical and the numerical solution at the line located at $x=-0.5/\sqrt{2}$. Note that by increasing the grid resolution, the numerical solution is closer to the analytical solution. However, there still exhibits oscillations near the interface of the

Zalesak's sphere. This is expected as central schemes could typically generate spurious oscillation at strong gradients.

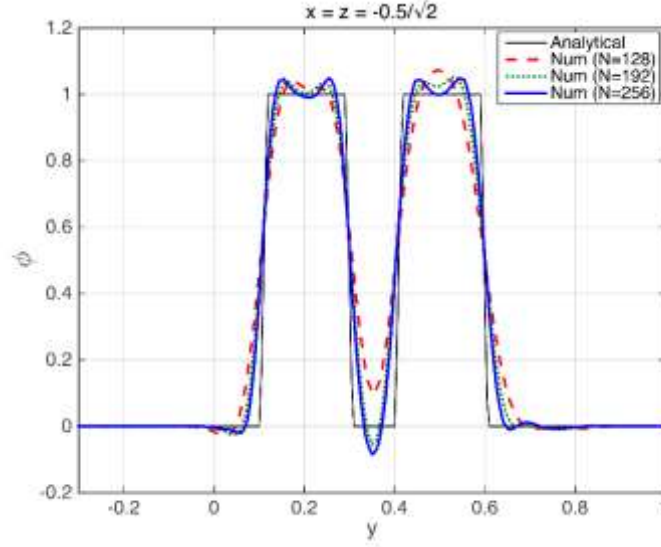


Figure 3.3: Analytical and the numerical solution at the line located at $x = -0.5/\sqrt{2}$.

3.2. 2D and 3D Taylor-Green decaying vortex

The decaying vortex has been investigated by various researchers as a benchmark test for two-dimensional unsteady flow, in which both the temporal and spatial accuracy can be demonstrated. In the present study, it is also selected as one of the validation case. For this classical test, the analytical solution of the velocity and pressure field at a certain time can be given as

$$u(x, y, t) = -\cos(\pi x) \sin(\pi y) e^{-2\pi^2 t / \text{Re}}, \quad (3.7)$$

$$v(x, y, t) = \sin(\pi x) \cos(\pi y) e^{-2\pi^2 t / \text{Re}}, \quad (3.8)$$

$$p(x, y, t) = -\frac{1}{4} \cos(2\pi x) \sin(2\pi y) e^{-4\pi^2 t / \text{Re}}, \quad (3.9)$$

The computational domain was set as $[-1, 1]$ in both x and y direction and only five vertical layers are used. Periodic condition is imposed at all boundaries to represent a 2D case, and thus to avoid any problem related to boundary conditions. In this study, the horizontal domain is firstly divided into uniform rectangles and then each rectangle is split into two right-angled triangles to represent the non-orthogonal grids. Here Reynolds number is defined

as $Re = U_{max}L/\nu$, where U_{max} is the initial maximum velocity and $L=1$ is the size of a vortex. The Reynolds number for 2D simulation is set as 20. To check the spatial accuracy, three different grids spacing are used ranging from 0.0625 to 0.01563 while a fixed time stepping size is used for all simulations and the calculated velocity field is compared to the analytical solution for $t = 0.5$. To allow for maximum time step size, the semi-implicit Crank-Nicholson method is employed for both the convection and diffusion term. To check the temporal accuracy, five different time stepping sizes are used, ranging from 0.015 to 0.1.

Figure 3.4 shows that the current scheme is clearly second order for both spatial and temporal accuracy as expected. For 3D simulations, at $Re = 1600$, a mesh resolution of $128 \times 128 \times 128$ is used and time step equals to 0.001. Figure 3.5 shows the evolution of the iso-surface of the Z-component of vortices. We can see the flow transitions to turbulence, with the creation of small scales, followed by a decay phase, similar to decaying homogeneous turbulence.

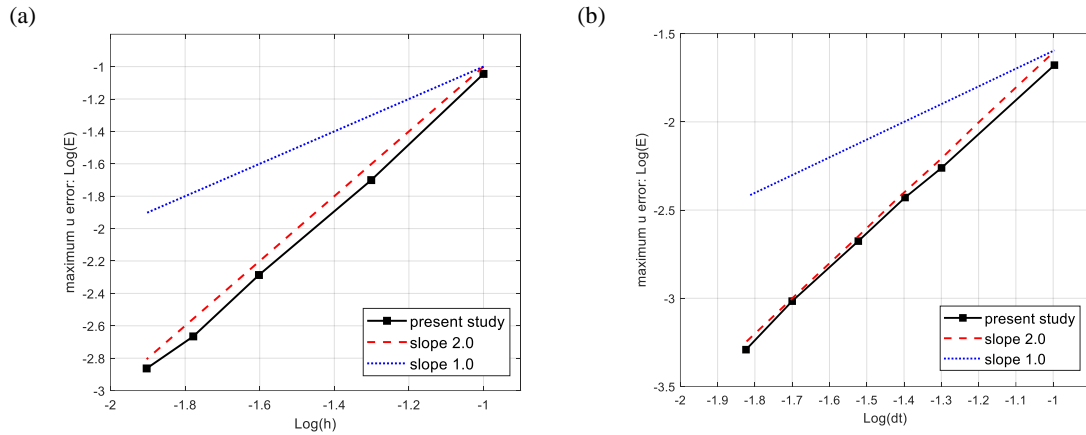


Figure 3.4: Spatial (a) and temporal (b) accuracy plots. As the slopes show the position of 1st and 2nd accuracy order of numerical schemes.

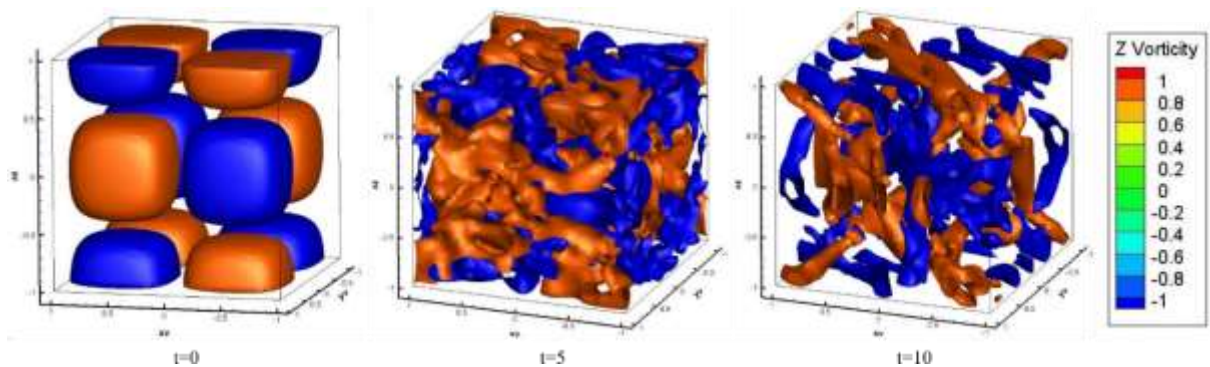


Figure 3.5: Iso-surface of the Z-component of vorticity at different time.

3.3. Lid-driven cavity flow

Another test case selected for NSMP3D is the lid-driven cavity problem, in which the top wall moves with a uniform velocity in its own plane and is a classic benchmark problem for testing and evaluating numerical techniques. Since the paper by Ghia et al. (1982), much researches have taken place using simulation or by experiment (Kim and Choi, 2000; Jan and Sheu, 2007; Mahesh et al., 2004). Although this test case is usually limited for two-dimensional and incompressible laminar flow, recent researches have shown that it can also be used in relatively high Reynolds number and three-dimensional problems using DNS or LES (Bouffanais et al., 2007).

The typical 2D computational domain for the lid-driven cavity problem is a square domain with four wall boundaries. On the top wall, a fixed constant horizontal velocity is imposed, serving as the moving lid that drives the flow. The rest of the walls are set as no-slip boundaries. In order to test NSMP3D, this problem is extended into a three-dimensional cubic domain. Two sets of boundary conditions are tested for this problem: 1) periodic boundary condition was imposed in the spanwise (Y) direction, representing a 2D problem; 2) wall boundary condition was imposed in the spanwise (Y) direction, representing a fully 3D problem. At low Reynolds numbers, the flow is expected to reach a steady state and the flow remains two-dimensional.

As report by Bouffanais et al. (2007), the critical value for onset turbulence is around 2000 to 3000, where instability appears in the downstream corner. In the present test cases, we keep the Reynolds number within the laminar regime to avoid the complication of turbulence eddies and DNS is also used to simulate a higher Reynolds number $Re=1000$ which is experimentally and numerically studied by former researchers. The non-dimensional horizontal velocity at the top wall is set to be one, whereas velocity field inside the computational domain is initialized to be zero. The steady state is achieved after a sufficient time for a 3D simulation. In horizontal direction (X-Y plane), the domain is discretized into 32×32 rectangles, for which is then divided into four triangles, representing an unstructured grid arrangement for $Re=100$ and $Re=400$, while a refined mesh is used in the corner for $Re=1000$ to capture the secondary vortex. On the vertical, uniform layers are used for all the tests.

Figure 3.6 shows the velocity profiles at the horizontal and vertical midsections for both 2D and 3D problem with the same grid resolutions with the point number in vertical $NZ=64$.

The results of Ghia et al. (1982) using fine grid configuration are also plotted for comparison. For 2D simulation, it can be seen that our results from NSMP3D with periodic boundary condition matches exactly with the reference data even with fewer mesh points. Close to the top boundary, the gradient of the streamwise velocity is relatively small, which indicates very weak shear stress. As we move close to the center, the streamwise velocity drops rapidly, indicating the presence of a vortex structure and adverse pressure gradient. Close to the bottom wall, a nearly parabolic distribution of the streamwise velocity was observed, implying that the shear stress is the dominating factor in maintaining these velocity fields. For the vertical velocity distribution (see Figure 3.6b), a nearly symmetric profile and mild velocity gradient are observed from the left to the right wall, indicating that the vertical midsection is not significantly disturbed by the vortex structure at the top but mostly affected by the confinement of the side walls.

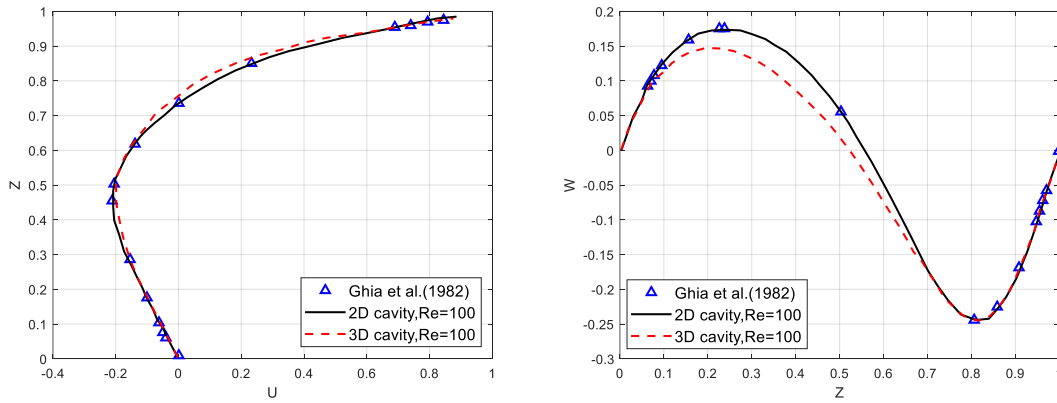


Figure 3.6: Profile of horizontal midsection velocity (u) and vertical midsection velocity (w) at $Re = 100$.

Figure 3.7 shows similar results for Reynolds number equal to 400 for both 3D and 2D problem with similar resolution, $NZ = 64$. For the 2D problems, a close match was again observed between NSMP3D and reference data. For the 3D problem, as no direct reference data was available, another 3D finite-volume method based code CgLES (Thomas and Williams, 1995; Ji et al., 2012) used in DNS mode was employed for validation. The reference code was run using the same geometry setting and boundary condition, but with a much finer grid resolution of $256 \times 256 \times 256$. The results obtained from NSMP3D and reference code were almost identical despite the difference in mesh resolutions and both have difference with the 2D data. This means that at $Re = 400$, the boundary wall has affected the flow field and the problem becomes fully three-dimensional.

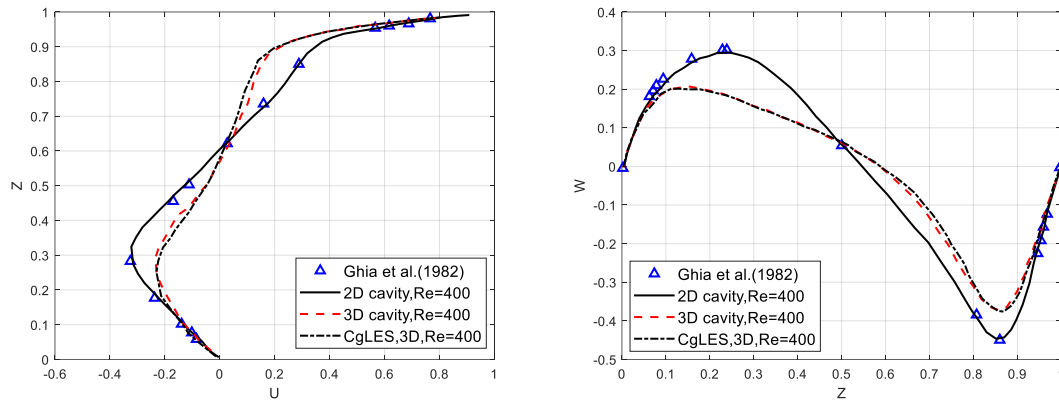


Figure 3.7: Profile of horizontal midsection velocity (u) and vertical midsection velocity (w) at $Re = 400$.

The steady state results at a vertical plane obtained from NSMP3D (at $y = 0.5$) at $Re = 1000$ is shown in Figure 3.8. From the plots, we can see that driven by the top lid, the velocity field has formed a rotational pattern with the main vortex slightly shifting into the top right section and a pair of secondary vortex near the bottom corners. From the top wall to the vortex center, the streamwise velocity gradually decreases and becomes negative as it moves away from the vortex center towards the bottom wall. The highest vertical velocity was observed to be near the top-left and top-right corner, indicating a change of flow direction due to the confinement of the sidewalls. The velocity profile given by NSMP3D compared very well with the results of Tang et al. (1995).

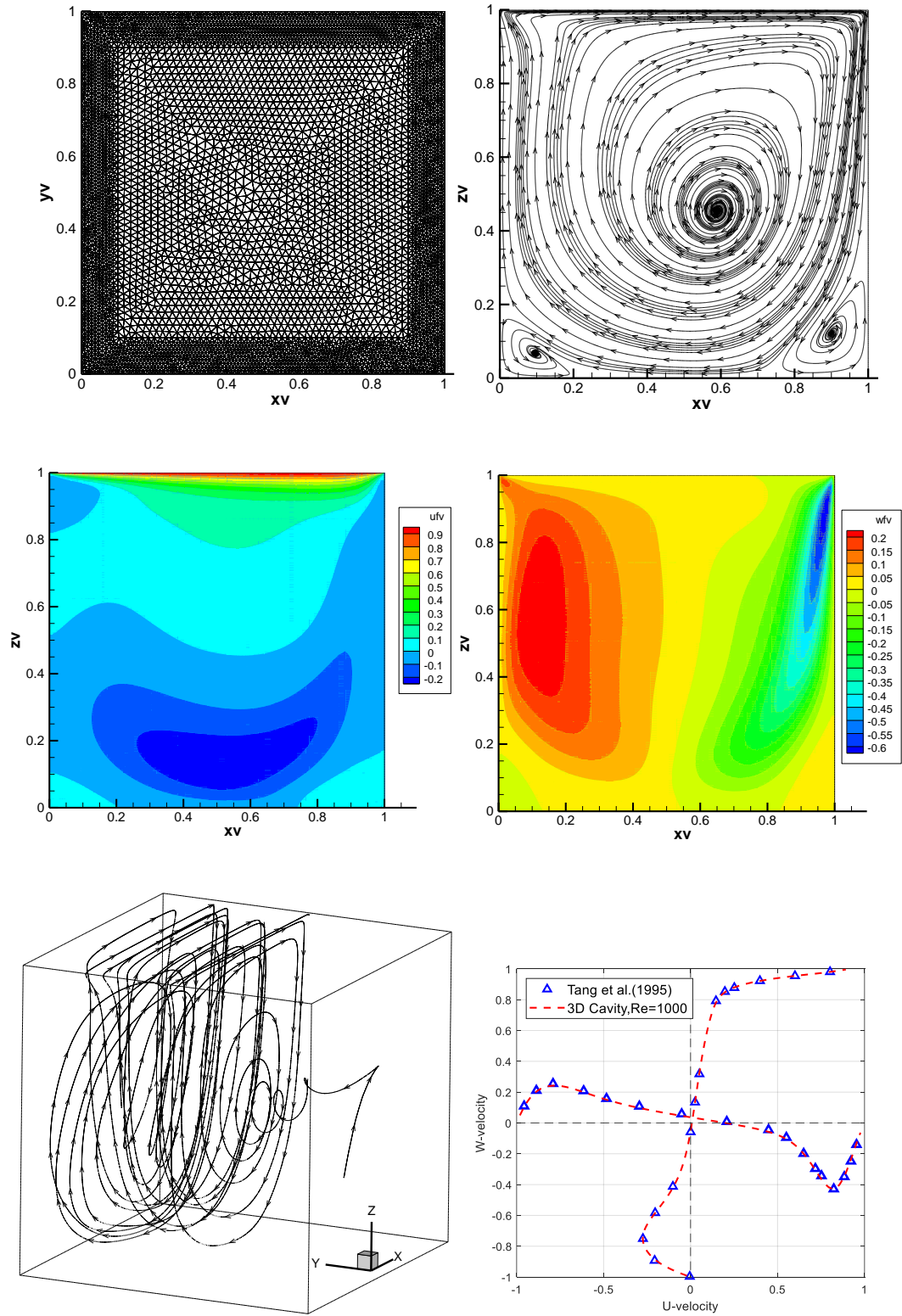


Figure 3.8: 3D cavity driven flow at $Re = 1000$. (a) Unstructured mesh with refinement resolution in the corner; (b) 2D streamlines; (c) Streamwise velocity; (d) Vertical velocity; (e) 3D streamlines; (f) Profile of midsection velocity distribution.

3.4. Standing wave in a closed basin

In the above-mentioned test cases, all simulations were done with rectangle domains where a wall boundary condition is applied or the free surface is approximated by using a stress free lid. To test the capability of simulating 3D linear waves with sigma transformation scheme, the test case of standing wave in a closed basin was selected, as it is a good example for testing mass and energy conservation when computing transient flows. Furthermore, this test case has been studied by various researchers in Cartesian coordinates system (Chen et al., 2003; Casulli, 1999; Stelling and Zijlema, 2003) and sigma-coordinate system (Ma et al., 2012; Koçyigit et al., 2002; Yuan and Wu, 2004) reproducing accurate waves with relatively few vertical layers.

For this test, we consider linear wave analytical solution based on potential flow theory, an inviscid fluid of constant density is confined in a closed basin with length $L=10m$ and width $W=10m$. The undisturbed water level is $h=10m$. The wave amplitude, A , is set to $0.1m$, 1% of the water depth so that small amplitude linear wave theory applies. The fluid is inviscid fluid of constant density. A zero initial velocity is assumed and the initial free surface elevation is given by

$$\eta(x, y, t = 0) = A \cos(kx), \quad (3.10)$$

where k is the wave number of the first sloshing mode in the x direction, i.e., $k = \pi/L$.

At the free surface, the tangential stress equals zero, the vertical velocity w satisfies the kinematic boundary conditions and zero pressure condition is applied. Free-slip boundary condition is employed on all the side and bottom walls, where the Neumann boundary condition is used for dynamic pressure. The frequency ω of the resulting wave is given by positive root of $\omega^2 = gk \tanh(kh)$ where h is the equilibrium depth. The period of oscillations for this problem is $T=3.55s$. The analytical solution for free surface elevation η is given by:

$$\eta(x, y) = A \cos(kx) \cos(\omega t). \quad (3.11)$$

Similarly, the velocity components and dynamic pressure can be derived by,

$$u(x, y, z, t) = \omega A \frac{\cosh[k(z+h)]}{\sinh(kh)} \sin(kx) \sin(\omega t), \quad (3.12)$$

$$w(x, y, z, t) = -\omega A \frac{\sinh[k(z+h)]}{\sinh(kh)} \cos(kx) \sin(\omega t), \quad (3.13)$$

$$p(x, y, z, t) = -\rho g \eta + \rho g A \frac{\cosh[k(z+h)]}{\cosh(kh)} \cos(kx) \cos(\omega t). \quad (3.14)$$

The computational domain and the initial free surface profile is shown in Figure 3.9. The basin is discretized with triangles of the horizontal plane, which are extended for the three-dimensional case in the form of prisms. The type of grid used in this simulation consists of four triangles for each of the 400 squares in the X-Y plane and the space step in the vertical direction is $\Delta z = 0.5m$, which is the same distance as the longest side of any horizontal triangle. A small-time step of $\Delta t = 0.001s$ is used for higher accuracy. The number of vertical layers used for this simulation is similar to the ones used by other authors (Chen et al., 2003; Koçyigit et al., 2002). The NSMP3D code requires that Δz is close to the maximum length of the triangular mesh to reach the desired accuracy. There are other numerical methods using fewer layers (five layers) such as the NHWAVE code developed by Ma et al. (2012) which is based on Finite Difference method. However, the velocity and pressure accuracy are not reported.

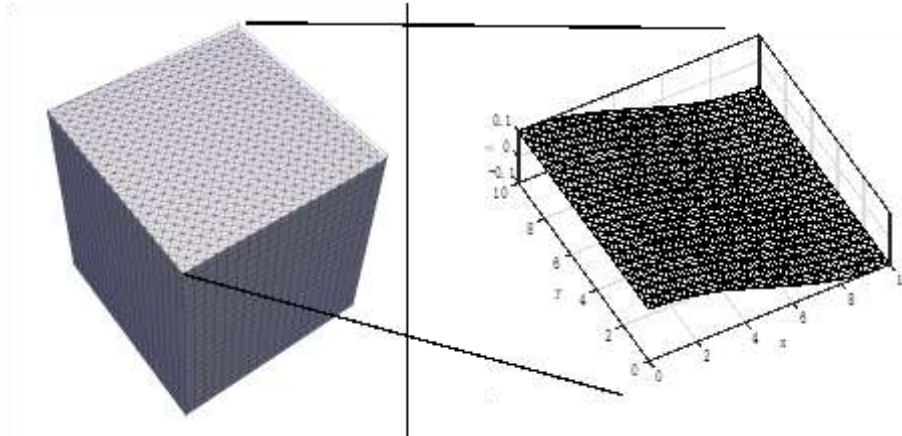


Figure 3.9: Domain discretization and initial free-surface profile for the standing wave problem in a closed basin.

Figure 3.10 shows the computed and analytical surface elevation for $t = T/2$ and $t = T$ during one period of oscillation. For better illustration, the three dimensional water elevations shown here were obtained by multiplying the solution by a scale factor of 25. As can be seen, the numerical results convincingly correspond to the analytical solution for short period waves. The greatest difference occurs close to the boundary, where the gradient of the horizontal velocity at the free surface was set as zero. We can also notice that there is no

wave propagation along the spanwise direction, which means the current numerical algorithm based on unstructured collocated grid is not interfering with extra numerical noise.

To demonstrate the behavior of the numerical solution with and without the hydrostatic pressure assumption after several periods of oscillation, comparisons between the numerical and analytical water surface elevation at $(x,y) = (2.5m, 2.5m)$ and $(x,y) = (0.25m, 0.25m)$ over four wave periods are shown in Figure 3.11. Using NSMP3D, the hydrostatic pressure is explicitly computed from the free surface elevations and the local fluid density, i.e., no Poisson equation is solved. As expected, the hydrostatic model fails to predict the wave period and a lag time between numerical and analytical results has been observed. In contrast, the surface elevations computed under the non-hydrostatic assumption are in good agreement with the analytical solution and no lag time is observed. We also notice that the approximations for the point $(x,y) = (0.25m, 0.25m)$ are less accurate than the ones of $(x,y) = (2.5m, 2.5m)$. The difference in the accuracy is directly related to the boundary conditions of the water elevation in the horizontal direction as we discussed previously.

Figure 3.12 shows a comparison between the analytical and numerical solutions of the velocity components u, v, w and pressure p along the vertical section of the basin with the non-hydrostatic model at different time instances: $t = T/2$ and $t = T$. Agreement has been achieved between numerical and analytical solutions. The greatest difference occurs in the pressure field, due to the difference in the boundary conditions at the free surface. We remark that the normalized pressure is used for displaying, which is defined as the dynamic pressure divided by the constant water density. For better visualization, the velocity vectors shown are displayed using the magnitude and are multiplied for a factor of 10 (100 for $T/2$ and T). Furthermore, comparisons of the velocity components and pressure field between the analytical solutions and numerical results at position $(x,y) = (2.25m, 2.25m)$ at the same four time instances are presented in Figure 3.13. Fair comparisons are obtained for the velocity components and the dynamic pressure, which demonstrates the capability and accuracy of the present model.

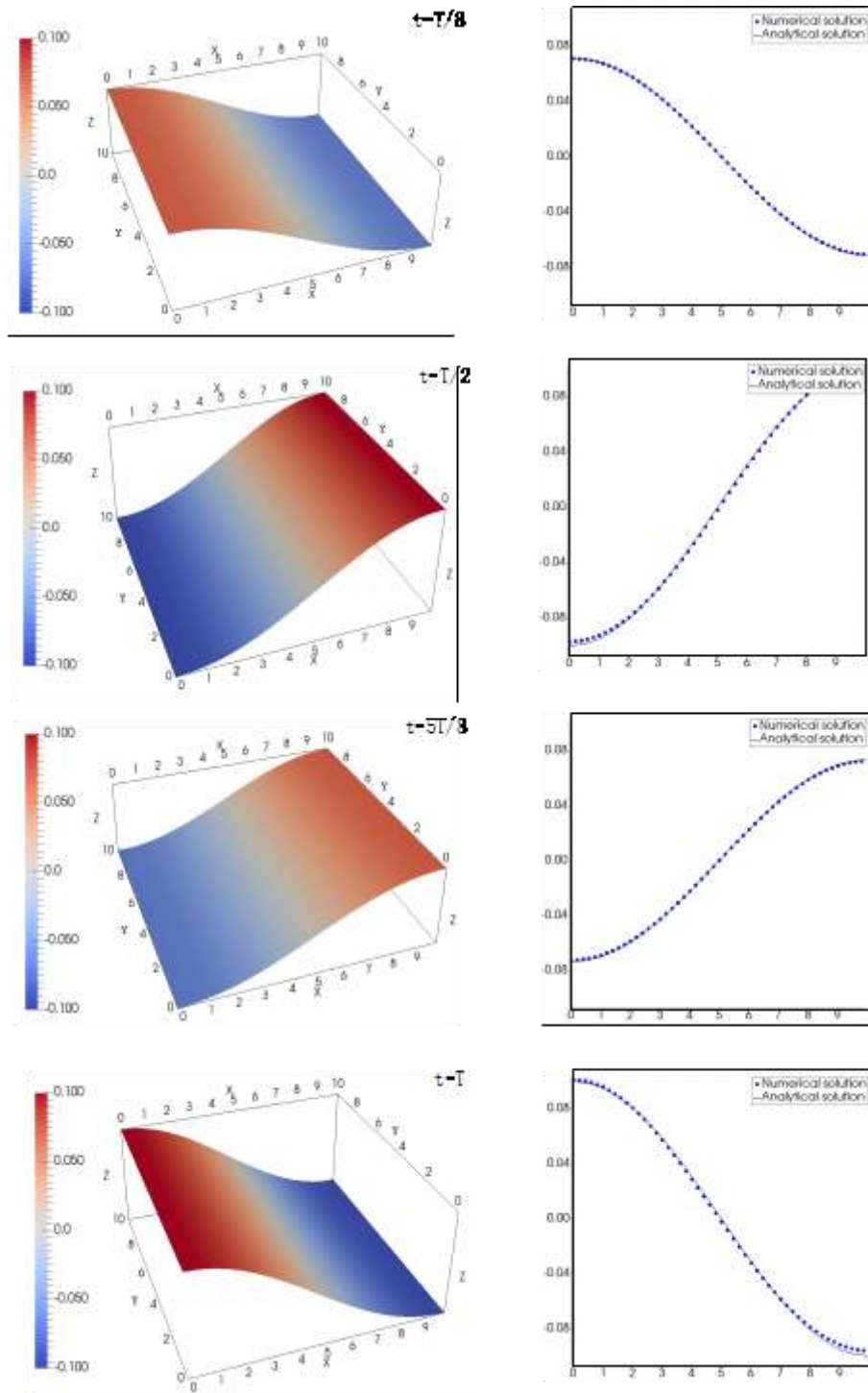


Figure 3.10: Comparison between numerical and analytical solutions of water level for: $t = T/8$, $t = T/2$, $t = 5T/8$ and $t = T$.

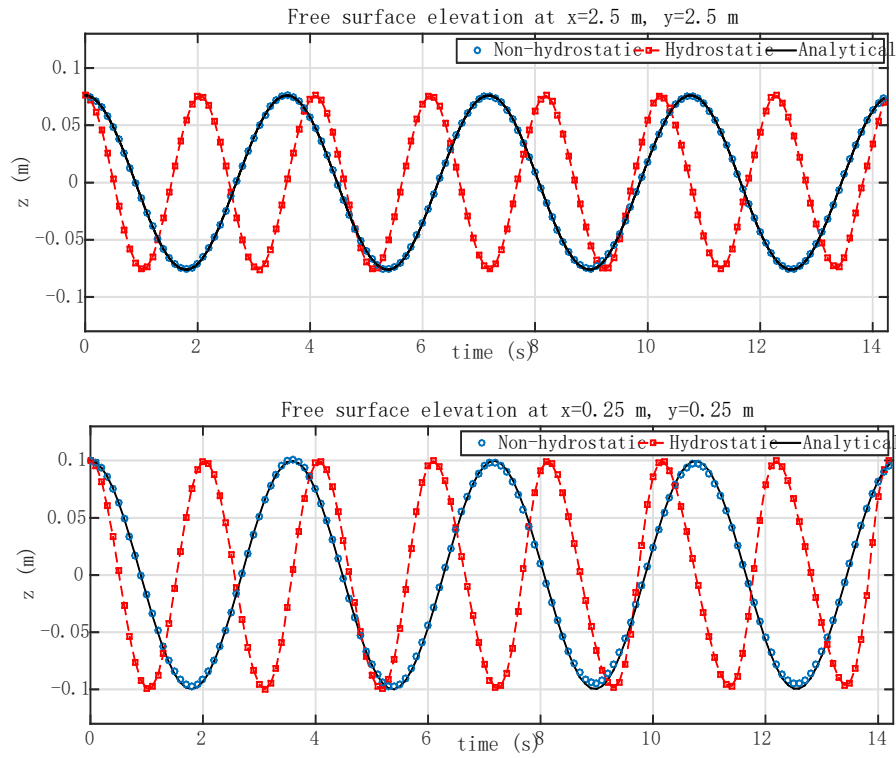


Figure 3.11: Comparisons of the free surface elevation at $(x,y) = (2.25m, 2.25m)$ and $(x,y) = (0.25m, 0.25m)$ between analytical solutions and numerical results with hydrostatic and non-hydrostatic models.

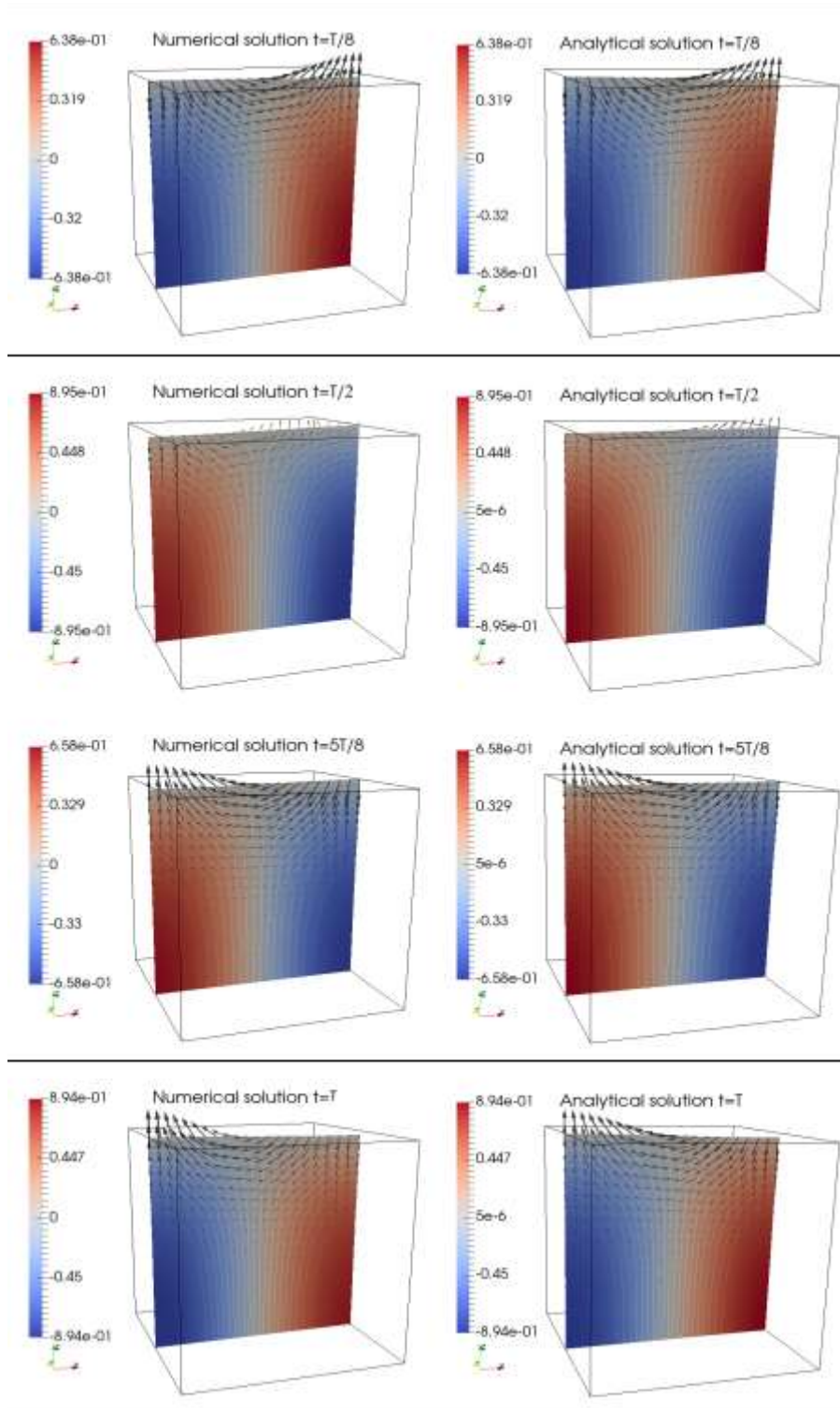


Figure 3.12: Comparison between numerical and analytical solutions of velocity and hydrodynamic pressure fields in the vertical section for: $t = T/8$, $t = T/2$, $t = 5T/8$ and $t = T$.

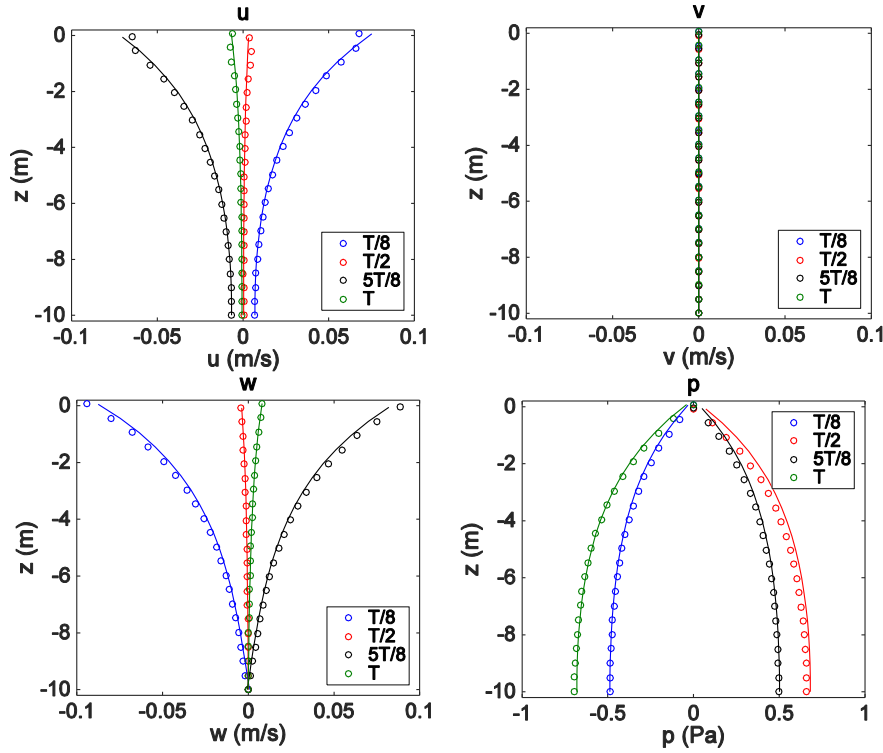


Figure 3.13: Comparison of the velocity and pressure between the analytical solutions (solid lines) and numerical results (dotted lines) at the position $(x, y) = (2.25\text{m}, 2.25\text{m})$ in four different time instances (T is the period).

3.5. Wave propagation over a submerged bar

In this example, we aim to examine the performance of our algorithm in modelling wave deformation over uneven bottoms. The test case is in a wave flume with a submerged trapezoidal bar following the experiment from Beji & Battjes. (1994). This case has been used to verify a number of non-hydrostatic free surface models (Ma et al., 2012; Cui et al., 2012). The wave flume has a length of 30 m and still water depth of 0.4 m. In this example, the wave flume has a width of 1 m. The bottom geometry consists of a submerged bar with upward slopes of 1:20 and a 2m horizontal crest followed by a downward slope of 1:10. The deep region is 0.4m and reduced to 0.1 m in the shallowest region, as shown in Figure 3.14.

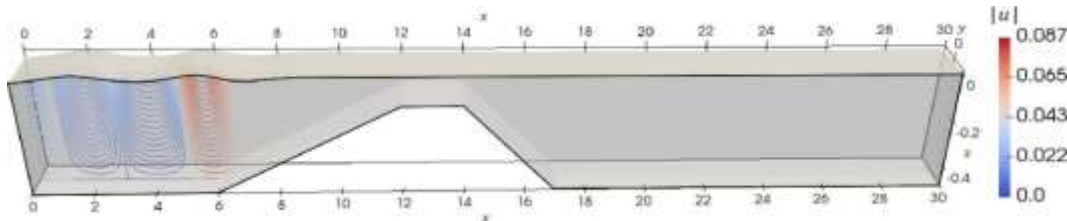


Figure 3.14: Sketch of the geometry for the Beji and Battjes test.

The surface elevation and wave velocity distribution over water depth at the incoming boundary is imposed using the Stokes' first order solution as

$$\eta = \frac{h}{2} \cos(kx - \omega t), u = \frac{h}{2} \omega \frac{\cosh[k(h+z)]}{\sinh(kh)} \cos(kx - \omega t), \quad (3.15)$$

where H is the incoming wave height, ω is the wave frequency, h is the still water depth and k is the wave number obtained from the linear wave dispersion relationship $\omega^2 = gk \tanh(kh)$. A wave with period of $2.02s$ and amplitude of $1.0cm$ is considered. At the outflow boundary, a $5m$ sponge layer with a radiation boundary is applied. The spatial gradients of water surface and velocities were set to zero at the two lateral boundaries. The computational domain is discretized by 48000 triangles with an average side length of $0.0125m$. The time step is $0.005s$ and the implicit fractional-step algorithm is used to perform the simulations.

Figure 3.15 shows the comparisons of free surface elevation at six measurement locations between numerical results and experimental data: $x=10.5m$; $x=12.5m$; $x=13.5m$; $x=14.5m$; $x=15.7m$; $x=17.3m$. Fair comparisons are obtained indicating the model's capability to simulate complex interactions between waves and uneven bottoms. The results indicates that the surface elevation at locations $x=10.5m$ and $x=12.5m$ have been well simulated by our model. The secondary wave mode at locations $x=14.5m$; $x=15.7m$ is also well predicted. Some discrepancies arise at $x=14.5m$ and $x=15.7m$, located at the back of the bar. The same discrepancies have also been found by other non-hydrostatic models (Stelling and Zijlema, 2003; Cui et al., 2012). Despite those discrepancies, the overall agreement with the experimental data is good.

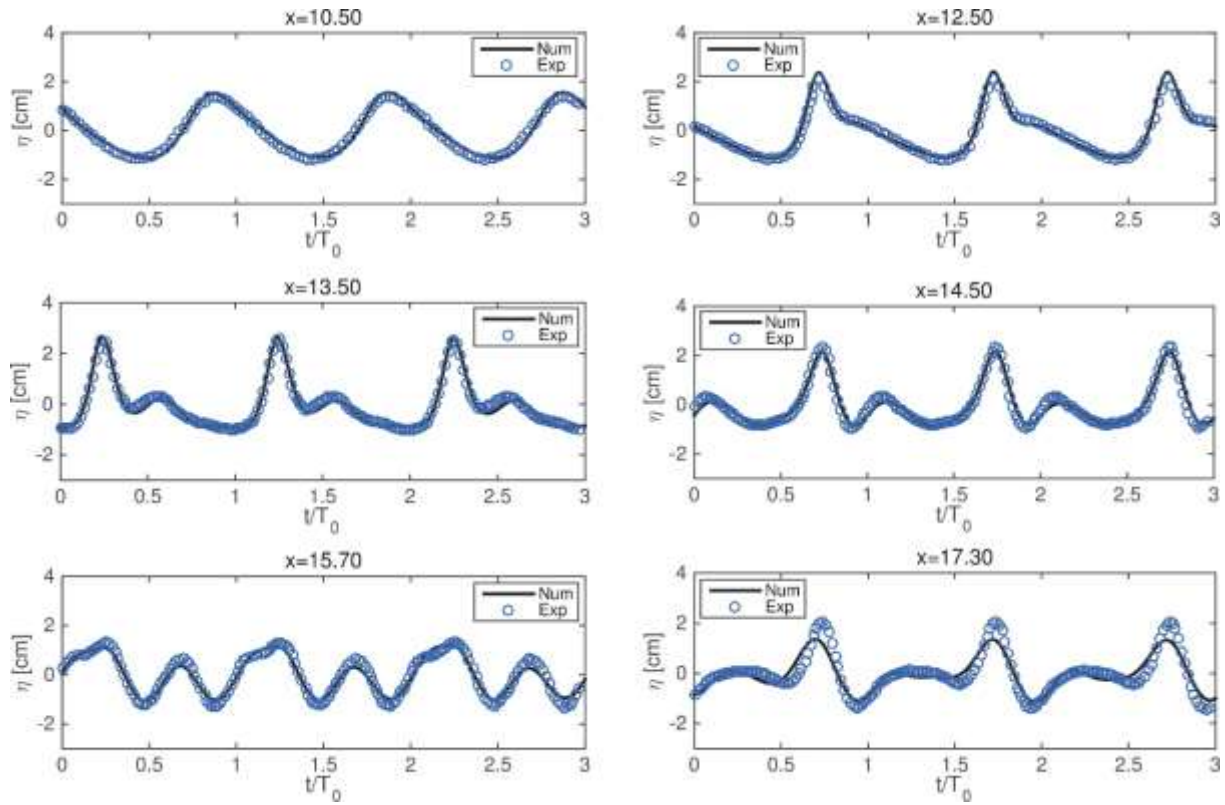


Figure 3.15: Comparisons between numerical and experimental surface elevations at $x = 10.5m$; $x = 12.5m$; $x = 13.5m$; $x = 14.5m$; $x = 15.7m$; $x = 17.3m$.

3.6. Channel flow

Channel flow represents a great interest to the engineering and science community, as most applications can be simplified into either circular or rectangular in cross section. This can also serve as a case for testing the turbulent model used in NSMP3D.

3.6.1. 2D laminar channel flow

Fully developed channel flows have been studied extensively to deepen our understanding on the mechanics of wall-bounded turbulent flows (J. Kim, Moin, & Moser, 1987). As a result, a huge number of experimental and computational studies of channel flow have been carried out, which provides us plenty of comparable results to test the computation capacity of our code in high Reynolds numbers.

The 2D laminar flow on an inclined bed driven by gravity is studied. For the channel flow with small slope $\alpha = \sin\alpha$, the flow velocity on top can be obtained analytically,

$$u = \frac{\alpha g h^2}{2\nu}, \quad (3.16)$$

where ν is the kinematic viscosity of water, h is the water depth and g is gravitational force. At low Reynolds numbers, the laminar flow in a channel can be described by Poiseuille's law, following a parabolic equation:

$$\frac{u(z)}{u} = \frac{z}{h} \left(2 - \frac{z}{h} \right), \quad (3.17)$$

where z denotes the vertical distance from the bed. In this study, the channel slope is set as $\alpha = 0.0113m/m$. Body force (f_x, f_z) is used to represent the gravity force. Normalized by the bed friction velocity ($u_\tau = \sqrt{\alpha g h}$) and the water depth, this non-dimensional body force can be calculated as

$$f_x = \frac{\alpha g}{u_\tau^2 / h} = 1.0 \quad \text{and} \quad f_z = \frac{g}{u_\tau^2 / h} = 88.5. \quad (3.18)$$

The channel's dimension is $6h \times 4h \times 2h$ in x, y, z direction. Periodic boundary condition is imposed in the streamwise and spanwise direction. Both the top and bottom boundaries were set as no-slip wall. The Reynolds number based on the friction velocity ($Re_\tau = u_\tau h / \nu_w$) of 5 was used for the current simulation and non-dimensional velocity u^+ on top can be obtained by

$$u^+ = \frac{u}{u_\tau} = \frac{\alpha g h^2}{2\nu_w \sqrt{\alpha g h}} = 2.5. \quad (3.19)$$

The Reynolds number based on the velocity on top ($Re = uh / \nu_w = u^+ Re_\tau$) can be found to be 12.5. The mesh is composed of 64×64 grid points (Figure 3.16), resulting $\Delta x^+ = 0.2344$ and $\Delta y^+ = 0.1563$. The initial flow field is set to zero for the entire domain and is driven by the horizontal body force in the water region. The time step is fixed at $dt = 0.0005$, the simulation duration is $T = 40$ non-dimensional time units. The final steady velocity field is achieved when the streamwise velocity profile at each cross-section has become identical.

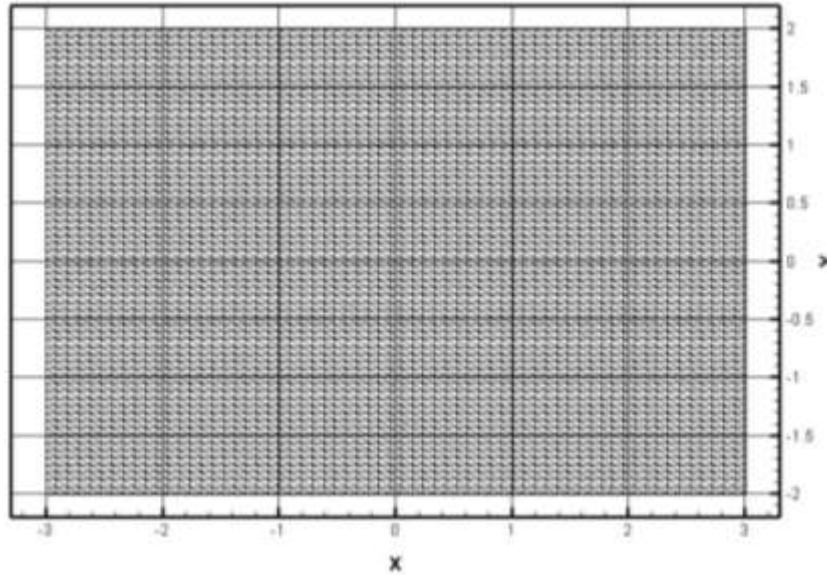


Figure 3.16: Mesh description for 2D Channel flow.

Figure 3.17 shows the contour of streamwise velocity field and velocity vectors with a parabolic profile at steady state. Velocity profiles shown in Figure 3.18a are compared with the analytical solution. It can be seen that the velocity profiles from the present computation match exactly with the analytical solution at $t = 40$, and the normalized free surface velocity is found to be 2.5. Normalized by the analytical shear stress ($\tau = \rho u_{\tau}^2$) at the bottom wall, shear stress compared with analytical solution is shown in the Figure 3.18b. It can be seen that the velocity profiles from current simulation match exactly with the theoretical results except the bottom boundaries in the shear stress profile.

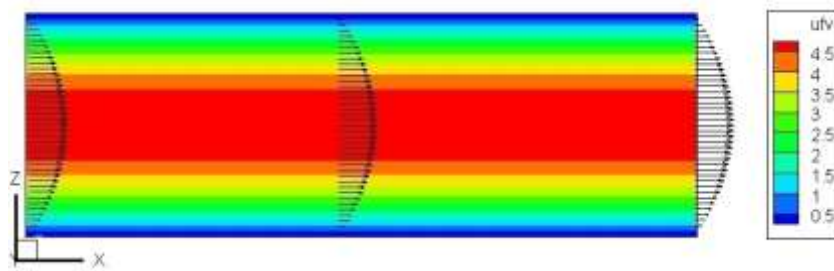


Figure 3.17: Steady streamwise velocity vector field for 2D channel flow.

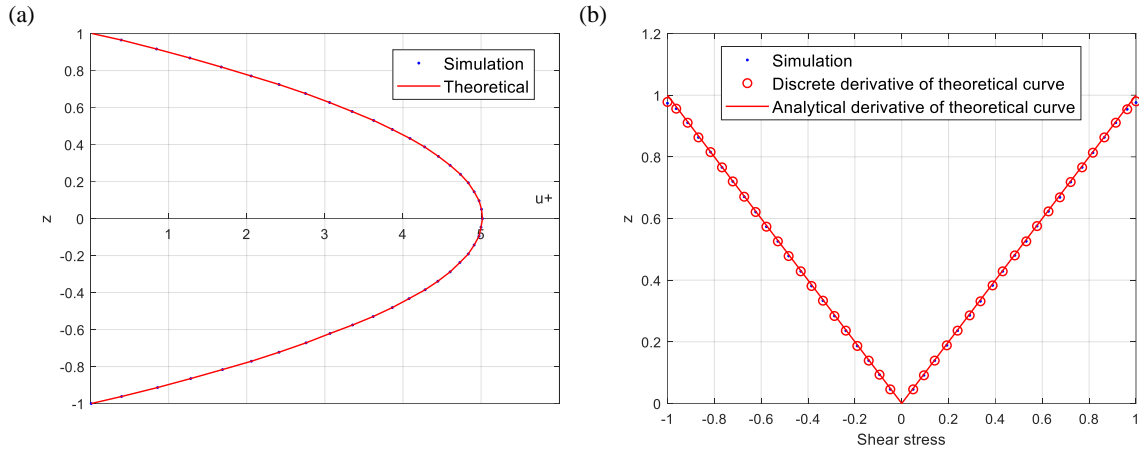


Figure 3.18: 2D laminar channel flow: (a) Streamwise velocity profile at $x = 2.5$, $y = 0$; (b) Shear stress profile.

3.6.2. Turbulent channel flow

Periodic boundary condition was applied in the streamwise and spanwise directions and a constant body force f_x of 1.0 was used to drive the flow. No-slip boundary condition is used on bottom surface and free-slip boundary on the top. The initial velocity fields are set as random perturbation field.

3.6.2.1. Direct numerical simulation (DNS) of turbulent channel flow

The Reynolds number based on the friction velocity ($Re_\tau = u_\tau h / \nu_w$) is set as 180 to match Kim et al. (1987). The Reynolds number based on the mean surface velocity (U_s) and half channel depth (h) is given by $Re = U_s h / \nu_w = U_s / u_\tau Re_\tau = 3258$, where U_s / U_τ is determined from the simulation. The computational domain is set as $6h \times 4h \times 2h$ in x , y , z direction respectively. The horizontal plane is discretized on structured triangle grid of 128×84 while 128 irregular layers are used in the vertical direction. The values of the grid spacing in terms of wall units is found to be $\Delta x^+ = 16$, $\Delta y^+ = 11$ and $\Delta z_{max}^+ = 4.2$. The center of the first layer grids is located at $z^+ \approx 0.7$, which is within the laminar boundary layer. The time step is fixed at $dt = 0.0003$ to keep the Courant number smaller than 1.0 during the whole simulation. The case is run for 100 non-dimensional time units and plane-averaged turbulence statistics values are gathered from $t^+ = 70$ to $t^+ = 100$.

The mean velocity profile at different vertical layers is shown in Figure 3.19 along with the reference DNS data of Kim et al. (1987). In general, the current result exhibits good capability in capturing the mean flow field, with the first point sits in the viscous sub-layer. In the buffer region, small discrepancy with the reference data can be observed in this region

with a smaller mean velocity. In the region ($z^+ > 20$), the computed results closely follows the log-law, denoting a full developed turbulent flow. Clearly, our DNS results show the capability of the proposed model in simulating turbulent flows. Using the iso-surface Q -criterion of instantaneous flow, Figure 3.20 shows tube-like vertical structures, which are randomly distributed over the turbulent flow field (Nagaosa, 1999).

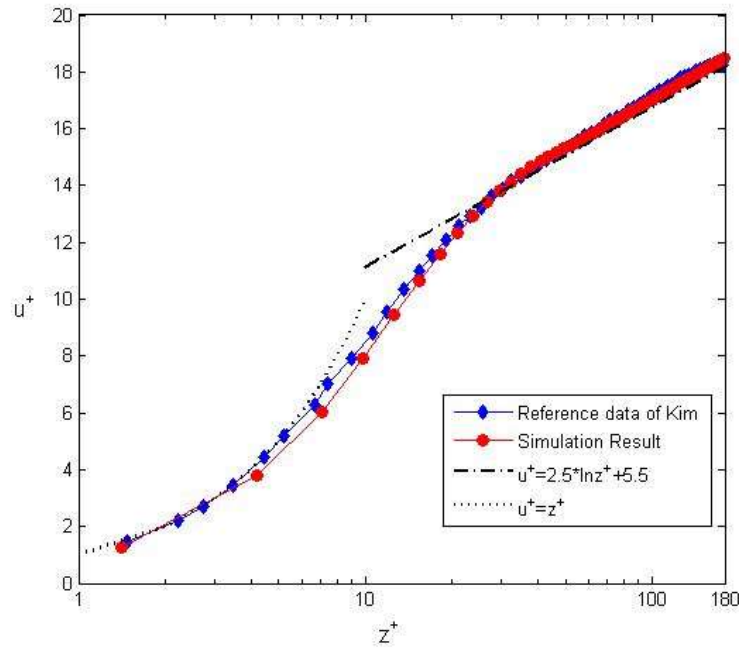


Figure 3.19: Mean streamwise velocity distribution in wall units by direct numerical simulation.

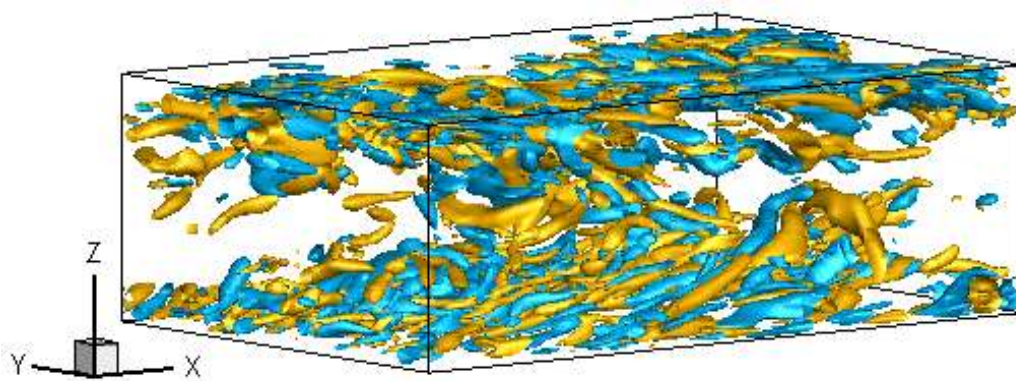


Figure 3.20: Iso-surface of Q -criterion field showing direct simulation of turbulent structure in the channel flows.

3.6.2.2. Large eddy simulation (LES) of turbulent channel flows

Large eddy simulation is carried out at the friction Reynolds number as 395. Computations have been performed using the constant coefficient Smagorinsky sub-grid scale model ($C_s = 0.1$). The initial condition and boundary condition are set as the same as the above DNS cases, while computational domain is $2\pi h \times \pi h \times 2h$ in x, y, z direction with two computational grids are $64 \times 64 \times 64$ and $96 \times 96 \times 96$ respectively. The wall normal grid is stretched by using a hyperbolic-tangent type stretching function:

$$z(j) = \frac{\tanh(2.25 \times (\frac{2j}{N} - 1))}{\tanh(2.25)}, j = 0, 1, \dots, N \quad (3.20)$$

The grid spacing for coarse mesh in the streamwise and spanwise directions are $\Delta x^+ = 38$, $\Delta y^+ = 19$ and the first mesh point away from the wall is at $z^+ \approx 1.4$ and $\Delta z_{max}^+ = 28.2$; while for fine mesh, the grid space is $\Delta x^+ = 26$, $\Delta y^+ = 13$, $\Delta z_{min}^+ = 0.86$, $\Delta z_{max}^+ = 18.92$. The time step is fixed at $dt = 0.0005$, the simulation duration is 80 non-dimensional time units. The plane-averaged turbulence statistics values are gathered from $t^+ = 60$ to $t^+ = 80$.

Jarrin (2008) and Okong'O et al. (2000) are chosen as references, in which LES has been used in an unstructured grid. Figure 3.21 shows the planar average of time-averaged velocity, normalized by the friction velocity. The experimental log-law from Eckelmann (1974) is $u^+ = 2.65 \ln z^+ + 5.9$ for a nearby friction Reynolds number cases. Obviously, our LES result using coarse mesh has excellent agreement with experimental data of Eckelmann (1974) and unstructured numerical data from Okong'O et al. (2000) and Jarrin (2008). Using fine mesh, Our LES result is close to numerical results of Jarrin (2008) with the same mesh, the predicted velocities from both are very slightly higher than the log law $u^+ = 2.5 \ln z^+ + 5.5$ given by Kim et al. (1987) using DNS. A discrepancy of about 6% between DNS and Experimental results from Eckelmann (1974) has been observed. The explanation about this discrepancy can be found in Kim et al. (1987)..

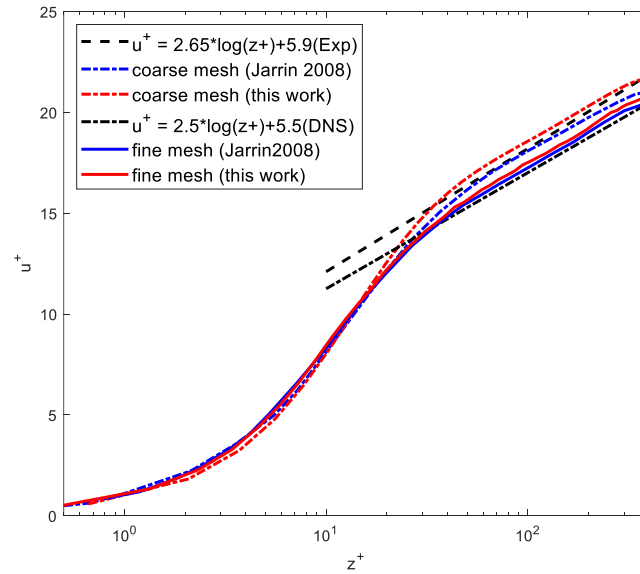


Figure 3.21: Large eddy simulation of mean streamwise velocity distribution in wall units.

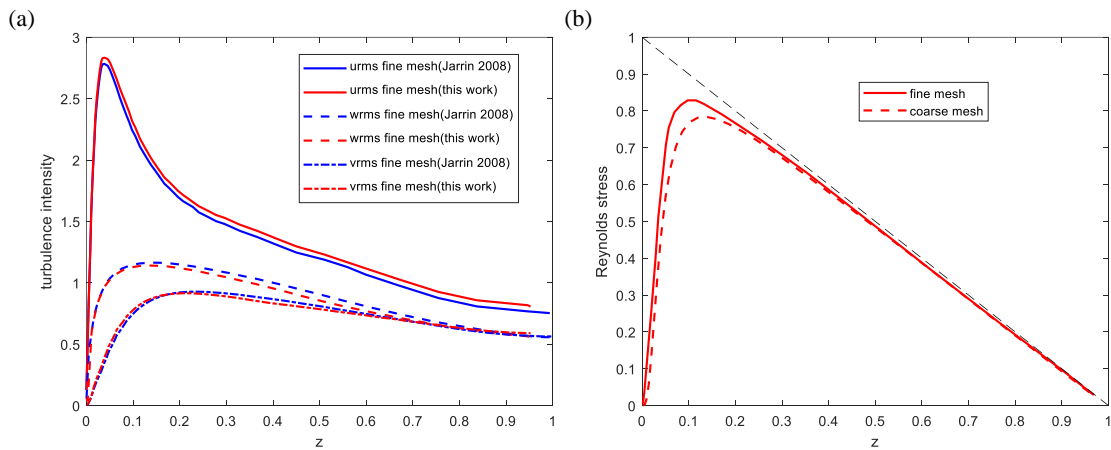


Figure 3.22: Large eddy simulation of the turbulent channel flow: (a) Streamwise turbulence intensity using coarse mesh and (b) Reynolds stress

The computed streamwise turbulent intensity (u_{rms} , v_{rms} , w_{rms}) and Reynolds stress using fine mesh are shown in Figure 3.22. The tendency of our results are in good agreement with the reference data, with a very slightly difference of the turbulent intensity, compared with the references in streamwise direction. Our results exhibit increased turbulence generation in the buffer region, which leads to a higher turbulence intensity and a higher mean velocity profile. Using iso-surface Q -criterion of instantaneous flow in the lower half part, Figure 3.23 shows hairpin structures, which are randomly distributed over the turbulent flow field and an instantaneous velocity profile in the full channel.

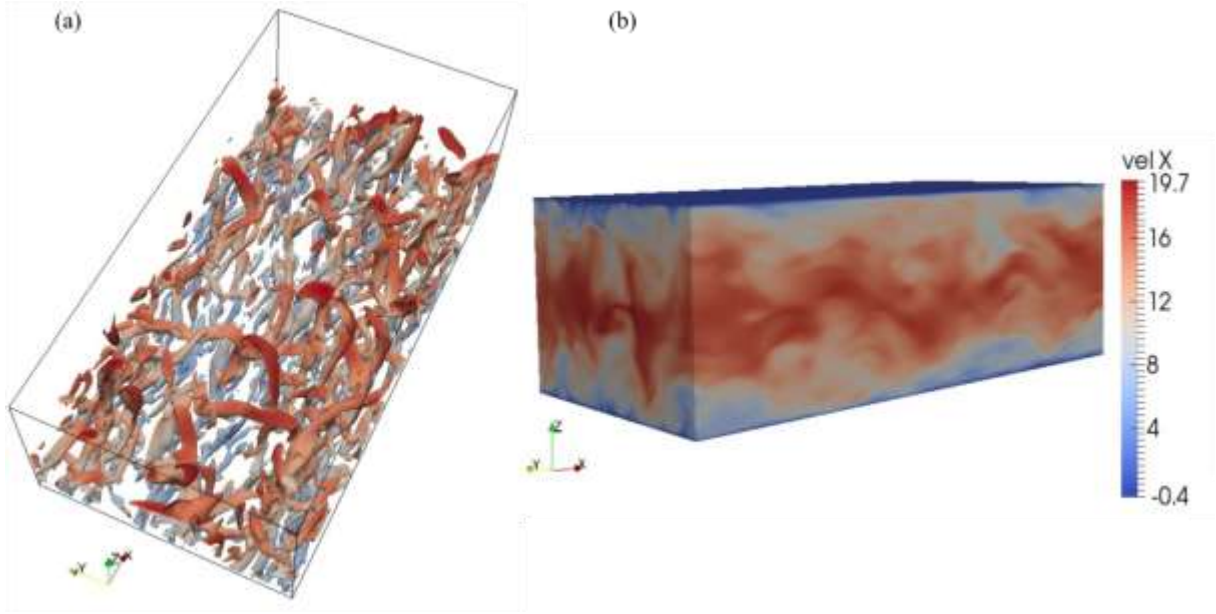


Figure 3.23: Large eddy simulation of of the turbulent channel flow: (a) Iso-surface of Q-criterion field showing turbulent structure and (b) Instantaneous velocity profile.

3.7. Speed-up test

In this section, some numerical results are reported to demonstrate the effectiveness of the proposed parallel methods. Different number of processors are performed to measure the parallel efficiency and the results have been obtained after averaging over several simulations of the same problems. Performances are evaluated in terms of speedup and efficiency. The speedup S_p is defined as $S_p = T_1/T_p$ and the efficiency E is defined as $E_p = T_1/(n_p T_p)$ where T_1 is the execution time of the serial algorithm and T_p is the execution time of the parallel algorithm with n_p processors.

We applied our parallel solver to standing wave in a closed basin case corresponding to the solitary wave propagation in a channel problem. In this case, we can easily control the size and distribution of the sub-domains, and measure their influence on the parallel performance. To test the performance of the solvers, a mesh of 80 000, 320 000 and 5 120 000 prisms have been generated, (right triangular elements and 20 layers) and $\Delta t = 0.01s$. The sub-domains are taken by dividing n_p times the 3D domain in the x -direction.

The performance of the parallel methods is investigated in Figure 3.24. It shows the total CPU time, the speedup and efficiency up to $t = 0.5s$ starting from 2 up to 20 processors. Inner calculations in each sub-domain are reduced as the number of processors increases and the

total CPU time decreases as the number of processors increases. It can also be noticed that the speedup deviates from the ideal speedup line as the number of processors increases because an increased communication time between blocks. Nevertheless, the speed up improves with the size of the problem. Such effect is due to the growth of the computational time spent in the inner computations with the problem size.

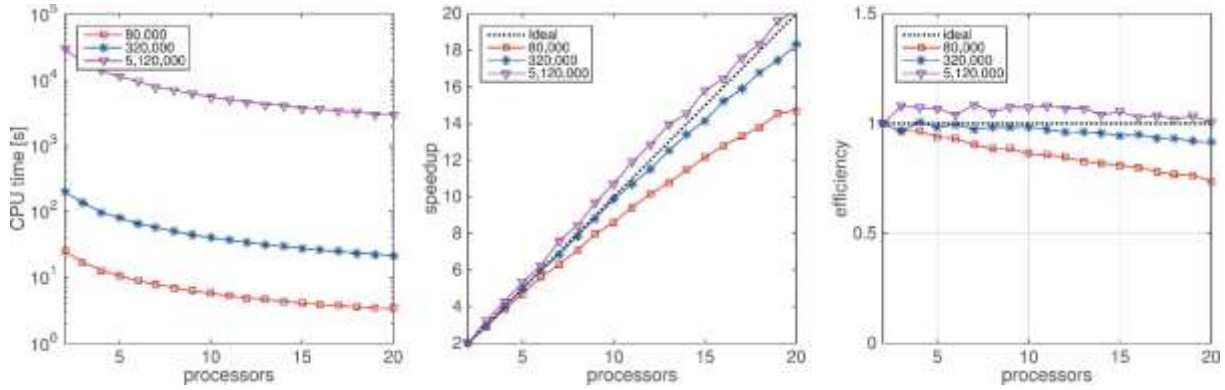


Figure 3.24: Performance of the solitary wave propagation in a channel problem using different number of processors and mesh resolutions.

3.8. Conclusion

The proposed scheme is tested by several benchmark test cases for accuracy and computational efficiency and can be applied to unsteady flow problems with a complex geometry. The test case of 2D decaying vortex shows that NSMP3D gets second order of accuracy in space and in time and is used in comparison with the analytical solution. The test case of lid-driven cavity flows shows that NSMP3D can provide the results equivalent to those obtained from previous numerical studies, even they used finer computational meshes. 3D standing wave in a closed basin checks the ability of NSMP3D in simulating free-surface and non-hydrostatic flow using sigma-coordinates system in comparison with small amplitude linear wave theory. From the validation on selected and relevant test cases, the proposed scheme yields an accurate and robust solution for three-dimensional problems at relatively low cost.

Chapter 4

3D simulations of scour around an obstacle

In order to prove the capacity of NSMP3D in handling unsteady flows and vortex shedding, the classic test case of 2D flows around a cylinder is carried out with increasing Reynolds numbers. The numerical results are compared with experimental and numerical data given in the literature (Ghia et al., 1982; Thom, 1933; Nishioka and Sato, 1974). Then, a test case on 3D free-surface, non-hydrostatic flows around a cylinder will be presented. The comparison between our numerical results with experimental results obtained with high Reynolds numbers and different Froude number will be given.

4.1. Flow around a cylinder on flat bed with rigid surface

The flows around a circular cylinder, significantly varying with cylinder Reynolds numbers, have long been a benchmark problem (Kim & Choi, 2000) for validating external flows. It is known that at lower Reynolds numbers ($Re_D < 47$), the flow will form a stable recirculation bubble behind the cylinder. When Re_D increases up to 200, a stable vortex shedding is formed and the flow remains two-dimensional. While Re_D are higher than 1000, flows become fully three-dimensional.

4.1.1. Low Reynolds number cases

A various number of Reynolds numbers have been selected for this benchmark test, ranging from 50 to 3,900. The diameter for the cylinder is set as one. The computational domain is set as $[-10, 20]$ in the streamwise direction, $[-15, 15]$ in the spanwise direction to develop a free outflow. A uniform Dirichlet inflow boundary condition is imposed at the inlet,

with a non-dimensional unit velocity. In the spanwise direction, free slip boundary condition is used to minimise the effect of wall boundaries. In the vertical direction, periodic boundary condition is used to mimic an infinite long cylinder. The element counting for the computational domain in X-Y direction is about 20,000 with 20 layers are used in vertical. To ensure the first layer points lie within the boundary layer, 157 mesh points are constructed around the cylinder and the distance from the first layer cell centers to the wall is about $\delta=0.01$. In a recent numerical study carried out by (Qu et al., 2013), a rectangle domain of similar dimension as the present study was used but with a closer distance of the first grid point away from the wall ($\delta=0.005$). All the simulations are initially run for a duration of 100 time units (D/U) until the solution is statistically stable and then the simulation is restarted for another 300 time units to gather the time averaged data.

The steady state recirculation bubble and pressure near the cylinder at $Re_D = 40$ is shown in Figure 4.1. The present result shows smooth instantaneous pressure contours, indicating few pressure oscillations in the proposed scheme.

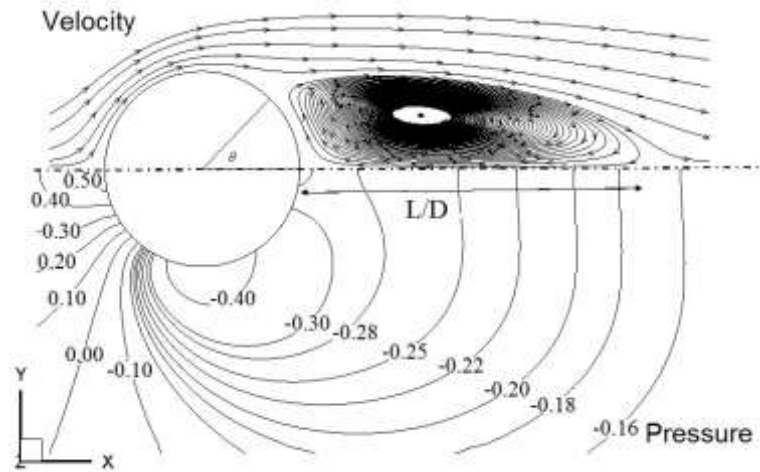


Figure 4.1: Bubble characteristics for $Re_D = 40$.

The evolution of the recirculation-area length as a function of the Reynolds number is shown in Figure 4.2a. From the time-averaged stats, it can be seen that the length of the recirculation area moves towards the cylinder body as the Reynolds number increases. The calculated recirculation-area length is compared to the experimental measurement of Nishioka and Sato (1974) and the computational result of Park et al. (1998), who have used a fine mesh consisting of 641×241 grid points. A fair agreement was found between the present result and the reference data. Figure 4.2b shows the Strouhal number as a function of the Reynolds number, which indicates the vortex shedding frequency for each case. Williamson

(1989) studied the oblique and parallel vortex shedding in the wake of a circular cylinder at low Reynolds numbers and pointed out that the Strouhal-Reynolds number relationship are closely related to the transition of the mode of vortex shedding. In a recent numerical study carried out by Qu et al. (2013), a rectangle domain, similar in size to that of the present study, was used but with a closer distance to the first grid point away from the wall ($\delta = 0.005$). An excellent agreement is found among all three results.

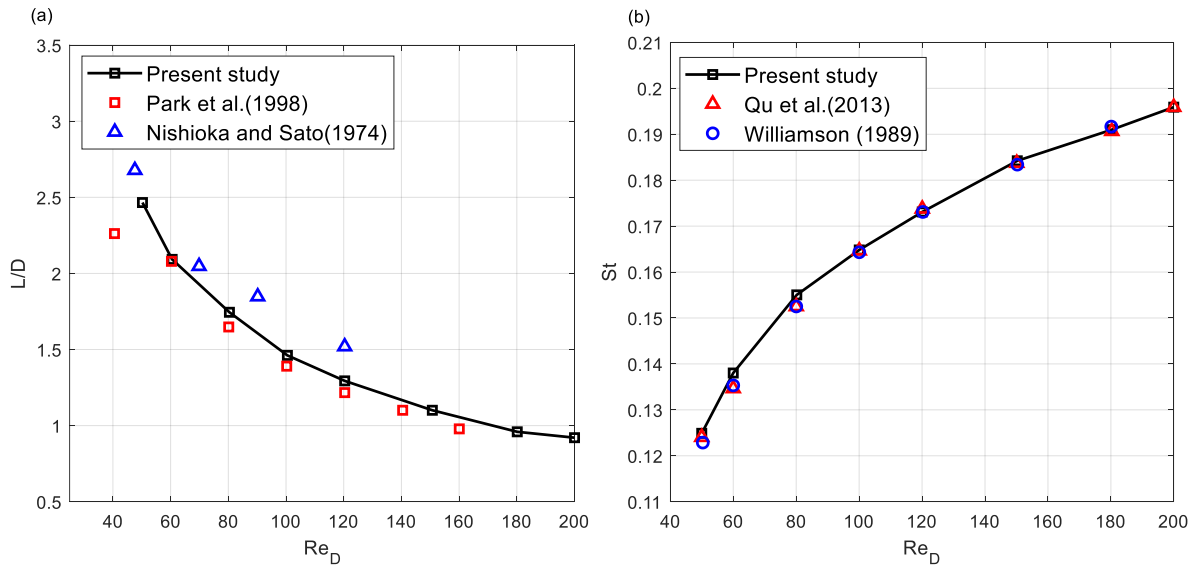


Figure 4.2: Evolution of (a) Reattachment length and (b) Strouhal number.

Figure 4.3 shows the time averaged pressure coefficient around the cylinder surface for two different Reynolds numbers, plotted along with measurement from Homann (1936) and Thom (1933) and numerical result from Rajani et al. (2009). The current result agrees well with the reference data. For $Re_D > 47$, with the increase of Reynolds number, an increase of the negative pressure was noticed, especially from the base suction point at the back of the cylinder. The point of the largest negative pressure coefficient moved upstream, indicating a shift in the mean separation point, due to the decreasing thickness of the wall shear layers and increasing vortex shedding. This finding is also supported by the reduction of the length of the recirculation bubble as shown in Figure 4.2. At the frontal stagnation point, the decrease in time averaged pressure coefficient is smaller when compared with the base suction points, which means the base pressure is more sensitive to the dynamics of wake.

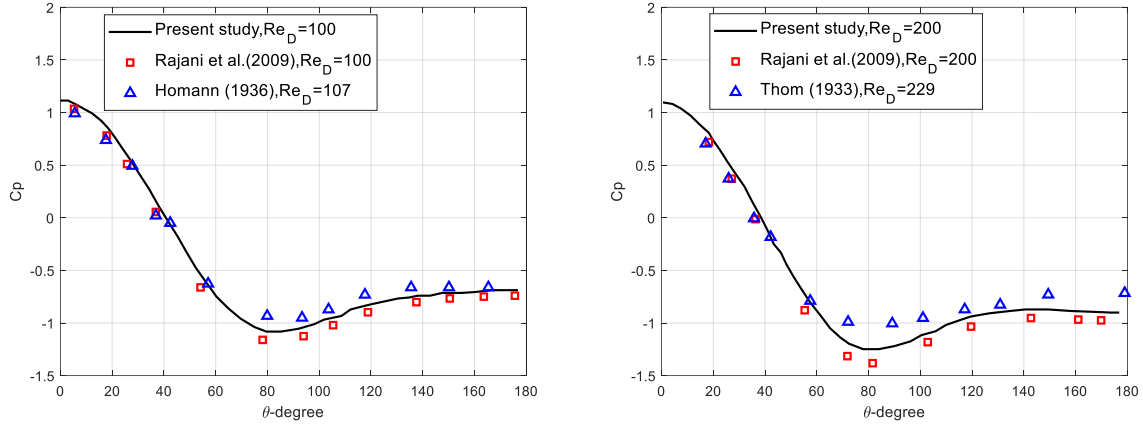


Figure 4.3: Time averaged pressure coefficient at different Reynolds numbers.

Results on drag and lift coefficient and vorticity contour are shown in Table 4.1 and Figure 4.4, respectively. For drag and lift coefficient, the first value is the time averaged mean value, and the values after ' \pm ' denote the maximum deviation from the time averaged value. From Table 4.1, the mean drag coefficients decrease with the increase of Reynolds numbers, while the oscillation amplitude increases continuously. Quantitatively, the present scheme tends to have over-predicted values as compared with other numerical results, especially with data from Qu et al. (2013) for low Reynolds numbers. This deviation can be explained due to the difference in the size of computational domain, spatial/temporal resolution, as well as the boundary conditions.

Table 4.1 Drag and lift coefficients for unsteady flow past a cylinder at various Reynolds numbers

Re_D	Present results		Park et al. (1998)		Mittal (2005)	Qu et al. (2013)
	C_d	C_l	C_d	C_l	C_d	C_d
50	1.476 ± 0.005	± 0.062	-	-	1.416	1.397
60	1.432 ± 0.006	± 0.146	1.39	± 0.1344	-	1.377
80	1.389 ± 0.007	± 0.340	1.35	± 0.2452	-	1.336
100	1.374 ± 0.044	± 0.341	1.33	± 0.3321	1.322	1.317
120	1.361 ± 0.018	± 0.420	1.32	± 0.4103	-	1.306
150	1.357 ± 0.028	± 0.526	-	-	-	1.305
200	1.347 ± 0.045	± 0.673	-	-	1.327	1.316

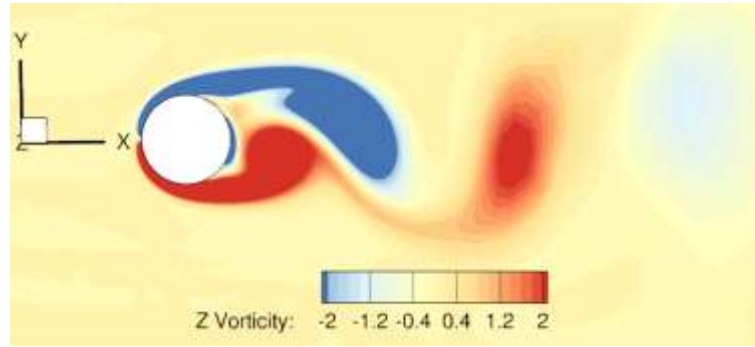


Figure 4.4: Instantaneous plot of the vortex shedding at $Re_D = 200$.

A comparison between our numerical and experimental results is presented on a free slip bed at $Re_D = 3,900$. The vertical mean streamwise (u/U) and spanwise velocity (v/U) components at five different stations, $x/D = 1.06, 2.02, 3.0, 4.0$ and 5.0 , are plotted in Figure 4.5. A U-shaped profile is observed near the wake region. The experimental data LS93 and OW93 were obtained from Lourenco (1993) and Ong & Wallace (1996), respectively. LES B16 corresponds to numerical results from Bai et al. (2016). We notice that our numerical results largely correlate with the experimental data, except at $x/D = 1.06$, where the uncertainties in measurements are high. For the purpose of demonstrating this discrepancy, the numerical result obtained by Tremblay et al. (2000) using the DNS is also included in Figure 4.5 (b). We notice that the present numerical results are actually very close to the DNS prediction.

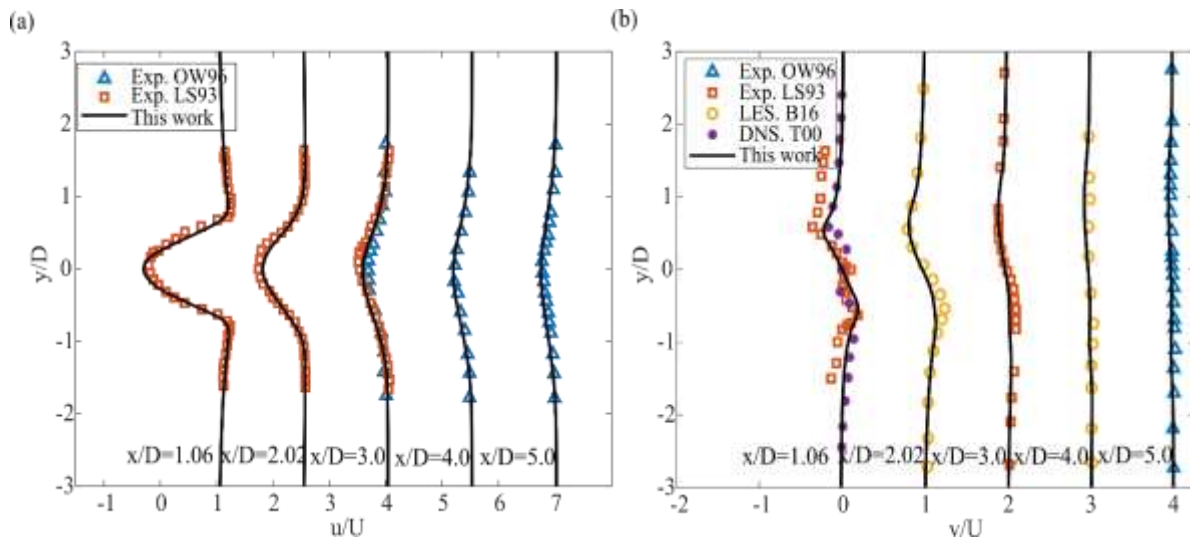


Figure 4.5: Mean velocity on a free slip bed at different streamwise positions (x/D) at $Re_D =$

3,900: (a) streamwise (u/U) and (b) spanwise (v/U) velocities.

4.1.2. Moderate Reynolds number case

Turbulent flows around a vertical cylinder are a complex phenomenon in computational fluid dynamics. The phenomenon of horseshoe vortex oscillation has been studied intensively by many researchers both experimentally and computationally and can serve as reference data for the current test case. LES was performed at a Reynolds number of 4,460 and 46,000 for a systematic study of the 3D horseshoe vortex and the wake behind the cylinder, with a much finer grid resolution in both horizontal and vertical directions.

A sketch of the computational geometry for the numerical simulations around a circular cylinder is shown in Figure 4.6. The origin of the coordinate system is located at the cylinder center on the bottom, with the x , y and z axis corresponding to the streamwise, spanwise and ascendant vertical direction, respectively. The computational domain is kept the same as 2D case, while in the vertical direction, to make the 3D phenomenon more obvious, the bottom boundary is set a no-slip wall and the top boundary is set as a free slip wall. Inflow velocity is given by a Poiseuille profile with the mean value as unit velocity.

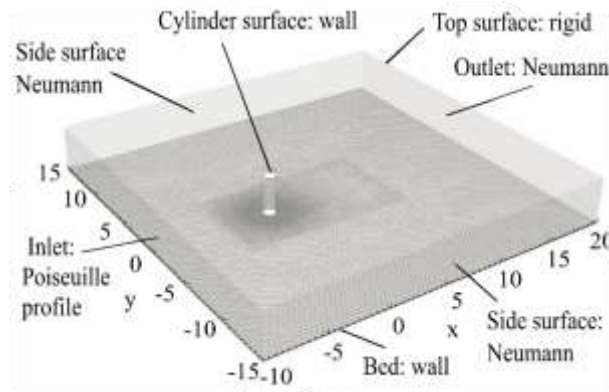


Figure 4.6: Sketch of the geometry of the computational domain and specification of the boundary conditions.

For $Re_D=4460$ case, the boundary layer thickness δ/D in the inflow is set to be $0.59D$. The element in the computational domain in X - Y direction is about 41202 with 424 points along the cylinder surface, the first row of cells is situated at $0.003D$ away from the cylinder surfaces, corresponding to 0.75 wall units. While for $Re_D = 46000$ case, the boundary layer thickness δ/D in the inflow is set to be $0.5D$, The computing domain is discretised into the order of three million finite volumes. 128 layers with finer resolution close to the bottom are employed to capture the oblique pattern of vortex shedding in the vertical direction. Horizontally, the first row of elements is situated at $0.003D$ away from the cylinder surfaces corresponding to 14 wall units.

The HV system is attributable to the separation of the incoming boundary layer induced by adverse pressure gradients, which are generated by the cylinder obstruction. The turbulence driven by the resulting flows will create a number of necklace-like structures around upstream the cylinder. Because of the lateral pressure gradients, these structures stretch when they fold around the cylinder (Kirkil et al., 2008). Their legs are approximately parallel to the direction of the incoming flow.

Figure 4.7a shows the main coherent structures in an instantaneous flow associated to a HV system on a rigid bed using Q criterion. We can see that the 2D parallel vortex shedding has transformed into a 3D mode, with dislocations present in both streamwise and vertical directions. The three non-dimensional vortices (DV1, PV1, CV1) and two counter-rotating bottom-attached vortices (BAV1 and BAV2) are clearly observed. As Kirkil & Constantinescu (2012), the figure illustrates the development of smaller-scale instabilities along the legs of BAV2. Figure 4.7b presents 3D streamlines, which clearly illustrate the HV system around the cylinder as shown in Figure 4.7a. It's observed that thanks to used fine-mesh resolution, numerical results can show rotational movements of HV around themselves.

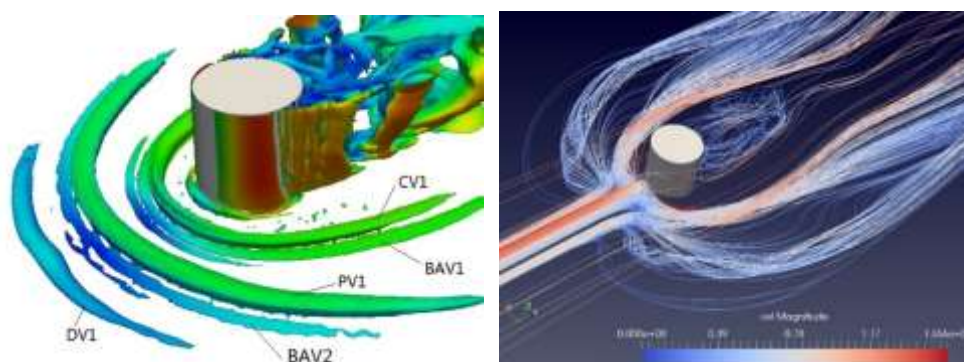


Figure 4.7: (a) Detailed view of the HV coherent structure; (b) and 3D streamlines.

Figure 4.8 shows the streamlines in front of the cylinder on a vertical plane (at the central axis, $y=0$) at 14 different instants during an oscillating cycle of the HV system, compared with experiment of Lin et al. (2003). We can remark that there are three primary clockwise vortices (PV) close to the bottom, forming a necklace vortex system. As reported by Kirkil and Constantinescu (2010), a typical horseshoe vortex system can consist of six individual vortices and its dynamics depend largely on the Reynolds number and on the characteristics of the incoming boundary layer. According to the smoke tunnel study by Baker (1979), it is also expected that counter-clockwise vortex should exist in the adjoining region between the cylinder and the bottom corresponding to each of the main vortex. We compare the structure

of the computed HV system with one observed in an experiment conducted at a Reynolds number of 2250 by Lin et al. (2003), the HV system was in the breakaway sub-regime. A nearly perfect agreement on HV system pattern has been obtained. The three main vortex are correspondingly: 1) the developing vortex (DV1) located at the upstream-most position of the flow domain, 2) the primary vortex (PV1) at the middle, and 3) the corner vortex (CV1) at the right. The overall process, illustrated in Figure 4.8, is that: DV1 is first formed at the upstream position among these three vortices, and DV1 originates from the position where the separated boundary layer starts to evolve, and moves downstream to become a new primary vortex (PV2). Subsequently, as the PV1 moves closer to the juncture of the vertical cylinder, it then becomes a new corner vortex (CV2). The similar expression of HV system is due to the similar relative thickness of the incoming boundary layer and similar Reynolds number.

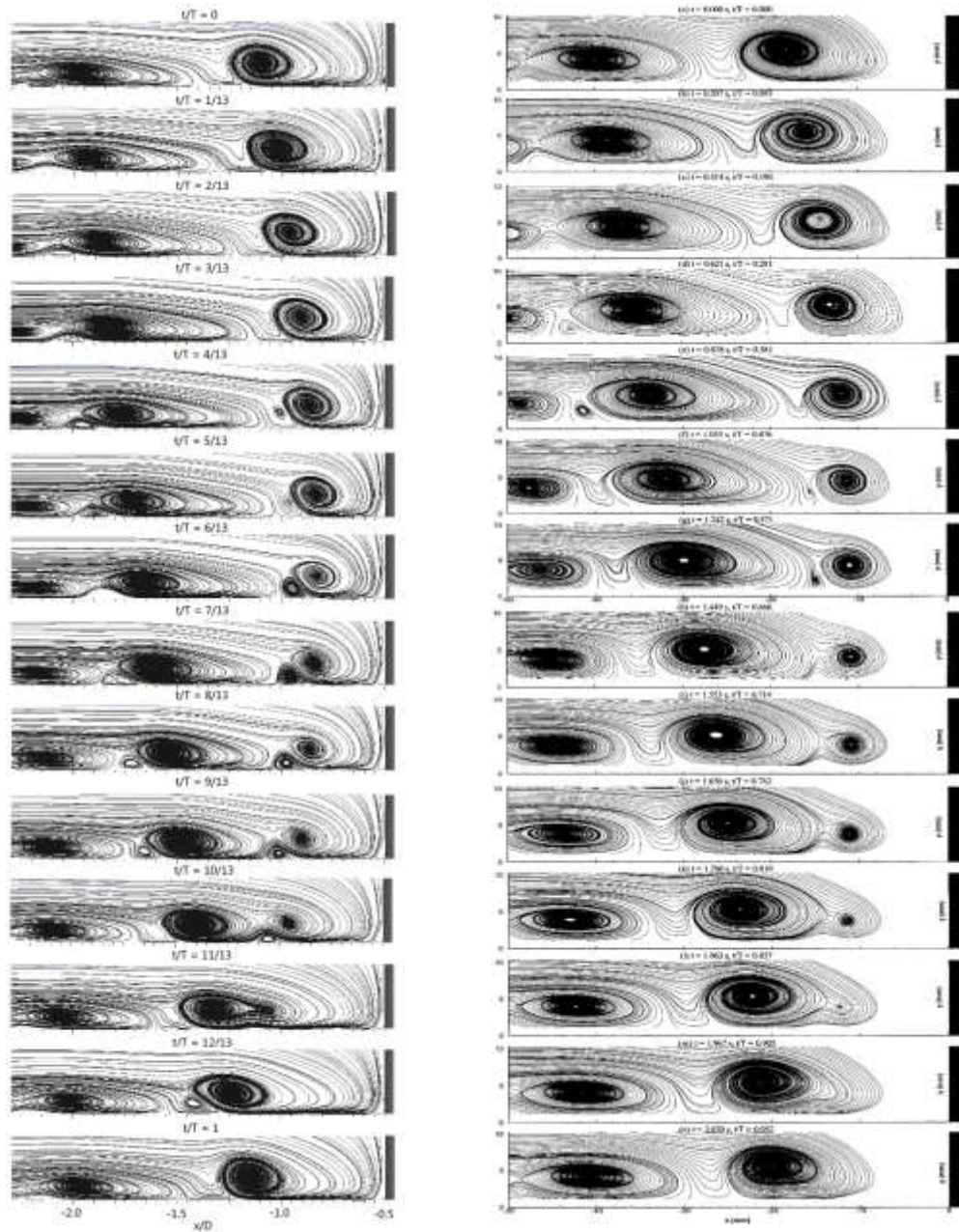


Figure 4.8: Streamline patterns in the upstream comparing the LES numerical results with experiment of Lin et al. (2003) at a time interval of $0.0769T$, where T is the period of the breakaway cycle.

4.1.3. High Reynolds number case

Figure 4.9 shows the main coherent structures in an instantaneous flow associated to a HV system on a rigid bed using $h=4D$ and $Re_D=46,000$. Clearly there exists two primary necklace vortices and two bottom-attached vortices. A U-shaped Primary Vortex (PV1) wraps around the upstream part of the cylinder, along which a small, but very coherent,

junction vortex appears at the base of the cylinder (JV). Another U-shaped Primary Vortex (PV2) is observed upstream of PV1. The formation of Bottom-Attached Vortices, BAV1 and BAV2, are induced upstream by the presence of the primary vortices PV1 and PV2. Secondary Vortices (SV) are observed towards PV2.

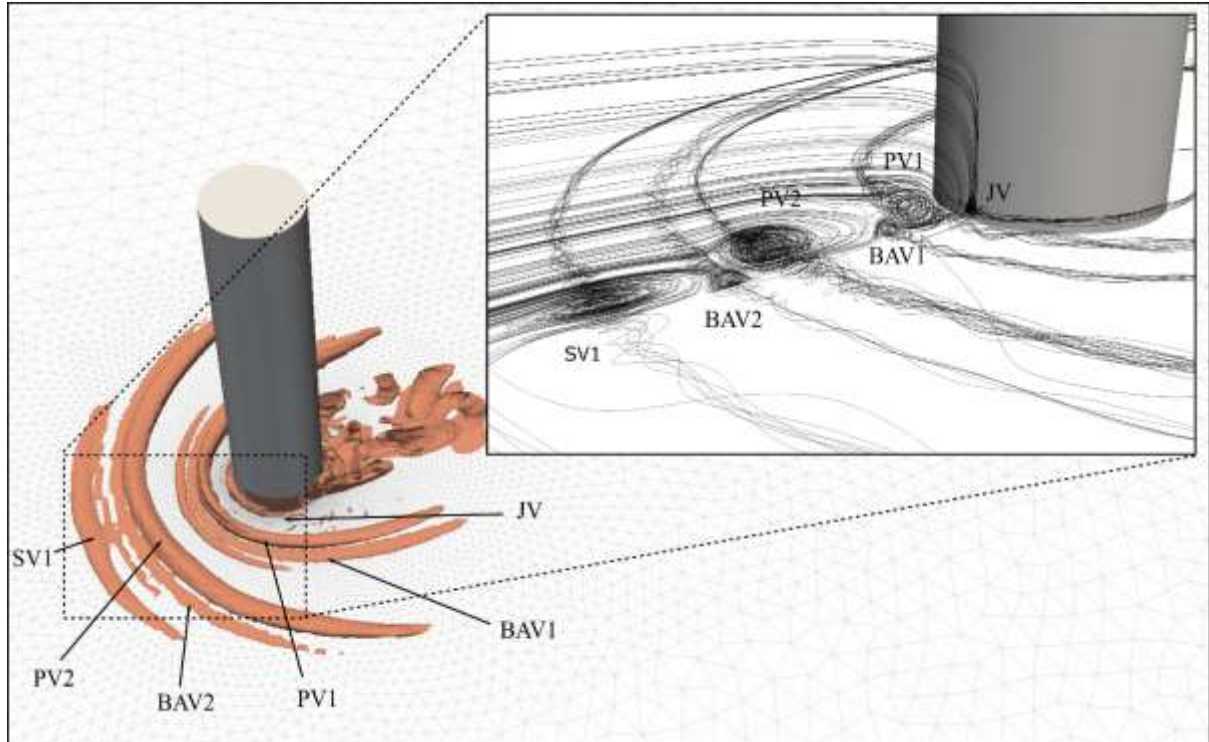


Figure 4.9: Detailed view of the coherent structure with a HV system on a rigid bed.

The location, size, and intensity of the turbulent HV highly vary in time. Figure 4.10 shows four instances of a cycle of oscillation. The main vortex cores show in different positions. Clockwise-rotating primary vortices (PV1, PV2) and counter-rotating bottom-attached vortices (BAV1, BAV2) appear at all times during the oscillation cycle, exhibiting a relatively stable behaviour. Smaller secondary vortices (SV) are shed randomly from the separation region of the incoming boundary layer. These SV are convected toward PV2 and can interact and merge with it. The direction of the oscillate centers of PV1 and PV2 are found to be oppositely positioned to one another: at $t=T/2$ they move closer, and at $t=T/4$ and $t=3T/4$ move far away from each other. The amplitude of oscillation in the direction of flow is about $0.1D$. We remark that the structure of HV system, observed by our model using $h=4D$ and $Re_D=46,000$, is similar to the ones of Kirkil et al. (2008) using $h=1.12D$ and $Re_D=16,000$.

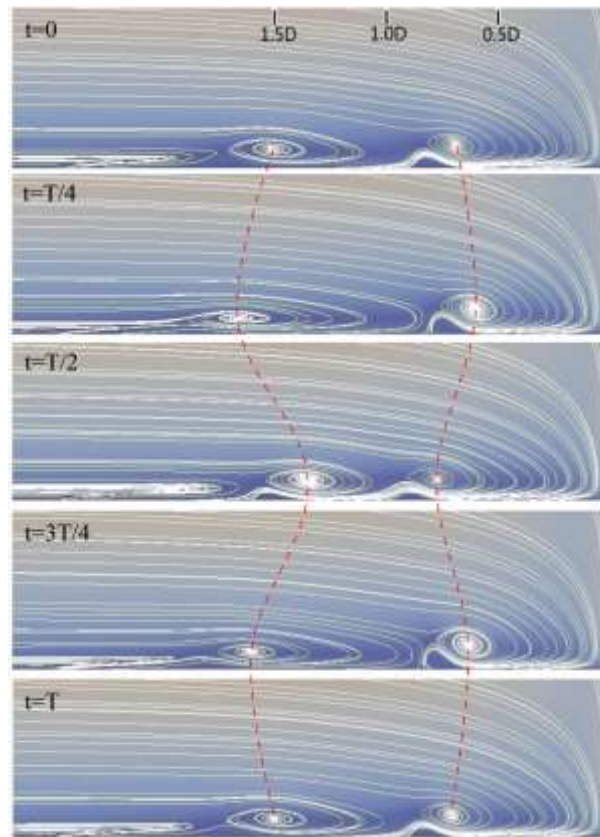


Figure 4.10: Instantaneous streamlines on the longitudinal section upstream the cylinder at five instants in time for the rigid bed case.

Figure 4.11 shows mean streamlines on a longitudinal plane located behind the cylinder in the wake. S , F and N denote the saddle points, the centers of foci and nodal points, respectively. The arrows represent the direction of the flow. It is noticed that there exists a nodal point of attachment N_l , corresponding to the merging point of shear layers emanating from both sides of the vertical cylinder to form a spanwise-oriented vortex. As a consequence, fluid particles situated close to the bed are first entrained into the core of this vortex, and then from there toward the surface by an upwelling anti-clockwise vortex, shown by a foci point F_l . This counter-clockwise rotating vortex is responsible for the scour mechanisms downstream of the cylinder.

Figure 4.12 shows mean flow streamlines on different spanwise cross-sections located at four different stations: $x/D=0.5$, 1.0 , 1.5 and 2.0 . The streamline patterns are almost symmetric, except for the lee wake just behind the cylinder. There is a pair of vortices near the bed corresponding to the primary vortex legs. We notice that even at $x=2D$, these legs are still maintained. The shear layers, emanating from the side edges of the cylinder, roll up to form vortices in the lee wake of the cylinder. These vortices engender upwelling motion of

fluid particles toward the surface. The upwelling motions inside the wake region are compensated by down-welling motions on the outside.

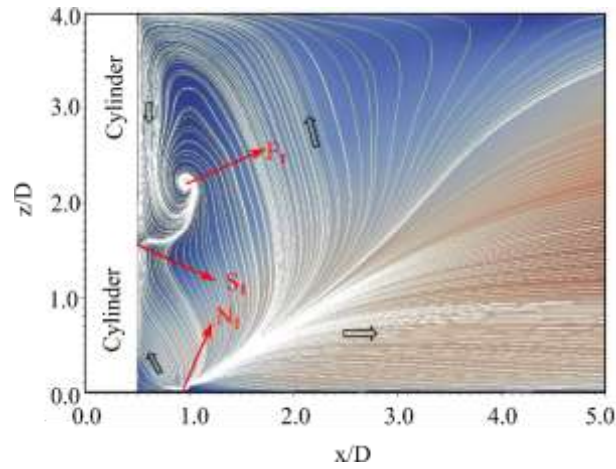


Figure 4.11: Mean flow streamlines on the longitudinal section behind the cylinder for the rigid bed case. The direction of the flow is indicated by the arrows.

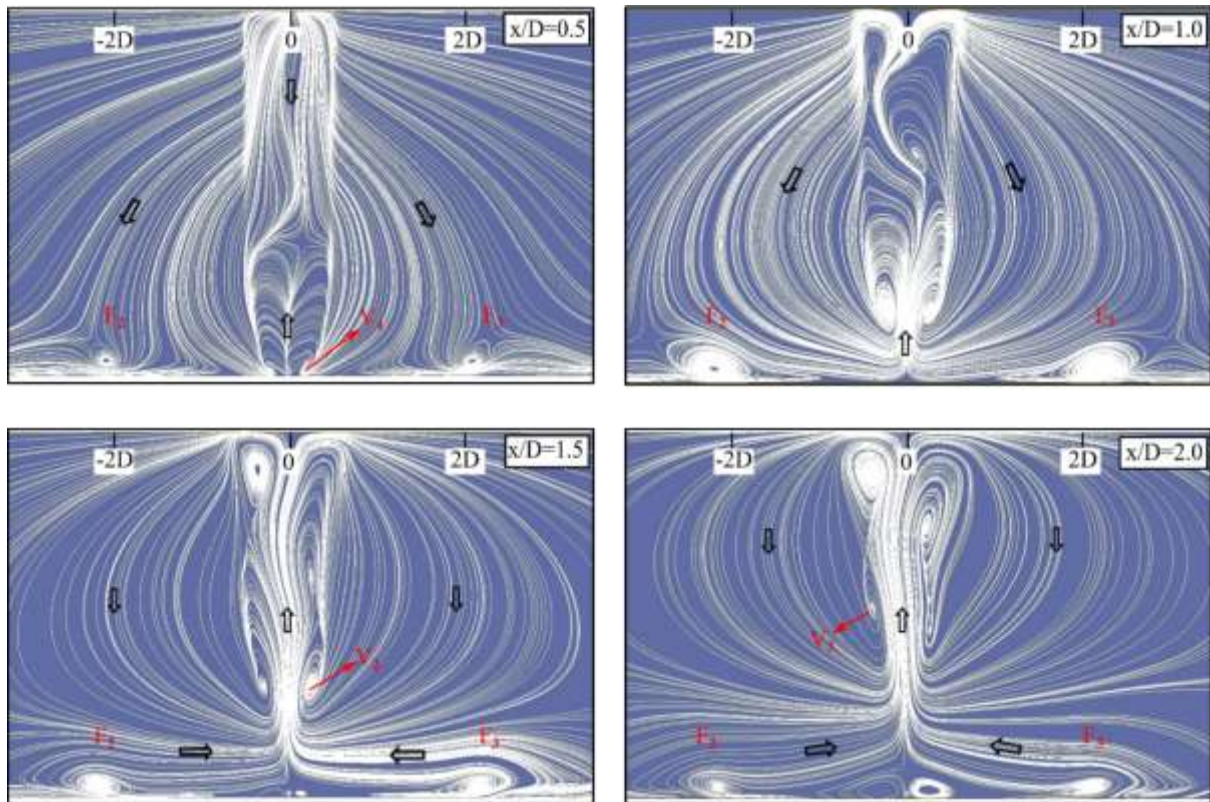


Figure 4.12: Mean flow streamlines on the vertical cross-sections behind the cylinder for the rigid bed case.

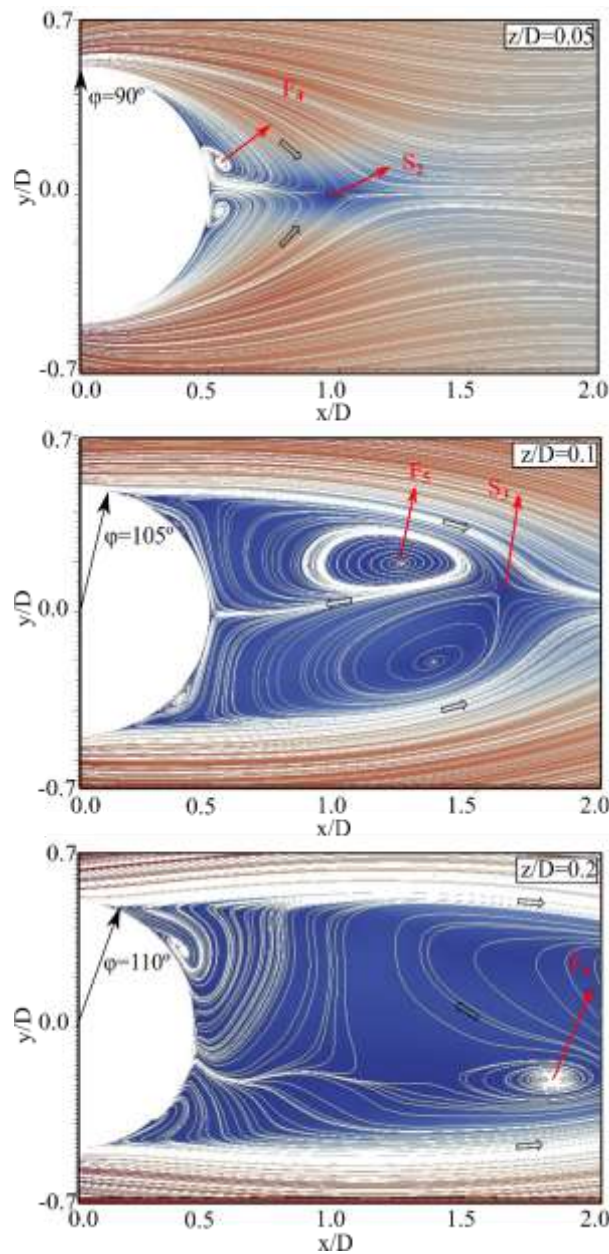


Figure 4.13: Mean streamlines on different horizontal planes for the rigid bed case.

Figure 4.13 presents mean flow streamlines on horizontal planes at $z/D = 0.05, 1.0$, and 2.0 in the wake region. The flow separation points are located at $\varphi = 90^\circ, 105^\circ$ and 110° at $z/D = 0.05, 1.0$ and 2.0 , respectively. It's noticed that these separation points move downstream as z/D increases. This observation is also recorded by Kirkil & Constantinescu (2015). Moreover, Figure 4.13 shows that the wake region becomes bigger as it rises to the surface. Saddle points, S_2 and S_3 indicate the end of the wake region at planes $z/D = 0.05$ and 1.0 and the corresponding detachment lengths are $0.9D$ and $1.9D$, respectively. Foci points F_4 ($x=0.55, y=0.13$), F_5 ($x=1.24, y=0.2$) and F_6 ($x=2.05, y=-0.22$) show the position of upwelling vortexes V_1, V_2 and V_3 .

Figure 4.14 gives the bed shear-stress iso-values, obtained from the mean flow simulation and compared with the results of Roulund et al. (2005). The model reproduces most of the characteristics observed by Roulund et al. (2005) in the vicinity of the cylinder but with very slight discrepancies far away from it. The average distribution of the shear stress is fairly axisymmetric. High values are found for shear stress on the two sides close to the cylinder, approximately corresponding to the position where the velocity is highest, just before the flow separation line.

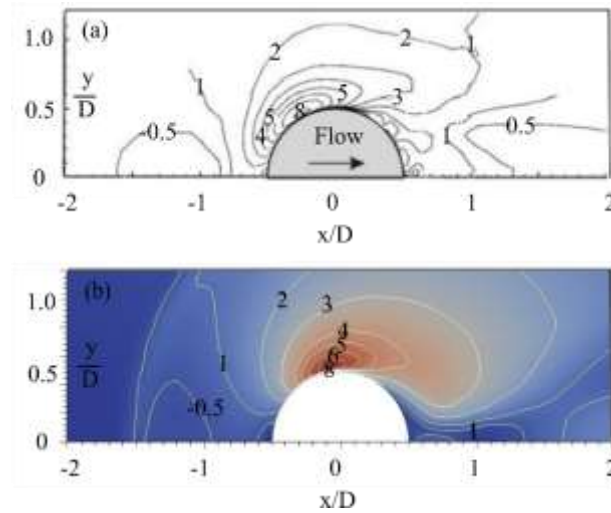


Figure 4.14: Non-dimensional bed shear stress distribution at $Re_D=46,000$.

(a) Results from Roulund et al. (2005) and (b) Current numerical simulation.

4.2. Flow around a cylinder on flat bed with free surface

4.2.1. Low Froude number case

Roulund et al. (2005) established that there is no significant Froude (Fr) number effect on the flow in the radial direction when relatively small values Fr are used. It was based on their numerical simulations of rigid bed flows ($Fr=0.14$). The comparison between their results with the experimental results of (Hjorth, 1975) ($Fr=0.21$) and of Dargahi (1989) ($Fr=0.19$). Dargahi (1989) shows that in these cases, Froude number effect was practically non-existent. Roulund et al. (2005) also indicates that the difference Δh in the surface elevation between the front and side edges of the cylinder may be written, for small Fr , as

$$\Delta h / h = Fr^2 / 2, \quad (4.1)$$

where h is the total depth. Using this relationship, it can be seen that the relative difference is so small when $Fr < O(0.2)$, making no significant impact in the simulations. However, this formula was not even numerically demonstrated because Roulund et al. (2005)'s model cannot handle free-surface flows. Using NSMP3D for this case, we impose no-slip conditions on the bottom to only focus on free-surface level evolution. The same discretization as in the 3D cylinder case is used for the numerical simulations.

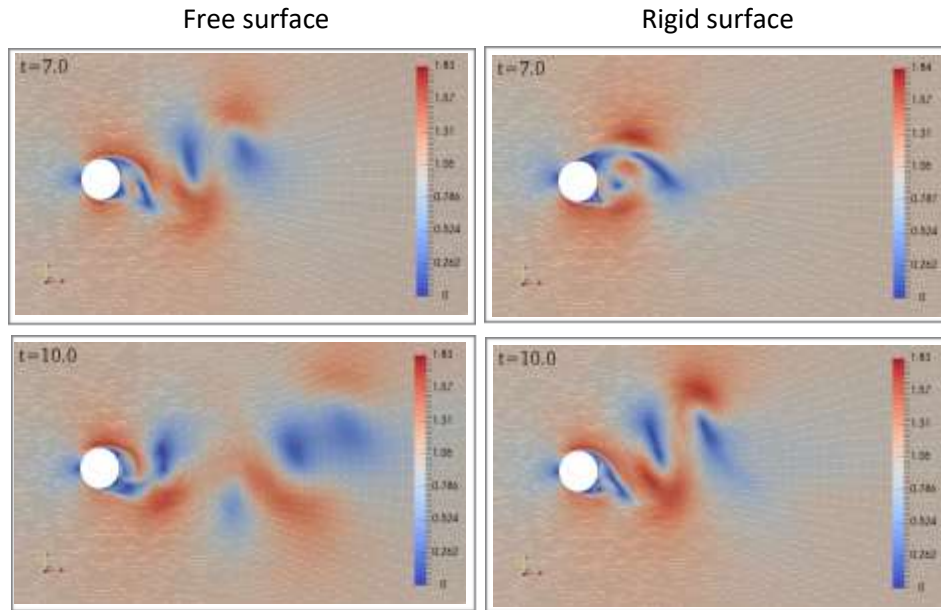


Figure 4.15: Velocity magnitude and streamlines for unsteady flow simulation using a free surface (left) and a rigid surface (right) for $Fr=0.075$, $Re_D=3032$ and $h/D=1.0$.

Figure 4.15 depicts the predicted horizontal velocity-magnitude field and streamlines around the cylinder, obtained from NSMP3D at the level $z/D = 0.5$ and different times, where z is the water depth level. The Froude number, the Reynolds number and relative water depth in these simulations are $Fr = 0.075$, $Re_D = 3032$ and $h/D = 1.0$, respectively. There are vortex shedding in the both cases. However, this phenomenon occurs with a lag time between the free-surface case and the rigid surface one. We notice the vortex shedding in the free-surface case evolves faster than the rigid-surface case, making that the individual vortices are perceptible at early times in the first case. Notice that the simulation at $t = 7$ in the free surface case is nearly similar to the one at $t = 10$ in the case of rigid surface. This can be explained by the fact that the free surface imposes less constraints on velocity fields than the rigid surface.

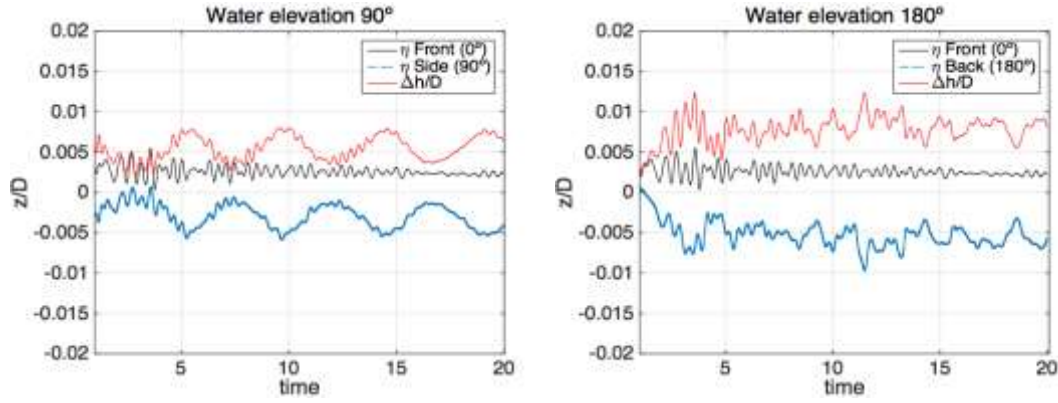


Figure 4.16: Numerical simulation of the water surface elevation between front and side (0 to 90°) and between front and back (0 to 180°) as a function of the time using $Fr = 0.075$, $Re_D = 3032$ and $h/D = 1.0$.

Figure 4.16 presents the variation in water surface elevation from the front to the side (0 to 90°), and from the front to the back (0 to 180°) of the cylinder, respectively, in function of time using the same flow parameters as above mentioned. Differential water surface elevation results have been normalized by the cylinder diameter. NSMP3D results show that the average water elevation difference at the side is about $\Delta h/h = 5.6\text{e-}03$ meanwhile Eq. (4.1) gives a value of $2.81\text{e-}03$. Obviously, the numerical value corresponds to the one predicted by NSMP3D. We also notice that more turbulent behaviour is observed at the back of the cylinder than at the side, as expected.

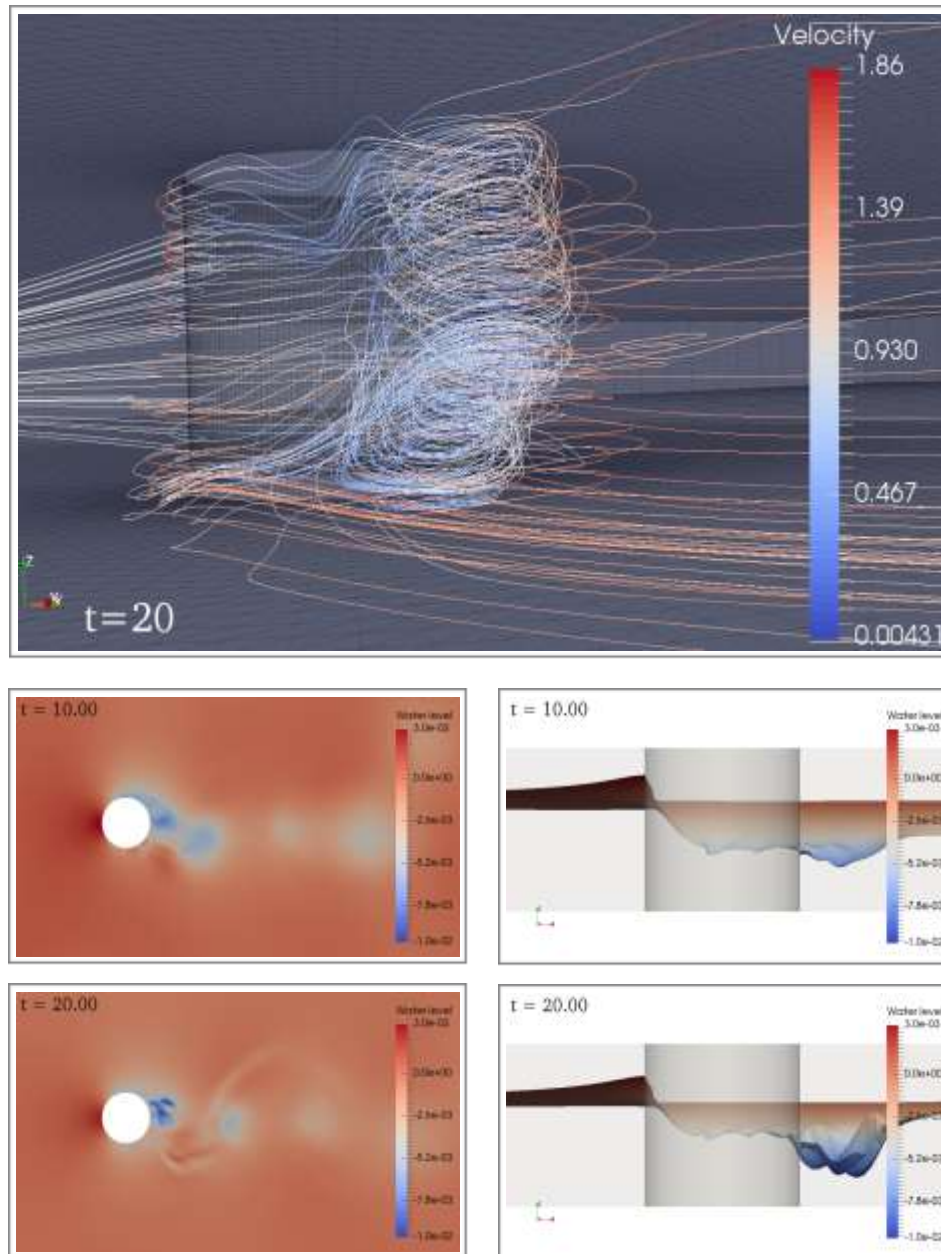


Figure 4.17: Velocity streamlines at the back of the cylinder and water surface elevation in the horizontal and vertical direction (amplified 50 times) at different times using $Fr = 0.075$, $Re_D = 3032$ and $h/D = 1.0$.

Figure 4.17 shows three-dimensional streamline plots at the back of the cylinder. Even though the water surface elevation is very small and the rigid lid approximation seems to be acceptable, we notice the influence of water surface elevation on the component of flow velocity in the radial direction, especially close to the free surface. In horizontal and vertical view, numerically predicted water elevations around the cylinder are also shown in Figure 4.17. The water surface elevation was highest in front of the cylinder, and lowest behind it, in

agreement with the experimental results. The water elevation has been amplified 50x to make visible this profile. Similar results are obtained for other small values of the Froude number.

4.2.2. High Froude number case

For large Froude numbers, the differential water surface elevation $\Delta h/h$ is expected to be a function of not only Fr but also h/D , as presented by Johnson and Ting (2003) in their experimental results. In this paper, we follow similar test cases as Johnson and Ting (2003) and shown in the Table 4.2.

Table 4.2 Numerical conditions and surface elevation for the test cases with large Froude numbers and high Reynolds number

Fr	Re_D	h/D	dh/D (90°)	dh/D (180°)
0.18	7.60E+03	1.04	0.032	0.047
0.20	7.90E+03	0.97	0.039	0.043
0.27	1.15E+04	1.03	0.085	0.079
0.29	1.67E+04	2.02	0.108	0.083
0.34	1.41E+04	1.03	0.137	0.123
0.36	1.50E+04	1.03	0.146	0.119
0.43	2.52E+04	2.06	0.251	0.135
0.44	1.85E+04	1.06	0.216	0.199
0.57	2.33E+04	1.00	0.325	0.250

Comparisons of the free surface elevations obtained from the experimental study and numerical predictions by NSMP3D, are given in Figure 4.18. It presents the variation in water surface elevation from the front to the side (0 to 90°), and from the front to the back (0 to 180°) of the cylinder, respectively, as a function of Fr and h/D . As seen from Figure 4.18, the tendency of the relationship between Froude number and water relative elevation shows good agreement between the numerical and experimental results. The results show that the value of dh/D increases when the Froude number increases. However, NSMP3D cannot handle with $Fr > O(0.6)$ and $Re > 25\,000$ due to high Reynolds number values. In these cases, the diffusion term is almost zero resulting in a strongly degenerate parabolic problem. Future research is focus on the implement new numerical techniques to solve this issue.

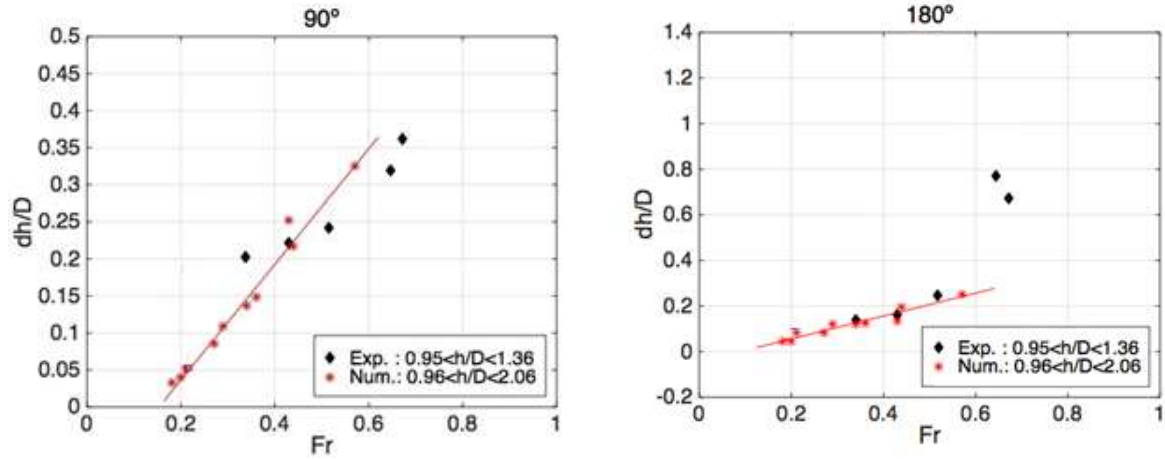


Figure 4.18: Comparison of the relative variation of different water surface elevation between the numerical model and the experimental results with large Froude numbers.

We present the NSMP3D results for $Fr = 0.44$, $Re_D = 18,500$ and $h/D = 1.06$ as an example for large Froude number values. Figure 4.19 shows dh/D from the front to the side (0 to 90°), and from the front to the back (0 to 180°) of the cylinder, respectively, as a function of time. The average water elevation difference at the side and back are $dh/D = 0.21$ and $dh/D = 0.19$, respectively. Although, the value at 180° has more oscillations, both values remain stable since $t = 5$.

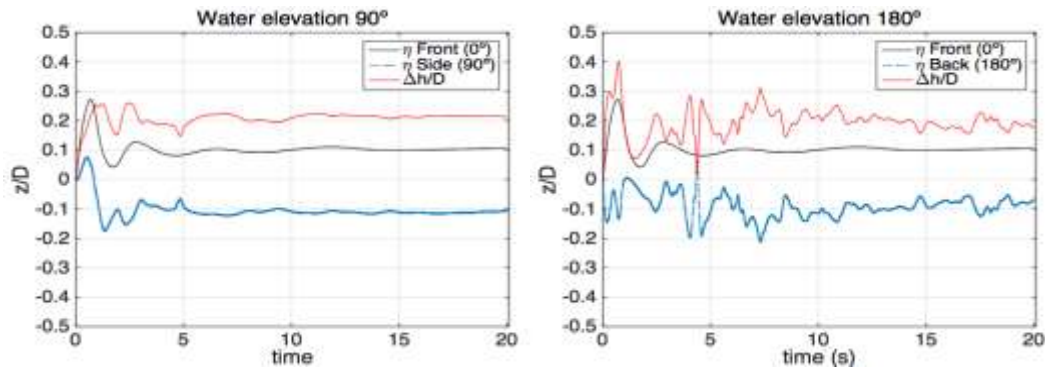


Figure 4.19: Numerical simulation of the water surface elevation between front and side (0 to 90°) and between front and back (0 to 180°) as a function of the time using $Fr=0.44$, $Re_D=18,500$ and $h/D=1.06$.

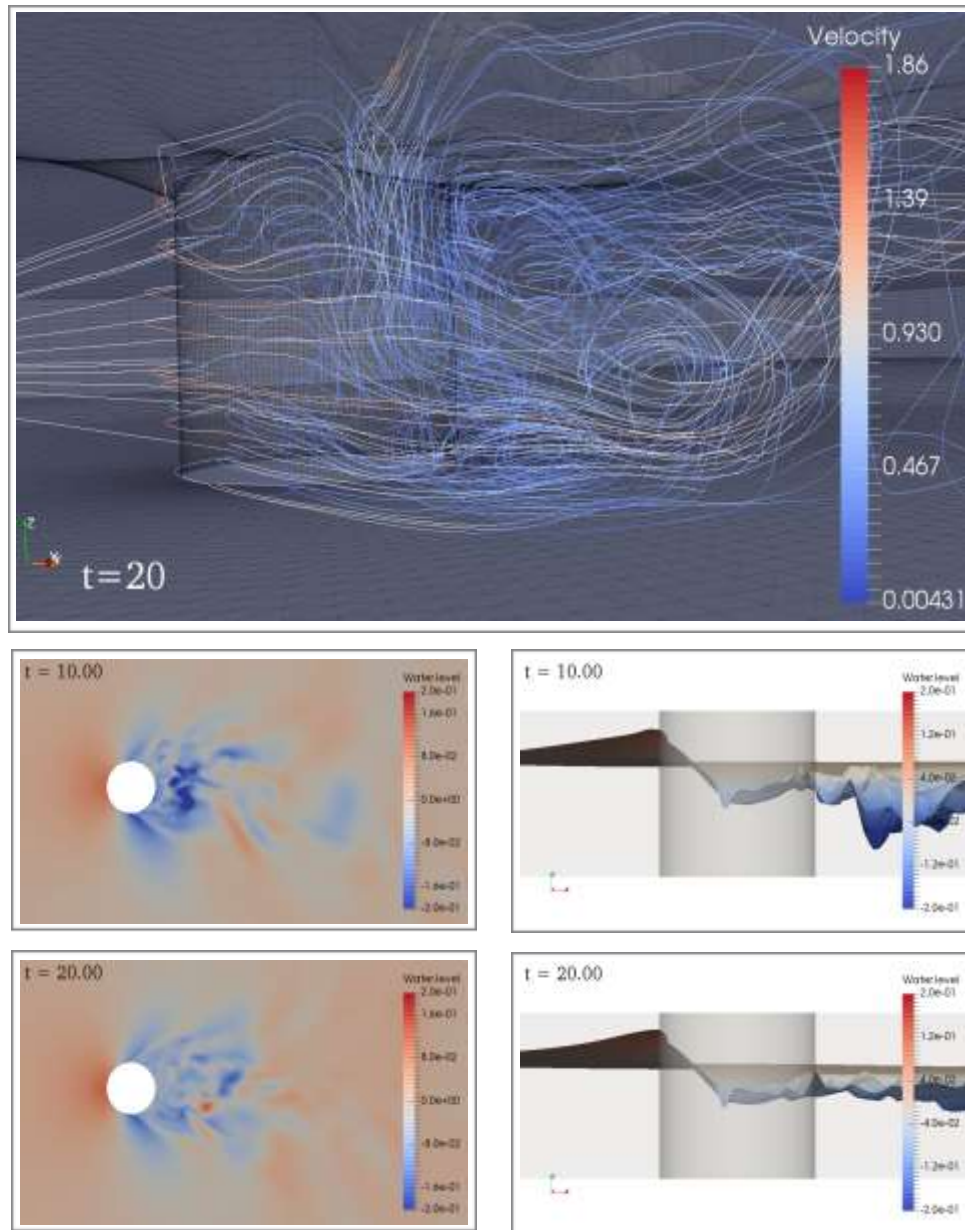


Figure 4.20: Velocity streamlines at the back of the cylinder and water surface elevation in the horizontal and vertical direction (amplified 5 times) at different times using $Fr=0.44$, $Re_D=18,500$ and $h/D=1.06$.

Figure 4.20 presents the three-dimensional streamlines plots and the water surface elevation at the horizontal and vertical direction. Clearly three-dimensional streamlines represent deviation-deflexion to form horseshoe vortex near the bottom and ascending flows combined with wake in the area behind the cylinder. The relative difference between the surface elevation in front and at the side edge of the cylinder is now almost 20% of the total water depth. This difference and therefore the induced-pressure gradient generates a strong down flow with a very strong component of flow velocity in the radial direction, as observed in the streamlines in Figure 4.20. NSMP3D results show that the water surface elevation was

also highest in front of the cylinder and lowest behind or side it, as expected. In Figure 4.20, the water elevation has been amplified 2x to observe the vertical profile (compare with the 50x used in the previous case).

4.3. Flow around a cylinder with scour erosion

The boundary conditions for the flow field are defined as follows: at the inlet, transverse and vertical velocities are specified as zero. The inflow velocity is given by a Poiseuille profile with a unit mean non-dimensional value and boundary layer thickness $\delta/D=0.5$. At the outlet, zero-gradient conditions were applied for all variables. The boundary in the spanwise direction is set as Neumann conditions. As it was pointed out in the previous section, a rigid surface is used on the top. Finally, no-slip wall boundary conditions are applied for the cylinder surface and the bottom bed. A detailed view of the deformed mesh close to the cylinder is shown in Figure 4.21.

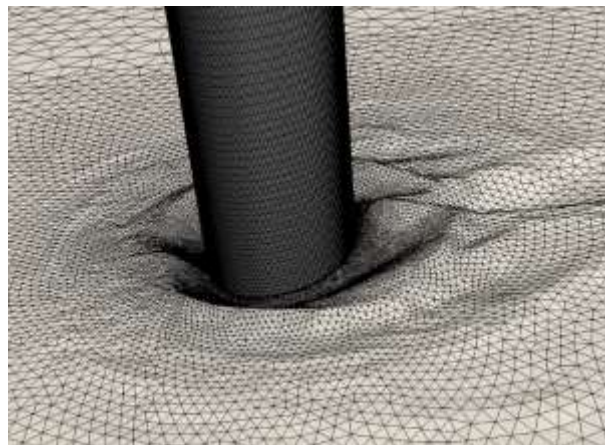


Figure 4.21: Detailed view of the deformed mesh close to the cylinder with scouring.

In this paper, a numerical study similar to Roulund et al. (2005) is adopted. The diameter of the cylinder is $D = 0.1m$. The water depth is set to be $h = 4D$. The undisturbed mean flow velocity is $U = 0.46m.s^{-1}$. The sand size is $d = 0.26mm$. The equivalent roughness height for the rough wall function is set to be $k_s=2.5d$, which determines the skin friction velocity in turn. A live bed scour with $Re_D = 46,000$ is applied to test the morphological model. The initial condition for live bed scour is from the final results of rigid bed simulation. The conditions in the last two cases are summarized in Table 4.3.

Table 4.3 Test conditions for scour around a cylinder

Bed	Loose sand
Water depth, h	0.4 m
Cylinder diameter, D	0.1 m
Boundary layer thickness, δ	0.2 m
Mean flow velocity, U	0.46 m/s
Reynolds number, Re_D	46,000
Froude number, F_r	0.23
Sediment density, ρ_s	2,600 kg/m ³
Fluid density, ρ	1,000 kg/m ³
Grain size, d	0.26 mm
Sand roughness due to skin friction, k_s	0.65 mm

4.3.1. Horseshoe vortex system

Figure 4.22 shows the main necklace vortices inside the scour hole by using the Q criterion. Similar to the rigid bed case, U-shape necklace vortices also appear in the live bed case. They contain two Primary Vortices (PV1 and PV2), a Bottom-Attached Vortex (BAV) and a Joint Vortex (JV) (Dey & Raikar, 2007). The HV system is in a close relationship with the scour process. According to Baker (1979) and Kirkil et al. (2008), the number of these necklace vortices and their extent in the polar direction may change with the Reynolds number. Necklace-like structures detach from the incoming bottom boundary layer over a certain range of polar angles and then interact with other secondary vortices or with the primary one. Some of these vortices merge with the main or another secondary necklace vortex; others will lose their coherence rapidly. Consequently, the intensity of the overall HV system varies substantially across time. In many cases, the interaction with another necklace structure takes place only over a limited area of the total length of two vortices.

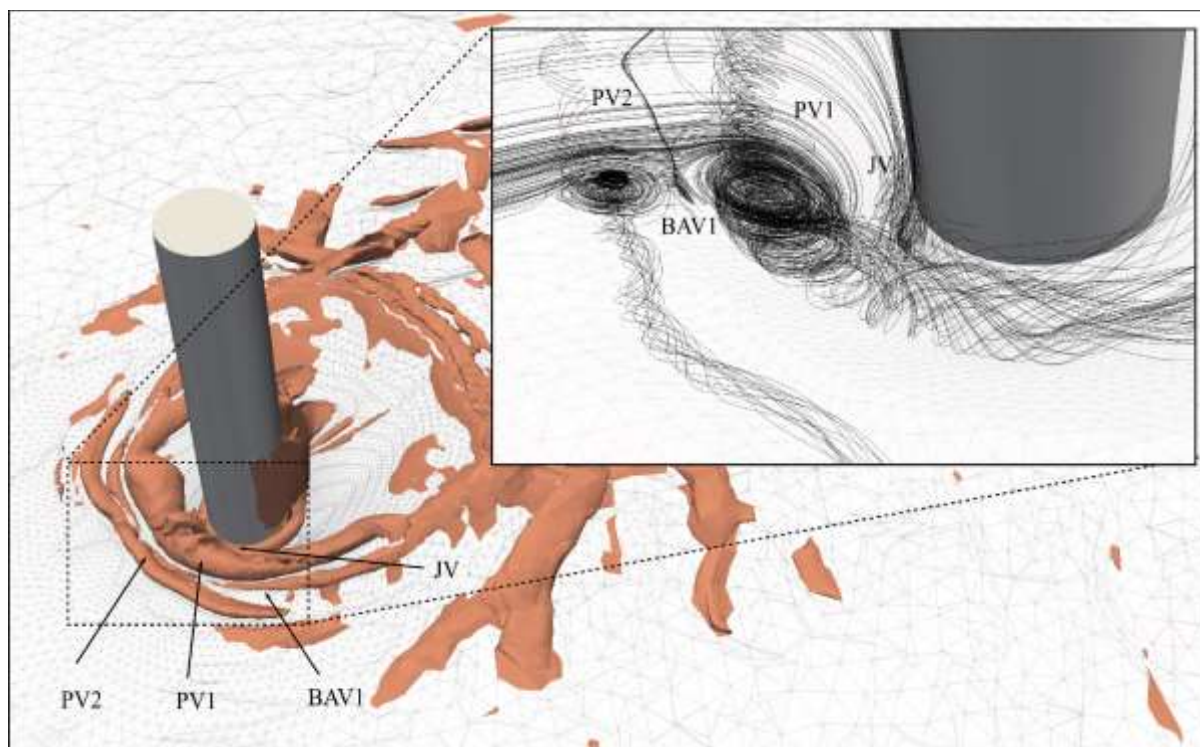


Figure 4.22: Visualization of the main necklace vortices inside the scour hole for the live bed case.

Figure 4.23 provides more details on the temporal evolution of the streamlines in the scour hole upstream the cylinder. The present model successfully simulates the dynamics of the initial stages of erosion by the unsteady coherent structures of the HV system. As the scour hole gets deeper and extends, the HV system grows in size but decreases in strength until reaching the conditions for equilibrium. Such a state of equilibrium is reached when the shear stresses are reduced down to a local threshold value for the sediment-particle entrainment. Once the scour hole has formed, the HV system becomes more stable. During the scour process, PV1 still oscillates around at $x = 0.5D$ upstream the cylinder, as with the rigid bed case, and slips down into the middle of the hole to adapt to a new position in the bed. PV2 grows bigger and increases in coherence. With the development of PV1 and PV2, a BAV is generated and grows between them. The vortices corresponding to JV grows bigger as the scour domain develops close to the cylinder.

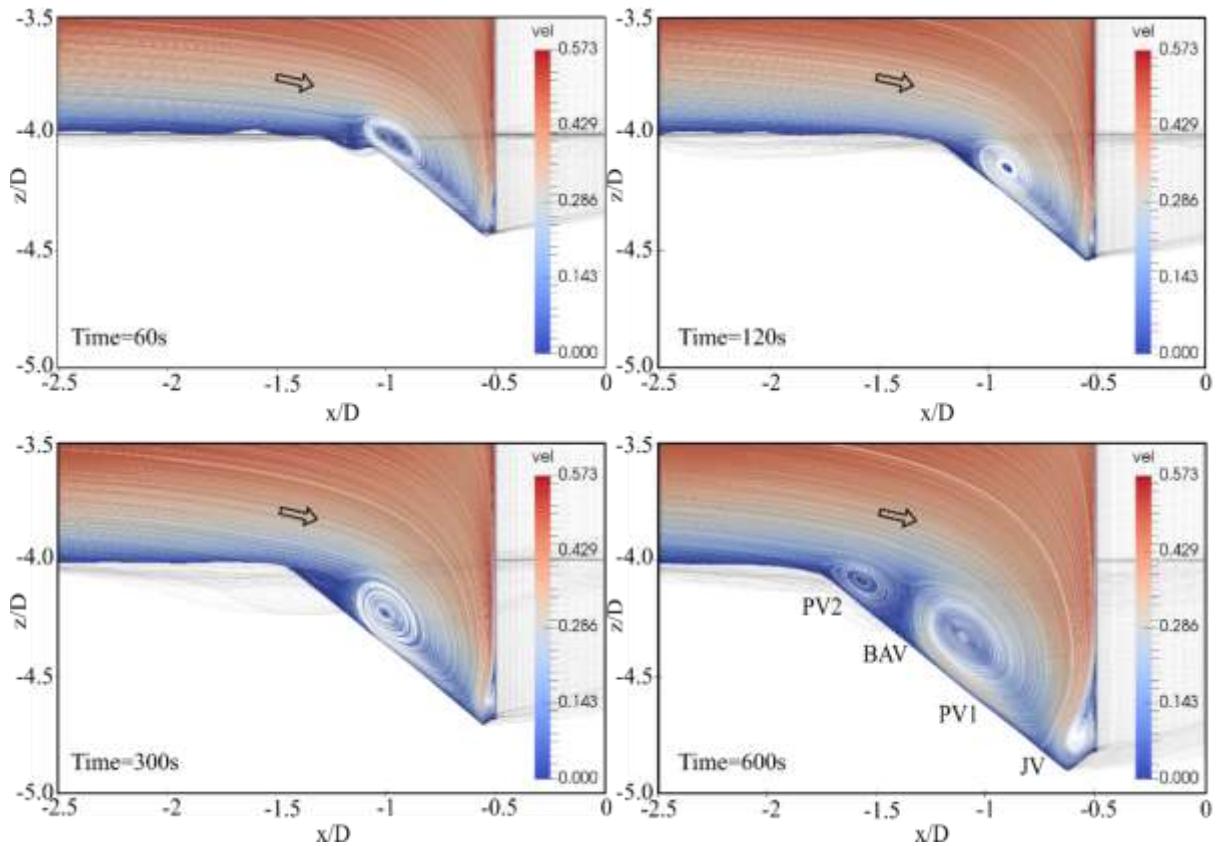


Figure 4.23: Horseshoe vortex system in the scour hole development around the cylinder in front of the cylinder.

4.3.2. Near wake flow

Figure 4.24 shows time-mean streamlines for the live bed case on a longitudinal plane behind the cylinder in the wake region. A large recirculation zone is generated due to the changes in bed topography as we move downstream. As with the rigid bed cases, there exists a nodal point N_2 of attachment positioned at $(x/D = 0.875, z/D = -0.1785)$. The negative sign indicates that this level is below the initial bed level. N_2 corresponds to the merging point of the streamlines issued from the convergence of both lateral sides of the cylinder. Thus, sediment particles situated close to the bed are entrained by the flow: first in the spanwise direction and later toward the surface by an upwelling anti-clockwise vortex, indicated by foci F_7 . The presence of foci and nodal points in the wake region has already observed in experimentation using $h = 6D$ and $Re_D = 7000$ (Sahin & Ozturk, 2009).

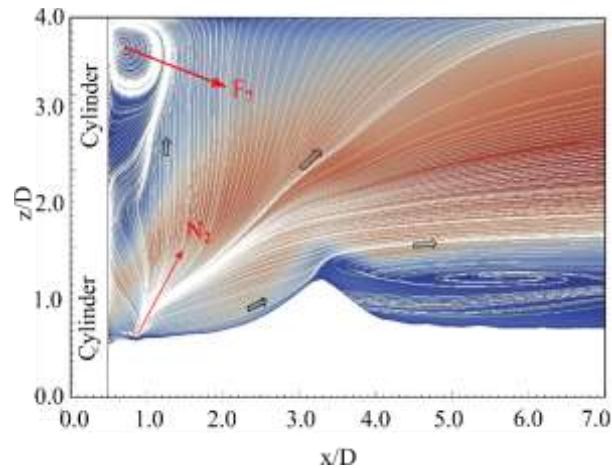


Figure 4.24: 3D streamlines of the mean flow for the live bed case.

Figure 4.25 presents a 3D view of time-averaged streamlines around the cylinder. Clearly, a down flow can be observed at the upstream side of the cylinder which generates a primary vortex, as discussed in the preceding paragraphs. The flow structure in the wake region are also showed in this figure. Streamlines wrap the cylinder from both lateral sides. Then, flow in spanwise converges at nodal point N_2 . From N_2 , due to an upwelling vortex (F_7), an important patch of fluids rises up into the surface layers, entraining sediment particles situated on the bed, and bringing them out the wake. This phenomenon induces the scour process behind the cylinder.

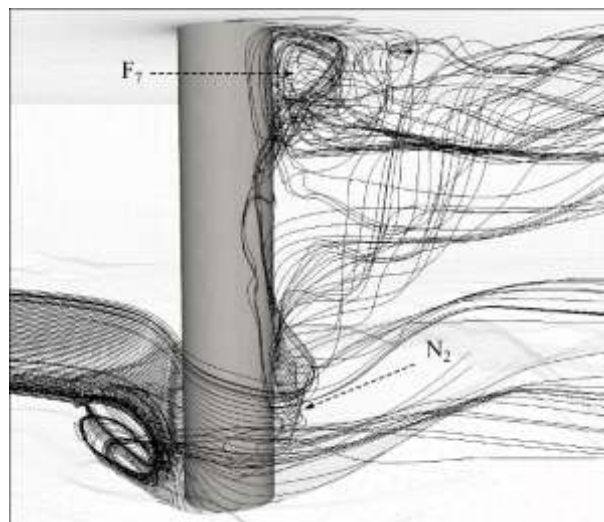


Figure 4.25: 3D streamlines of the mean flow for the live bed case.

4.3.3. General erosion patterns and maximum erosion depth prediction

Figure 4.26 illustrates the evolution of the scour hole across time as obtained by the present study at four instances: 30s, 120s, 300s and 750s. The pattern exhibited by the scour hole closely resembles the results observed in Roulund et al. (2005). The deepest part of the main scour hole occupies upstream and spanwise sides of the cylinder. A maximum angle for the bed slope is fixed inside this region, equal to the prescribed angle of repose: 32° . Exact localization of the maximum angle corresponds to regions where sand-slide algorithm functions and where the avalanching process is produced by the model. Additionally, sands are deposited in the downstream part of the cylinder. Some small bed changes are observed far from the main scour hole. The evolution of sand deposition downstream the cylinder is almost symmetric with the presence of sandpits. These sandpits tend to decrease with time without being fully erased at $t = 750s$.

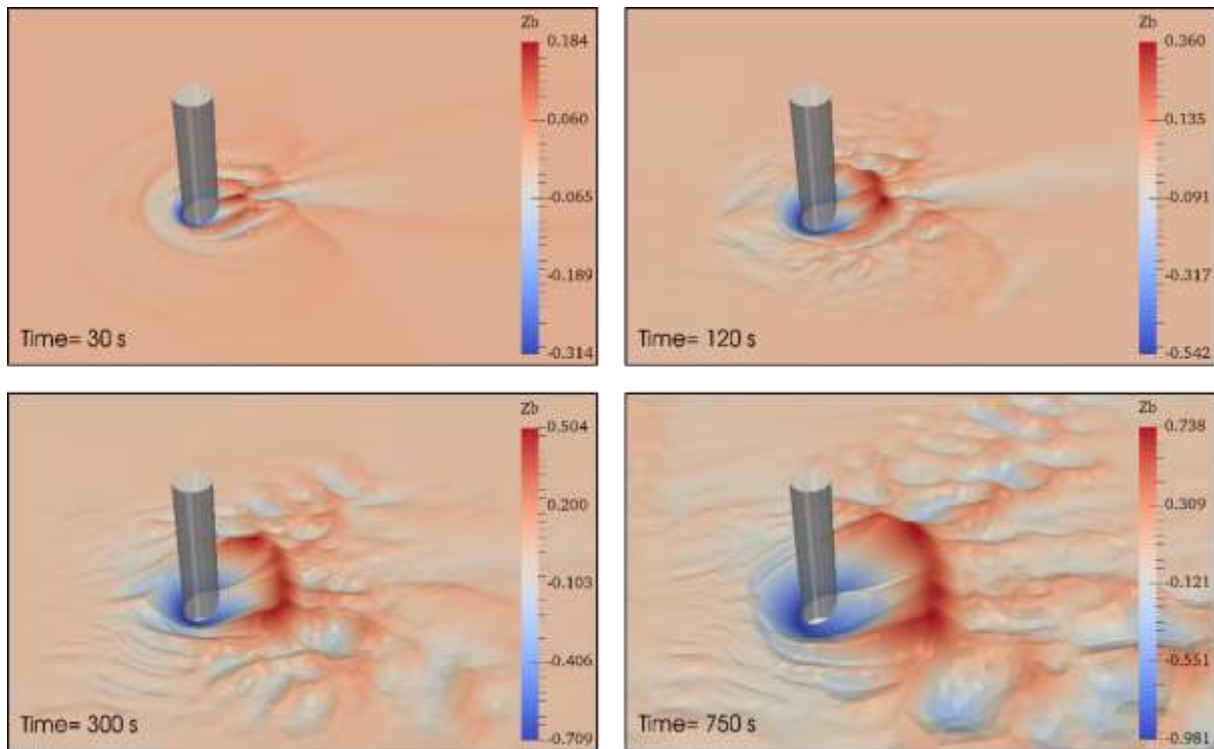


Figure 4.26: Scour development simulation results at time $t = 30s$, $t = 120s$, $t = 300s$ and $t = 750s$.

Figure 4.27 shows the time evolution of the scour depth at the upstream and downstream side of the cylinder compared with Roulund et al. (2005). At the beginning of the scour, both numerical models slightly over-predict the depth at the upstream side while under-predict the depth at the downstream side, compared to experimental data. Roulund et al. (2005) explained the reasons of the downstream discrepancy between simulation and experiment. One is that the suspended load process is not covered in the model, therefore the model scour

depth remains rather small during this stage. Another is that the vortex shedding in the lee wake of the cylinder is ignored, which will decrease the predicted scour depth downstream of the pile (Sumer et al., 1988). Here, the second factor has been taken in consideration in our model. Clearly, our numerical results on the hole evolution are in a better agreement with the experiments both in the upstream and in the downstream direction, compared with Roulund et al. (2005). The simulation results from reference have reached the equilibrium condition at about 1000s, but with scoured depth values smaller than the experiment. Our results are closer to the experiment in both upstream and downstream part.

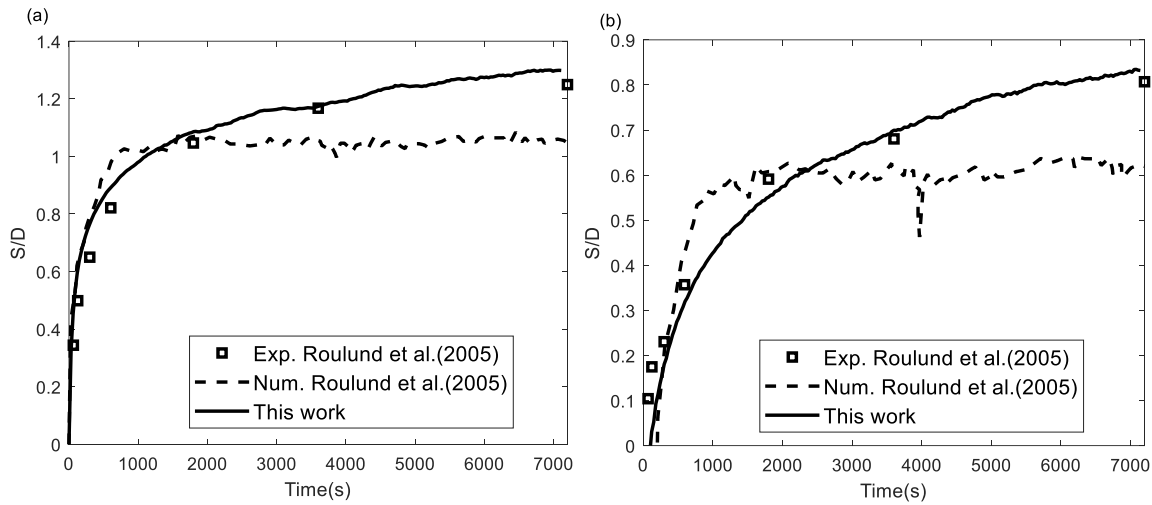


Figure 4.27: Numerical (Num.) and experimental (Exp.) results of the scour depth evolution at the (a) upstream, and (b) downstream side of the cylinder for the live bed case.

4.4. Conclusion

In this chapter, large eddy simulation is conducted to study the hydrodynamics and the scour process around a circular cylinder. Sigma-coordinates system is employed to follow sediment-water interface. Bed erosion is simulated by solving the sediment continuity equation in the bedload layer using a mass-conservative-based algorithm for sand-slide, and a bedload transport rate, which is based on a description of physical processes (Engelund & Fredsøe, 1976). This model has been rigorously validated for the rigid bed case by comparing with the previous studies (Kirkil et al., 2008, 2010, 2015; Sahin and Ozturk, 2009; Roulund et al., 2005). Simulation of scour process around a cylinder for the live bed case proposed by Roulund et al. (2005), with $H = 4D$ at $Re_D = 46,000$ until the equilibrium condition is then carried out.

In the rigid bed case, the HV system composed by U-shape necklace vortices such as Primary Vortex (PV), Bottom-Attached Vortices (BAV) and Secondary Vortex (SV) is relatively stable and under a oscillating cycle. Moreover, along the upstream face of the cylinder, there is a small, but very coherent, junction vortex appears at the base of the cylinder (JV). The number of PV, BAV depends on the Reynolds number and relative thickness of boundary layers. For $H = 4D$ at $Re_D = 46,000$, in the instantaneous flows, there are two PV, two BAV. During an oscillating cycle, two PV move oppositely, and at the end, find again nearly the same places where initially they are. The oscillating distance is about $0.1D$. The legs of PV are nearly parallel to the incoming flow. They still maintain downstream the cylinder until the position $x = 2D$. It seems that the flow coherent structure is not depending on the relative water depth H/D . Indeed, the HV system structure in our studied cases has the same than that of Kirkil et al (2008) for $H/D = 1.12$.

In the live bed, the HV system also composed of PV and BV. The HV system is in a close relationship with the scour process, and unstable. It becomes more stable when the scour hole is formed. The HV system is responsible for the scour process. Indeed, the cylinder obstruction generates the local redistribution of pressure, and induces down flows at the upstream face of the cylinder. That generates primary vortex (PV). On the other hand, following the HV, streamlines wrap the cylinder from both lateral sides, converging at a nodal point. From there, thanks to an upwelling vortex, fluids rises up into the free surface layers, entraining sediment particles situated on the bed, and bringing them downstream to deposit somewhere. This generates the scour process. The current work has focused on the coherent structure of flow fields and the scour process until its equilibrium state. Simulations performed with the NSMP3D model better reproduce the scour evolution as the experiment and show HV oscillation than the simulations of Roulund et al (2005), who rest on a model of turbulence ($\kappa - \omega$) which can't capture the oscillations of wake vortices.

Chapter 5

Conclusions and Perspectives

An accurate and efficient numerical solver, named as NSMP3D, has been developed for modelling non-hydrostatic turbulent flows using unstructured finite volume method with large eddy simulation. NSMP3D has been validated by several test cases to check the accuracy order of the proposed numerical techniques and its ability in turbulent flow simulations. The test case of 2D decaying vortex shows that NSMP3D got second order of accuracy in space and in time, which permits the simulations of non-hydrostatic flows at moderate Reynolds numbers. The vertical profiles of velocity computed by NSMP3D from turbulent channel flows using DNS and LES are in a good agreement with the previous studies. The test case of lid-driven cavity flows shows that NSMP3D can provide the results equivalent to those obtained from the previous numerical studies, even they used finer computational meshes. In the test case of flows around a vertical cylinder, the time averaged pressure coefficient for 2D problem and horseshoe vortex oscillation for 3D problem at moderate Reynolds number calculated by NSMP3D have been compared with previous experimental and numerical studies. Fair agreements have been obtained. Coherent structure of flows has been shown. Clearly, the proposed PM construction using a combination of momentum interpolation and center schemes has been proved to be robust, accurate and reliable for further researches and applications

A Navier-Stokes solver based on projection method and a second-order unstructured finite-volume mesh, using LES is newly developed to simulate the hydrodynamics and the scour process around a circular cylinder. A sigma-coordinate system is employed to follow the sediment-water interface. Bed erosion is simulated by solving the sediment continuity equation in the bedload layer using a mass-conservative-based algorithm for sand-slide and a bedload transport rate based on a description of physical processes (Engelund & Fredsøe, 1976). The present model has been rigorously validated for free slip bed case and the rigid bed case through comparison with previous studies. Then, the simulation of scour process

around a cylinder for the live bed case with $h=4D$ and $Re_D=46,000$ is then carried out until its equilibrium state.

Our model reproduces the shear stress observed by Roulund et al. (2005) in the vicinity of the cylinder with very slight discrepancy far away from it. The HV system is relatively stable and under an oscillating cycle. It is composed of primary, bottom-attached and secondary necklace vortices and a small coherent junction vortex. For $h = 4D$ and $Re_D = 46,000$, there are two primary and two bottom-attached vortices in instantaneous flows. During an oscillating cycle, two primary vortices move in opposite directions, and in the end, they return to approximate their initial positions. The oscillating distance is about $0.1D$. The legs of primary vortices are nearly parallel to the incoming flow and they are still maintained downstream the cylinder until the position $x = 2D$. Indeed, the HV structure in the case we document has almost the same structure as Kirkil et al. (2008) for $h/D = 1.12$.

The HV system is in a closely related to the scour process. It is unstable at the initial stage of scour and then becomes more stable as the scour hole is formed. The obstruction caused by the cylinder generates the local redistribution of pressure and induces down flows at the upstream face of the cylinder generating primary vortices. Streamlines wrap the cylinder from both lateral sides, converging at a nodal point at the downstream. From there, due to an upwelling vortex, fluids rise up into the surface, entraining the sediment particles situated on the bed, bringing them downstream to deposit somewhere else. This generates the scour process behind the cylinder.

Concerning the scour around a vertical cylinder, this work bring an evident novelty in comparing with the previous studies. Indeed, while Kirkil et al. (2008, 2010, 2015) have described the HV system without the scour process, and Roulund et al. (2005) had only studied the scour process without talking about the HV system, this work has described on both the HV system and the scour process until its equilibrium state in detail. Moreover, the 3D wake region behind the cylinder has also been shown up to deepen our knowledge during evolution of the scour process

In the future work, two phase modules will be implemented by introducing the Eulerian-Eulerian approach to provide solutions for renewed issues in real engineering applications.

Reference

- Bahaj, A. S., & Myers, L. E. (2003). Fundamentals applicable to the utilisation of marine current turbines for energy production. *Renewable Energy*, 28(14), 2205–2211.
- Bai, W., Mingham, C. G., Causon, D. M., & Qian, L. (2016). Detached eddy simulation of turbulent flow around square and circular cylinders on Cartesian cut cells. *Ocean Engineering*, 117, 1–14.
- Baker, C. J. (1979). The laminar horseshoe vortex. *Journal of Fluid Mechanics*, 95(02), 347–367.
- Baykal, C., Sumer, B. M., Fuhrman, D. R., Jacobsen, N. G., & Fredsoe, J. (2014). Numerical investigation of flow and scour around a vertical circular cylinder. *Philosophical Transactions of the Royal Society A: Mathematical, Physical and Engineering Sciences*, 373(2033), 104.
- Baykal, C., Sumer, B. M., Fuhrman, D. R., Jacobsen, N. G., & Fredsøe, J. (2017). Numerical simulation of scour and backfilling processes around a circular pile in waves. *Coastal Engineering*, 122, 87–107.
- Beji, S., & Battjes, J. A. (1994). Numerical simulation of nonlinear wave propagation over a bar. *Coastal Engineering*, 23(1–2), 1–16.
- Bouffanais, R., Deville, M. O., & Leriche, E. (2007). Large-eddy simulation of the flow in a lid-driven cubical cavity. *Physics of Fluids*, 19(5), 055108.
- Braza, M., Chassaing, P., & Minh, H. H. (n.d.). *Numerical study and physical analysis of the pressure and velocity fields in the near wake of a circular cylinder*. 53.
- Breusers, H. N. C., Nicollet, G., & Shen, H. W. (1977). Local Scour Around Cylindrical Piers. *Journal of Hydraulic Research*, 15(3), 211–252.

- Broglia, R., Pascarelli, A., & Piomelli, U. (2003). Large-eddy simulations of ducts with a free surface. *Journal of Fluid Mechanics*, 484, 223–253.
- Cantero, M. I., Balachandar, S., Cantelli, A., Pirmez, C., & Parker, G. (2009). Turbidity current with a roof: Direct numerical simulation of self-stratified turbulent channel flow driven by suspended sediment. *Journal of Geophysical Research*, 114(C3), C03008.
- Cantero, M. I., Balachandar, S., García, M. H., & Bock, D. (2008). Turbulent structures in planar gravity currents and their influence on the flow dynamics. *Journal of Geophysical Research*, 113(C8), C08018.
- Capuano, F., Mastellone, A., & De Angelis, E. M. (2017). A conservative overlap method for multi-block parallelization of compact finite-volume schemes. *Computers & Fluids*, 159, 327–337.
- Casulli, V. (1999). A semi-implicit finite difference method for non-hydrostatic, free-surface flows. *International Journal for Numerical Methods in Fluids*, 30(4), 425–440.
- Chakraborty, P., Balachandar, S., & Adrian, R. J. (2005). On the relationships between local vortex identification schemes. *Journal of Fluid Mechanics*, 535, 189–214.
- Chauchat, J., Guillou, S., Pham Van Bang, D., & Dan Nguyen, K. (2013). Modelling sedimentation–consolidation in the framework of a one-dimensional two-phase flow model. *Journal of Hydraulic Research*, 51(3), 293–305.
- Chen, C., Liu, H., & Beardsley, R. C. (2003). An unstructured grid, Finite-Volume, three-dimensional, primitive equations ocean model: application to coastal ocean and estuaries. *Journal of Atmospheric and Oceanic Technology*, 20(1), 159–186.
- Chorin, A. J. (1968). Numerical solution of the Navier-Stokes equations. *Mathematics of Computation*, 22(104), 745–762.
- Cui, H., Pietrzak, J. D., & Stelling, G. S. (2012). Improved efficiency of a non-hydrostatic, unstructured grid, finite volume model. *Ocean Modelling*, 54–55, 55–67.

- Dalal, A., Eswaran, V., & Biswas, G. (2008). A Finite-Volume method for Navier-Stokes equations on unstructured meshes. *Numerical Heat Transfer, Part B: Fundamentals*, 54(3), 238–259.
- Dargahi, B. (1989). The turbulent flow field around a circular cylinder. *Experiments in Fluids*, 8(1–2), 1–12.
- Dargahi, B. (1990). Controlling mechanism of local scouring. *Journal of Hydraulic Engineering*, 116(10), 1197–1214.
- Davidson, L. (1996). A pressure correction method for unstructured meshes with arbitrary control volumes. *International Journal for Numerical Methods in Fluids*, 22(4), 265–281.
- Deardorff, J. W. (1970). A numerical study of three-dimensional turbulent channel flow at large Reynolds numbers. *Journal of Fluid Mechanics*, 41(02), 453–480.
- Debnath, K., & Chaudhuri, S. (2010). Laboratory experiments on local scour around cylinder for clay and clay–sand mixed beds. *Engineering Geology*, 111(1–4), 51–61.
- Dey, S., & Raikar, R. V. (2007). Characteristics of horseshoe vortex in developing scour holes at piers. *Journal of Hydraulic Engineering*, 133(4), 399–413.
- Ducros, F., Laporte, F., Soulères, T., Guinot, V., Moinat, P., & Caruelle, B. (2000). High-Order Fluxes for Conservative Skew-Symmetric-like Schemes in Structured Meshes: Application to Compressible Flows. *Journal of Computational Physics*, 161(1), 114–139.
- Eckelmann, H. (1974). The structure of the viscous sublayer and the adjacent wall region in a turbulent channel flow. *Journal of Fluid Mechanics*, 65(03), 439.
- Engelund, F., & Fredsøe, J. (1976). A sediment transport model for straight alluvial channels. *Hydrology Research*, 7(5), 293–306.

- Enright, D., Fedkiw, R., Ferziger, J., & Mitchell, I. (2002). A Hybrid Particle Level Set Method for Improved Interface Capturing. *Journal of Computational Physics*, 183(1), 83–116.
- Ettema, R., Constantinescu, G., & Melville, B. (2011). *Evaluation of bridge scour research: pier scour processes and predictions* (p. 175). NCHRP Rep.
- EWEA. (2017). *Wind in power 2017: Annual combined onshore and offshore wind energy statistics*.
- Fernandez Luque, R., & Van Beek, R. (1976). Erosion and transport of bed-load sediment. *Journal of Hydraulic Research*, 14(2), 127–144.
- Ferziger, J. H., & Perić, M. (2002). *Computational methods for fluid dynamics* (3rd, rev. ed ed.). Berlin ; New York: Springer.
- Fredsøe, J., & Deigaard, R. (1992). *Mechanics of coastal sediment transport*. Singapore: World Scientific.
- Garcia, M., & Parker, G. (1991). Entrainment of Bed Sediment into Suspension. *Journal of Hydraulic Engineering*, 117(4), 414–435.
- Geyer, W. R. (1993). The Importance of Suppression of Turbulence by Stratification on the Estuarine Turbidity Maximum. *Estuaries*, 16(1), 113.
- Ghia, U., Ghia, K. N., & Shin, C. T. (1982). High-Re solutions for incompressible flow using the Navier-Stokes equations and a multigrid method. *Journal of Computational Physics*, 48(3), 387–411.
- Gorobets, A. V. (2015). Parallel technology for numerical modeling of fluid dynamics problems by high-accuracy algorithms. *Computational Mathematics and Mathematical Physics*, 55(4), 638–649.
- Graf, W. H., & Istiarto, I. (2002). Flow pattern in the scour hole around a cylinder. *Journal of Hydraulic Research*, 40(1), 13–20.

- Graf, W. H., & Yulistiyanto, B. (1998). Experiments on flow around a cylinder; the velocity and vorticity fields. *Journal of Hydraulic Research*, 36(4), 637–654.
- Hjorth, P. (1975). *Studies on the nature of local scour*. Inst. för Teknisk Vattenresurslära, Lunds Tekniska Högskola, Lunds Univ.
- Hoeksema, W. (2014). *Innovative solution for seafastening offshore wind turbine transition pieces during transport*. Delft university of technology.
- Homann, F. (1936). Der Einfluß großer Zähigkeit bei der Strömung um den Zylinder und um die Kugel. *ZAMM - Zeitschrift für Angewandte Mathematik und Mechanik*, 16(3), 153–164.
- Horvat, Z., Isic, M., & Spasojevic, M. (2015). Two dimensional river flow and sediment transport model. *Environmental Fluid Mechanics*, 15(3), 595–625.
- Hsu, T.-J. (2004). Toward modeling turbulent suspension of sand in the nearshore. *Journal of Geophysical Research*, 109(C6).
- Huang, T.-C., Chang, C.-Y., & Lin, C.-A. (2018). Simulation of droplet dynamic with high density ratio two-phase lattice Boltzmann model on multi-GPU cluster. *Computers & Fluids*, 173, 80–87.
- Huber, F. (1991). Update: bridge scour. *Civil Engineering, ASCE*, 61(9), 62–63.
- Jan, Y.-J., & Sheu, T. W.-H. (2007a). A quasi-implicit time advancing scheme for unsteady incompressible flow. Part I: Validation. *Comput. Methods Appl. Mech. Engrg.*, 16.
- Jan, Y.-J., & Sheu, T. W.-H. (2007b). A quasi-implicit time advancing scheme for unsteady incompressible flow. Part I: Validation. *Computer Methods in Applied Mechanics and Engineering*, 196(45–48), 4755–4770.
- Jarrin, N. (2008). *Synthetic inflow boundary conditions for the numerical simulation of turbulence*. University of Manchester.

- Ji, C., Munjiza, A., & Williams, J. J. R. (2012). A novel iterative direct-forcing immersed boundary method and its finite volume applications. *Journal of Computational Physics*, 231(4), 1797–1821.
- Johnson, K. R., & Ting, F. C. K. (2003). Measurements of water surface profile and velocity field at a circular pier. *Journal of Engineering Mechanics*, 129(5), 502–513.
- Kawano, A. (2016). A simple volume-of-fluid reconstruction method for three-dimensional two-phase flows. *Computers & Fluids*, 134–135, 130–145.
- Khosronejad, A., Kang, S., Borazjani, I., & Sotiropoulos, F. (2011). Curvilinear immersed boundary method for simulating coupled flow and bed morphodynamic interactions due to sediment transport phenomena. *Advances in Water Resources*, 34(7), 829–843.
- Khosronejad, A., Kang, S., & Sotiropoulos, F. (2012). Experimental and computational investigation of local scour around bridge piers. *Advances in Water Resources*, 37, 73–85.
- Kim, D., & Choi, H. (2000). A second-order time-accurate finite volume method for unsteady incompressible flow on hybrid unstructured grids. *Journal of Computational Physics*, 162(2), 411–428.
- Kim, H., Roh, M., & Nabi, M. (2017). Computational Modeling of Flow and Scour around Two Cylinders in Staggered Array. *Water*, 9(9), 654.
- Kim, J., Moin, P., & Moser, R. (1987). Turbulence statistics in fully developed channel flow at low Reynolds number. *Journal of Fluid Mechanics*, 177(1), 133–166.
- Kirkil, G., Constantinescu, S. G., & Ettema, R. (2008). Coherent structures in the flow field around a circular cylinder with scour hole. *Journal of Hydraulic Engineering*, 134(5), 572–587.
- Kirkil, Gokhan, & Constantinescu, G. (2010). Flow and turbulence structure around an in-stream rectangular cylinder with scour hole: flow around a rectangular culinder. *Water Resources Research*, 46(11).

- Kirkil, Gokhan, & Constantinescu, G. (2012). A numerical study of the laminar necklace vortex system and its effect on the wake for a circular cylinder. *Physics of Fluids*, 24(7), 073602.
- Kirkil, Gokhan, & Constantinescu, G. (2015). Effects of cylinder Reynolds number on the turbulent horseshoe vortex system and near wake of a surface-mounted circular cylinder. *Physics of Fluids*, 27(7), 075102.
- Koçyigit, M. B., Falconer, R. A., & Lin, B. (2002). Three-dimensional numerical modelling of free surface flows with non-hydrostatic pressure: 3D modelling of free surface flows. *International Journal for Numerical Methods in Fluids*, 40(9), 1145–1162.
- Komori, S., Murakami, Y., & Ueda, H. (1989). The relationship between surface-renewal and bursting motions in an open-channel flow. *Journal of Fluid Mechanics*, 203, 103–123.
- Kothyari, U. C., Hager, W. H., & Oliveto, G. (2007). Generalized approach for clear-water scour at bridge foundation elements. *Journal of Hydraulic Engineering*, 133(11), 1229–1240.
- Lachaussée, F., Bertho, Y., Morize, C., Sauret, A., & Gondret, P. (2018). Competitive dynamics of two erosion patterns around a cylinder. *Physical Review Fluids*, 3(1).
- Lança, R. M., Fael, C. S., Maia, R. J., Pêgo, J. P., & Cardoso, A. H. (2013). Clear-water scour at comparatively large cylindrical piers. *Journal of Hydraulic Engineering*, 139(11), 1117–1125.
- Launay, G. (2016). *Experimental study of the horseshoe vortex at the foot of a emergent obstacle in a laminar free-surface flow*. École centrale de Lyon.
- Levy, M., & Salvadori, M. (2002). *Why buildings fall down: how structures fail* (Updated and expanded). New York: W.W. Norton.
- Liang, S.-J., Jan, Y.-J., & Huang, C.-A. (2013). A quasi-Implicit time-advancing scheme for flow in a three-dimensional curved duct. *Numerical Heat Transfer, Part B: Fundamentals*, 64(4), 306–325.

- Lien, F.-S. (2000). A pressure-based unstructured grid method for all-speed flows. *International Journal for Numerical Methods in Fluids*, 33(3), 355–374.
- Lilly, D. K. (1967). The representation of small-scale turbulence in numerical simulation experiments. *Proceedings of IBM Scientific Computing Symposium on Environmental Sciences*, pp. 195–210.
- Lin, C., Lai, W.-J., & Chang, K.-A. (2003). Simultaneous Particle Image Velocimetry and Laser Doppler Velocimetry Measurements of Periodical Oscillatory Horseshoe Vortex System near Square Cylinder-Base Plate Junction. *Journal of Engineering Mechanics*, 129(10), 1173–1188.
- Link, O., González, C., Maldonado, M., & Escarriaza, C. (2012). Coherent structure dynamics and sediment particle motion around a cylindrical pier in developing scour holes. *Acta Geophysica*, 60(6), 1689–1719.
- Liu, D., Liu, X., & Fu, X. (2018). LES-DEM simulations of sediment saltation in a rough-wall turbulent boundary layer. *Journal of Hydraulic Research*, 1–12.
- Lourenco, L. M. (1993). Characteristics of the Plane Turbulent Near Wake of a Circular Cylinder. *A Particle Image Velocimetry Study*. Retrieved from <https://ci.nii.ac.jp/naid/10009520643/en/>
- Ma, G., Shi, F., & Kirby, J. T. (2012). Shock-capturing non-hydrostatic model for fully dispersive surface wave processes. *Ocean Modelling*, 43, 22–35.
- Mahesh, K., Constantinescu, G., Apte, S., Iaccarino, G., Ham, F., & Moin, P. (2006). Large-Eddy simulation of reacting turbulent flows in complex geometries. *Journal of Applied Mechanics*, 73(3), 374–381.
- Mahesh, K., Constantinescu, G., & Moin, P. (2004). A numerical method for large-eddy simulation in complex geometries. *Journal of Computational Physics*, 197(1), 215–240.

- Manes, C., & Brocchini, M. (2015). Local scour around structures and the phenomenology of turbulence. *Journal of Fluid Mechanics*, 779, 309–324.
- Mason, P. J., & Thomson, D. J. (1992). Stochastic backscatter in large-eddy simulations of boundary layers. *Journal of Fluid Mechanics*, 242(1), 51.
- Matutano, C., Negro, V., López-Gutiérrez, J.-S., & Esteban, M. D. (2013). Scour prediction and scour protections in offshore wind farms. *Renewable Energy*, 57, 358–365.
- McKnight, T. L., & Hess, D. (2000). *Physical geography—A landscape appreciation*, (6th ed.). Upper Saddle River, N.J Prentice Hall.
- Meland, N., & Norrman, J. O. (1966). Transport velocities of single particles in bed-load motion. *Geografiska Annaler. Series A, Physical Geography*, 48(4), 165.
- Melville, B. W., & Chiew, Y.-M. (1999). Time scale for local scour at bridge piers. *Journal of Hydraulic Engineering*, 125(1), 59–65.
- Mittal, S. (2005). Excitation of shear layer instability in flow past a cylinder at low Reynolds number. *International Journal for Numerical Methods in Fluids*, 49(10), 1147–1167.
- Mucha, P. J., & Brenner, M. P. (2003). Diffusivities and front propagation in sedimentation. *Physics of Fluids*, 15(5), 1305–1313.
- Nagaosa, R. (1999). Direct numerical simulation of vortex structures and turbulent scalar transfer across a free surface in a fully developed turbulence. *Physics of Fluids*, 11(6), 1581–1595.
- Nagel, T. (2018). *Numerical study of multi-scale flow-sediment-structure interactions using a multiphase approach* (Doctoral dissertation, Université Grenoble alpes). Retrieved from <https://tel.archives-ouvertes.fr/tel-01920495/>
- Necker, F., Härtel, C., Kleiser, L., & Meiburg, E. (2005). Mixing and dissipation in particle-driven gravity currents. *Journal of Fluid Mechanics*, 545(1), 339–372.
- Nezu, I., Nakagawa, H., & Jirka, G. H. (1994). Turbulence in open-channel Flows. *Journal of Hydraulic Engineering*, 120(10), 1235–1237.

- Nikuradse, J. (1933). *Laws of flow in rough pipes*. Washington: VDI Forschungsheft.
- Nishioka, M., & Sato, H. (1974). Measurements of velocity distributions in the wake of a circular cylinder at low Reynolds numbers. *Journal of Fluid Mechanics*, 65(01), 97–112.
- Okong'O, N., Knight, D. D., & Zhou, G. (2000). Large Eddy Simulations Using an Unstructured Grid Compressible Navier - Stokes Algorithm. *International Journal of Computational Fluid Dynamics*, 13(4), 303–326.
- Ong, L., & Wallace, J. (1996). The velocity field of the turbulent very near wake of a circular cylinder. *Experiments in Fluids*, 441–453.
- Othmar H, A., Theodore, von K., & Glenn B, W. (1941). *The failure of the Tacoma Narrows Bridge*. Washington D.C: Federal Works Agency.
- Pan, Y., & Banerjee, S. (1995). A numerical study of free-surface turbulence in channel flow. *Physics of Fluids*, 7(7), 1649–1664.
- Park, J. C., Kim, M. H., & Miyata, H. (1999). Fully non-linear free-surface simulations by a 3D viscous numerical wave tank. *International Journal for Numerical Methods in Fluids*, 29(6), 685–703.
- Park, J., Kwon, K., & Choi, H. (1998). Numerical solutions of flow past a circular cylinder at Reynolds numbers up to 160. *KSME International Journal*, 12(6), 1200–1205.
- Parker, G. (2008). Transport of gravel and sediment mixtures. *ASCE*, 165–252.
- Perot, J. B. (1993). An Analysis of the Fractional Step Method. *Journal of Computational Physics*, 108(1), 51–58.
- Pham Van Bang, D., Lefrançois, E., Sergent, P., & Bertrand, F. (2008). Expérimentation par IRM et modélisation par éléments finis de la sédimentation-consolidation des vases. *La Houille Blanche*, (3), 39–44.
- Phillips, N. A. (1957). A coordinate system having some special advantages for numerical forecasting. *Journal of Meteorology*, 14(2), 184–185.

- Pope, S. B. (2000). *Turbulent flows*. Cambridge ; New York: Cambridge University Press.
- Qu, L., Norberg, C., Davidson, L., Peng, S.-H., & Wang, F. (2013). Quantitative numerical analysis of flow past a circular cylinder at Reynolds number between 50 and 200. *Journal of Fluids and Structures*, 39, 347–370.
- Rajani, B. N., Kandasamy, A., & Majumdar, S. (2009). Numerical simulation of laminar flow past a circular cylinder. *Applied Mathematical Modelling*, 33(3), 1228–1247.
- REN21. (2018). *Renewables 2018: Global Status Report* (p. 43).
- Rhie, C. M., & Chow, W. L. (1983). Numerical study of the turbulent flow past an airfoil with trailing edge separation. *AIAA Journal*, 21(11), 1525–1532.
- Robinson, S. K. (1991). Coherent Motions in the Turbulent Boundary Layer. *Annual Review of Fluid Mechanics*, 23(1), 601–639.
- Rodi, W., Constantinescu, G., & Stroesser, T. (2013). *Large-Eddy Simulation in hydraulics*. Boca Raton: CRC Press.
- Roulund, A., Sumer, B. M., Fredsøe, J., & Michelsen, J. (2005). Numerical and experimental investigation of flow and scour around a circular pile. *Journal of Fluid Mechanics*, 534, 351–401.
- Rouse, H. (1937). Modern Conceptions of the Mechanics or Fluid Turbulence. *Transactions of the American Society of Civil Engineers*, 102(1), 463–505.
- Sahin, B., & Ozturk, N. A. (2009). Behaviour of flow at the junction of cylinder and base plate in deep water. *Measurement*, 42(2), 225–240.
- Segrè, P. N., Liu, F., Umbanhowar, P., & Weitz, D. A. (2001). An effective gravitational temperature for sedimentation. *Nature*, 409(6820), 594–597.
- Sheppard, D. M., Odeh, M., & Glasser, T. (2004). Large scale clear-water local pier scour experiments. *Journal of Hydraulic Engineering*, 130(10), 957–963.

- Shi, Y., Ray, R. K., & Nguyen, K. D. (2013). A projection method-based model with the exact C-property for shallow-water flows over dry and irregular bottom using unstructured finite-volume technique. *Computers & Fluids*, 76, 178–195.
- Shields, A. (1936). *Anwendung der aehnlichkeitsmechanik und der turbulenzforschung auf die geschiebebewegung*. Technical University Berlin.
- Shringarpure, M., Cantero, M. I., & Balachandar, S. (2012). Dynamics of complete turbulence suppression in turbidity currents driven by monodisperse suspensions of sediment. *Journal of Fluid Mechanics*, 712, 384–417.
- Stahlmann, A. (2013). *Numerical and experimental modeling of scour at foundation structures for offshore wind turbines*. Presented at the International Society of Offshore and Polar Engineers, Poland. Retrieved from <http://www.isopec.org/publications>
- Steijl, R., & Barakos, G. N. (2018). Parallel evaluation of quantum algorithms for computational fluid dynamics. *Computers & Fluids*, 173, 22–28.
- Stelling, G., & Zijlema, M. (2003). An accurate and efficient finite-difference algorithm for non-hydrostatic free-surface flow with application to wave propagation. *International Journal for Numerical Methods in Fluids*, 43(1), 1–23.
- Sumer, B. M. (2014). Flow–structure–seabed interactions in coastal and marine environments. *Journal of Hydraulic Research*, 52(1), 1–13.
- Sumer, B. M., & Fredsøe, J. (1997). *Hydrodynamics around cylindrical structures*.
- Sumer, B. M., Fredsøe, J., & Christiansen, N. (1992). Scour Around Vertical Pile in Waves. *Journal of Waterway, Port, Coastal, and Ocean Engineering*, 118(1), 15–31.
- Sumer, B. M., Jensen, H. R., Mao, Y., & Fredsøe, J. (1988). Effect of Lee-Wake on Scour Below Pipelines in Current. *Journal of Waterway, Port, Coastal, and Ocean Engineering*, 114(5), 599–614.

- Tang, L. Q., Cheng, T., & Tsang, T. T. H. (1995). Transient solutions for three-dimensional lid-driven cavity flows by a least-squares finite element method. *International Journal for Numerical Methods in Fluids*, 21(5), 413–432.
- Thom, A. (1933). The flow past circular cylinders at low speeds. *Proceedings of the Royal Society A: Mathematical, Physical and Engineering Sciences*, 141(845), 651–669.
- Thomas, T. G., & Williams, J. J. R. (1995). Turbulent simulation of open channel flow at low Reynolds number. *International Journal of Heat and Mass Transfer*, 38(2), 259–266.
- Tremblay, F., Manhart, M., & Friedrich, R. (2000). LES of Flow around a Circular Cylinder at a Subcritical Reynolds Number with Cartesian Grids. *8th European Turbulence Conference*, 659–662. Barcelona, Spain.
- Uh Zapata, M., Pham Van Bang, D., & Nguyen, K. D. (2018). Parallel simulations for a 2D x/z two-phase flow fluid-solid particle model. *Computers & Fluids*, 173, 103–110.
- Uh Zapata, Miguel, Pham Van Bang, D., & Nguyen, K. D. (2014). An unstructured finite volume technique for the 3D Poisson equation on arbitrary geometry using a sigma - coordinate system. *International Journal for Numerical Methods in Fluids*, 76(10), 611–631.
- Uh Zapata, Miguel, Pham Van Bang, D., & Nguyen, K. D. (2016). Parallel SOR methods with a parabolic-diffusion acceleration technique for solving an unstructured-grid Poisson equation on 3D arbitrary geometries. *International Journal of Computational Fluid Dynamics*, 30(5), 370–385.
- Uh Zapata, Miguel, Zhang, W., Pham Van Bang, D., & Nguyen, K. D. (2019). A parallel second-order unstructured finite volume method for 3D free-surface flows using a σ coordinate. *Computers & Fluids*, S0045793018308697.
- Van Rijn, L. C. (1984). Sediment transport, Part I: bed load transport. *Journal of Hydraulic Engineering*, 110(10), 1431–1456.

- Watchorn, M., & Trapp, T. (2000). Tidal stream renewable offshore power generation (TS-Ropg). In *World Renewable Energy Congress VI* (pp. 2664–2667).
- Williamson, C. H. K. (1989). Oblique and parallel modes of vortex shedding in the wake of a circular cylinder at low Reynolds numbers. *Journal of Fluid Mechanics*, 206(1), 579–627.
- World energy council. (2016). *World energy resources: marine energy* (p. 4).
- Wu, W. (2004). Depth-Averaged Two-Dimensional Numerical Modeling of Unsteady Flow and Nonuniform Sediment Transport in Open Channels. *Journal of Hydraulic Engineering*, 130(10), 1013–1024.
- Xue, S.-C., & Barton, G. W. (2013). A finite volume formulation for transient convection and diffusion equations with unstructured distorted grids and its applications in fluid flow simulations with a collocated variable arrangement. *Computer Methods in Applied Mechanics and Engineering*, 253, 146–159.
- Yuan, H., & Wu, C. H. (2004). An implicit three-dimensional fully non-hydrostatic model for free-surface flows. *International Journal for Numerical Methods in Fluids*, 46(7), 709–733.
- Zalesak, S. T. (1979). Fully multidimensional flux-corrected transport algorithms for fluids. *Journal of Computational Physics*, 31(3), 335–362.
- Zang, Y., Street, R. L., & Koseff, J. R. (1994). A non-staggered grid, fractional step method for time-dependent incompressible Navier-Stokes equations in curvilinear coordinates. *Journal of Computational Physics*, 114(1), 18–33.
- Zhang, W., Uh Zapata, M., Bai, X., Pham Van Bang, D., & NGUYEN, K. D. (2019a). 3D simulation of horseshoe vortex and local scour around a vertical cylinder using an unstructured finite-volume technique. *International Journal of Sediment Research*. <https://doi.org/revised submitted>

- Zhang, W., Uh Zapata, M., Bai, X., Pham Van Bang, D., & NGUYEN, K. D. (2019b). A combined momentum interpolation and centre schemes for 3D incompressible, non-hydrostatic turbulent flow solver based on projection methods in unstructured grids. *European Journal of Mechanics B/Fluids*. <https://doi.org/revised submitted>
- Zhao, M., Cheng, L., & Zang, Z. (2010). Experimental and numerical investigation of local scour around a submerged vertical circular cylinder in steady currents. *Coastal Engineering*, 57(8), 709–721.
- Zhao, N., & Wang, X. (2012). A Parallel Preconditioned Bi-Conjugate Gradient Stabilized Solver for the Poisson Problem. *Journal of Computers*, 7(12), 3088–3095.
- Zhou, J., Adrian, R. J., Balachandar, S., & Kendall, T. M. (1999). Mechanisms for generating coherent packets of hairpin vortices in channel flow. *Journal of Fluid Mechanics*, 387, 353–396.
- Zhou, L. (2017). *Numerical modelling of scour in steady flows* (Doctoral dissertation, École centrale de Lyon). Retrieved from <https://tel.archives-ouvertes.fr/tel-01598600>
- Zhu, H., Wang, L., & Tang, H. (2013). Large-eddy simulation of suspended sediment transport in turbulent channel flow. *Journal of Hydrodynamics*, 25(1), 48–55.
- Zlamal, M. (1978). Superconvergence and Reduced Integration in the Finite Element Method. *Mathematics of Computation*, 32(143), 663.

Appendix A.

Periodic boundary condition in parallel computation

In turbulent channel flows, it is necessary to have a periodic boundary condition to represent a computational domain with infinite length or width. From that, both steady and unsteady flow simulations can be considered and analysed, avoiding the difficulty and effort to construct a very large domain.

This appendix details the implementation of periodic boundary conditions for problems with simple geometry but unstructured mesh. The implementation is done by using MPI library to enable distribution of computing effort on cluster of CPU or supercomputing facility.

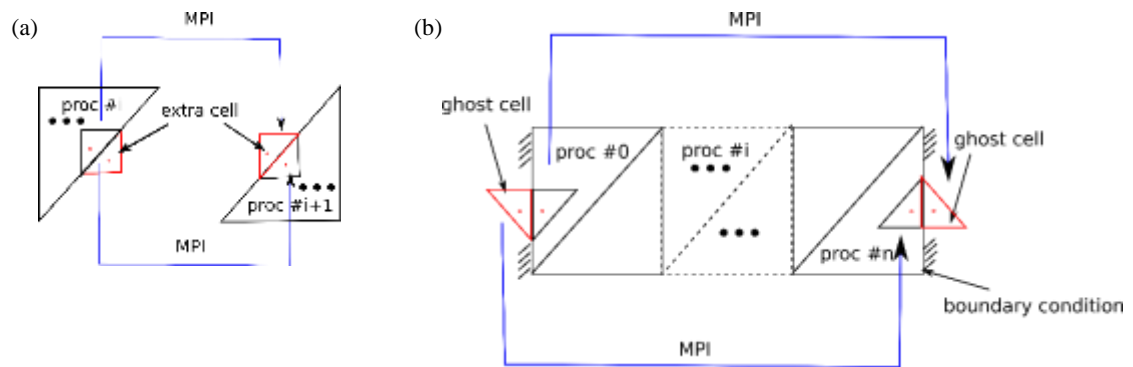


Figure A.1: Memory structure in the original MPI code.

In the parallel scheme of NSMP3D, the computational domain is first divided into a number of smaller subdomains (number i , or $\#i$). Each subdomain is then mapped onto independent processor of a computer cluster. Therefore, each processor only deals with the task of field computation of a much smaller subdomain, relieving the burdens on both the computer memory and the CPU time, in comparison to that experienced when attempting to

solve the original problem using a single processor. Data communication between processors is carried out by using the Message Passing Interface (MPI) library.

In Figure A.1, additional group of cells at each subdomain are introduced: Extra and ghost cells. Extra cells are in the inner subdomain, which contain the information of the overlapping boundaries, are computed or updated by MPI subroutines. Ghost cells are outside of the domain, which contain the information of the physical boundaries such as wall, discharge or free surface boundaries.

I. Modification of memory structure

The (initial) memory structure for each subdomain ($\#i$) is illustrated in Figure A.2. For a subdomain i (which is handled by processor $\#i$), the inner (N_Cell_i) and ghost (N_CELL_{ghost}) cells are stored as local variables. The information of the overlapping cells (Extra cell) are stored as global variables since they are obtained from other neighbouring processors.

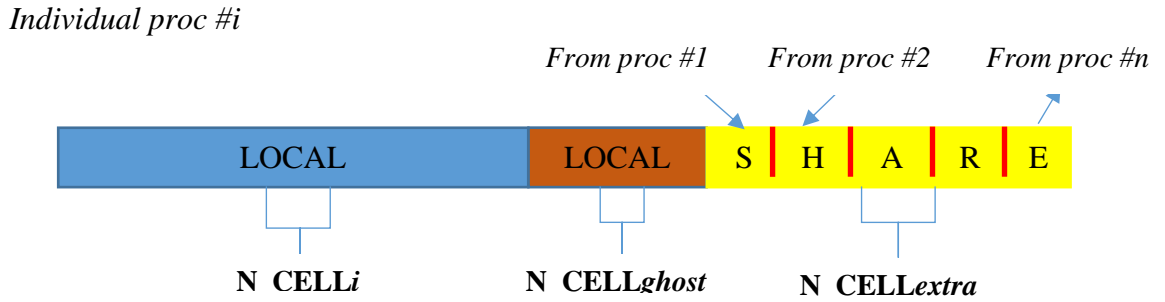


Figure A.2: Memory structure in the original MPI code.

Now, for the implementation of periodic boundary conditions, the category of ghost cells are divided in two subcategories: the previous ghost cells with information stored as local variables; the new ghost cells with information of periodic boundary. These ‘*periodic*’ ghost cells are stored as global variables since information are shared variables like the extra cells. Figure A.3 presents the modified structure of ghost cells with similar legend as in Figure A.2: brown colour for local variables and yellow colour for global variables.

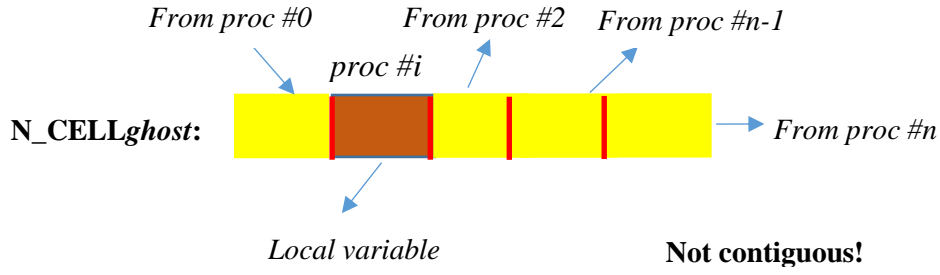


Figure A.3: New memory structure for the ghost cells with potential periodic boundary.

In the modified structure, the ghost cell are arranged in a specific order which is not definitely contiguous, for unstructured mesh in particular. However, it is better to consider contiguous variables to enhance efficiency of MPI communications between processors. A specific rearrangement of shared (i.e. global) variables are later introduced (see end of section 2.2) to fulfil this requirement.

II. Modification of the communication technique

In the original version, only extra cells (or information of the overlapping cells) are stored as global variables and shared between processors. Figure A.4 shows the SEND and RECEIVE (initial) procedure for processor $\#i$ having domain overlapping with processors $\#1$, $\#2$ and $\#3$.

At the beginning of any communication cycle, the information from the inner cells of processor $\#i$ are send to the overlapping cells (extra cells) of processors $\#1$, $\#2$ and $\#3$. Then, the overlapping cells of processor $\#i$ will receive from them information to update its own value.

As the overlapping cells are contiguous in the initial version (no periodic boundary conditions), the updating of extra cells is easy: we only need to know the initial location and size of the data to be transferred from local memory of other processors.

Individual Proc #i

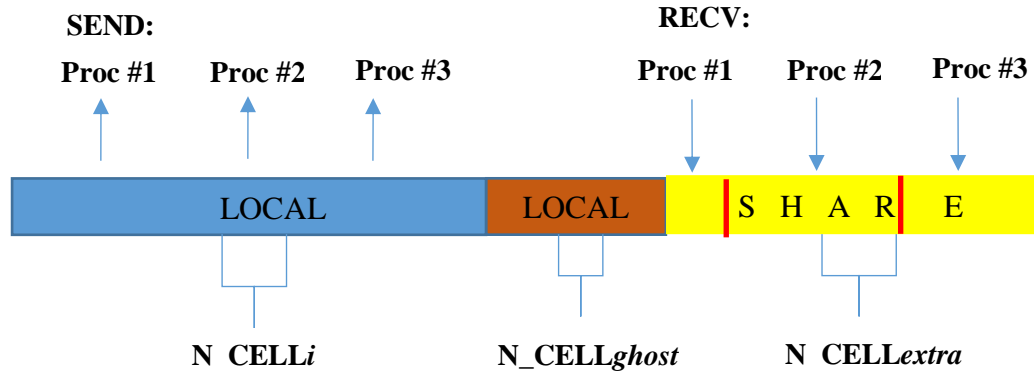


Figure A.4: Schematic of Communication in original NSMP3D.

In the modified NSMP3D (with periodic boundary conditions), the sending procedure is similar to the original code, but the received data also contains information of the ghost cells (Figure A.5).

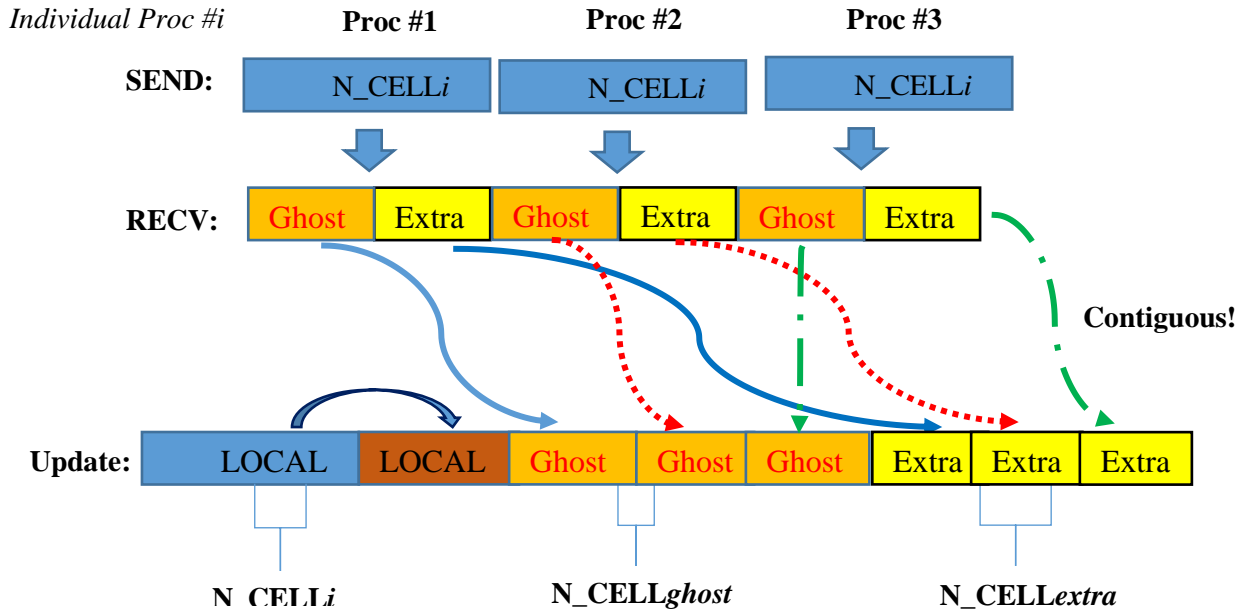


Figure A.5: Scheme plot of Communication process with periodic boundary condition.

The memory structure (Figure A.3) is rearranged into a contiguous array by grouping the global or shared information (coming from periodic or overlapping cells) and indexing the local position in original memory. During the SEND procedure, the global information (from ghost and extra cells) are packed and sent together. During the RECEIVE procedure, the transmitted data is first saved to a contiguous array, then split into ghost and extra cells in the named processor. Figure A.5 shows the structure of the contiguous array and the receiving process.

Appendix B.

Suspended load transport

The suspended load in an inclined channel with a slope of φ is studied. Monodisperse particles are transported by suspension leading to vertical profile of concentration in equilibrium between deposition and re-suspension (Figure B.1). The advection-diffusion model often solves it with a reference concentration given at a certain reference height. Empirical models of sediment entrainment usually give the reference concentration. Two entrainment models commonly used can be found in Van Rijn (1984) and Garcia and Parker (1991).

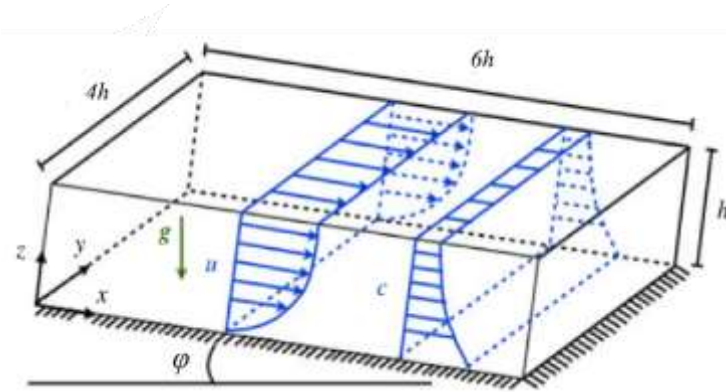


Figure B.1: Schematic representation of the model of a turbidity current. The model preserves the most essential features of turbidity currents, i.e. the flow is entirely driven by the suspended sediments and the settling of sediments self-stratifies the flow, from Shringarpure et al. (2012).

The flow is assumed to be entirely driven by the suspended sediments and the settling of sediments. The turbidity current is modelled in an inclined channel with a slope. The particle-laden flow is assumed to be dilute so that collision between sediment particles and rheology effects can be neglected, settling velocity is independent of concentration at the dilute limit, and Boussinesq approximation can be employed. Under these circumstances, the suspended flow is governed by continuous equation and the following equations:

$$\frac{\partial \mathbf{u}}{\partial t} + \mathbf{u} \cdot \nabla \mathbf{u} = -\frac{1}{\rho} \nabla p + \nu \nabla^2 \mathbf{u} + \frac{\rho_{mix} - \rho}{\rho} \mathbf{g}, \quad (\text{B.1})$$

$$\frac{\partial c}{\partial t} + (\mathbf{u} + \mathbf{V}) \cdot \nabla c = \mathfrak{D} \nabla^2 c, \quad (\text{B.2})$$

where c is the volumetric concentration of sediments, ρ is the density of water, $\rho_{mix} = (1-c)\rho + c\rho_s$ is the density of mixture and ρ_s is the density of the sediments. $\mathbf{u} = \{u_x, u_y, u_z\}$ is the velocity vector and $\mathbf{V} = \{V_x, 0, -V_z\}$ is the terminal settling velocity of an isolated sediment particle in a quiescent ambient, and \mathfrak{D} is the diffusivity of the sediment. Solid particles are assumed to be non-cohesive and large enough to consider them as non-Brownian particle. It is now well established that even such large particles effectively diffuse due to long-range hydrodynamic interactions mediated by particle number density fluctuations (Segrè et al., 2001; Mucha and Brenner, 2003). Thus, \mathfrak{D} is taken to be the effective constant diffusivity of the sediments. The diffusive term in (B.2) also provides a mechanism to re-suspend sediments from the bed (Garcia and Parker, 1993). The corresponding settling velocity for sediment diameters 70 μm and 120 μm are $V = 0.004\text{m/s}$ and $V = 0.01\text{m/s}$ (Parker, 2008).

I. Mean flow equations

The mean flow equations obtained by averaging the momentum and concentration equations over time and over two homogeneous direction (i.e. x, y direction), with substituting Reynolds decomposition $u = \bar{u} + u'$ and $c = \bar{c} + c'$. The ensemble-averaged quantities are only functions of the bed-normal z direction. According to Shringarpure et al. (2012), the mean momentum equations in x, z directions and concentration equation reduce to

$$\nu \frac{d^2 \bar{u}}{dz^2} - \frac{d(\overline{u'w'})}{dz} + R\bar{c}g_x = 0, \quad (\text{B.3})$$

$$\frac{d(\overline{w'w'})}{dz} + \frac{1}{\rho} \frac{d\bar{p}}{dz} + R\bar{c}g_z = 0, \quad (\text{B.4})$$

$$\mathfrak{D} \frac{d^2 \bar{c}}{dz^2} + V_z \frac{d\bar{c}}{dz} - \frac{d(\overline{c'w'})}{dz} = 0, \quad (\text{B.5})$$

where $R = (\rho_s - \rho) / \rho$. Integrating the above equations from the bottom to top boundary in z direction, the mean pressure distribution and the Reynolds stress $\overline{u'w'}$ is zero at the bottom boundary condition are respectively obtained by:

$$\bar{p} = -\rho \left(\overline{w'w'} \right) + \rho g_z \int_0^h R \bar{c} dz, \quad (\text{B.6})$$

$$\nu \frac{d\bar{u}}{dz} \Big|_{z_b} = R \bar{c} g_x, \quad (\text{B.7})$$

where \bar{p} is a relative averaged pressure to insure the incompressibility condition. According to Eq. (B.7), a velocity scale is defined as $u_\tau = \sqrt{R g_x \bar{c}^{(v)} h}$, where $\bar{c}^{(v)} = \frac{1}{h} \int_0^h \bar{c}(z) dz$.

According to the work by Geyer (1993), turbulent sediment fluxes can be approximated as

$$-\left(\overline{c'w'} \right) = \mathfrak{D}_t \frac{d\bar{c}}{dz}, \quad (\text{B.8})$$

Where $\mathfrak{D}_t = \kappa u_\tau z (1 - z/h)$ the turbulent diffusivity, and κ is the constant in the velocity log law. Eq. (B.5) can be integrated to the Rouse equation (Rouse, 1937):

$$\frac{\bar{c}}{\bar{c}_a} = \left(\frac{h-z}{z} \frac{a}{h-a} \right)^\zeta, \quad (\text{B.9})$$

where ζ is Rouse number given by $\zeta = \frac{V_z}{\beta \kappa u_*}$, \bar{c}_a is the mean sediment concentration at a conventional elevation a . Normally the sediment reference concentration is taken at $a = 0.05h$, h is the total depth of the channel, where the top of the bed load layer is assumed.

II. Non-dimensional equations

Three scales are employed to define dimensionless variables: velocity u_τ , channel depth h , $\bar{c}^{(v)}$ for concentration of sediments, and ρu_τ^2 for pressure. The dimensionless equations for Eqs. (B.1)- (B.2) are

$$\frac{\partial \tilde{\mathbf{u}}}{\partial t} + \tilde{\mathbf{u}} \cdot \nabla \tilde{\mathbf{u}} = -\nabla \tilde{p} + \frac{1}{\text{Re}_\tau} \nabla^2 \tilde{\mathbf{u}} + \tilde{c} \mathbf{e}_g, \quad (\text{B.10})$$

$$\frac{\partial \tilde{c}}{\partial t} + (\tilde{\mathbf{u}} + V) \cdot \nabla \tilde{c} = \frac{1}{\text{Re}_\tau S_c} \nabla^2 \tilde{c}, \quad (\text{B.11})$$

where $Re_\tau = \frac{u_\tau h}{\nu}$, $\mathbf{e}_g = \{1, 0, -g_z/g_x\}$, S_c is Schmidt number, defined as $S_c = \nu/\mathcal{D}$, where $\tilde{\cdot}$ is the non-dimensional variable. Based on the findings of Necker et al. (2005) and Cantero et al. (2008), the simulation results of turbidity currents are insensitive to the precise values of Schmidt number as long as it's $O(1)$, the present simulations employ $S_c = 1$.

It is not possible for the finite-sized sediments to stay in suspension without the presence of turbulent mixing and turbulent sediment resuspension from the bed. The laminar flow is assumed to be one-dimensional, steady and uniform. This means that $\tilde{v} = \tilde{w} = 0$, $\partial/\partial \tilde{t} = \partial/\partial \tilde{x} = \partial/\partial \tilde{y} = 0$. In this case the above governing equation simplify to

$$\frac{d^2 \tilde{u}}{d\tilde{z}^2} = -Re_\tau \tilde{c}, \quad \tilde{V}_z \frac{d\tilde{c}}{d\tilde{z}} = \frac{1}{Re_\tau S_c} \frac{d^2 \tilde{c}}{d\tilde{z}^2}. \quad (\text{B.12})$$

Integrating this with boundary condition yields $\tilde{c} = A \exp(-\tilde{V}_z Re_\tau S_c \tilde{z})$ and the system is closed with the criterion $\int_0^1 \tilde{c} d\tilde{z} = 1$. As pointed by Shringarpure et al. (2012), in the limited case of very large settling velocity, i.e. $\tilde{V} \rightarrow \infty$, the sediments settle to the bottom and the concentration profile is given by a Dirac delta function located at $\tilde{z} \rightarrow 0_+$ and at the same time maximum velocity $\tilde{u}_{\max} \rightarrow 0$. Therefore, the flow ceases to exist. Figure B.2 shows the laminar velocity for $\tilde{V} = 0.0265$, $Re_\tau = 395$ and $S_c = 1$ (Case 7).

III. Computational conditions

In this simulation, the initial condition for fluid field is extracted from turbulent channel flow with friction Reynolds number as $Re_\tau = 395$. Large eddy simulation with $64 \times 64 \times 64$ mesh is conducted until the non-dimensional simulation time $t = 60$, to be the initial velocity and pressure fields. A uniform concentration $c = 1.0$ distributed within the whole channel is used as the initial condition for suspended solid field, as that has been used in the reference. Neumann boundary conditions are used in both top and bottom surface for concentration.

Table B.1 List of the parameters in the simulation.

	V_z	β	\tilde{c}_b	\tilde{c}_t	κ	B
Case 1	0.0	-	1.0	1.0	0.41	7.6
Case 2	0.0048	-	0.993	1.012	0.405	7.5
Case 3	0.005	0.6	0.908	1.138	0.355	5.9
Case 4	0.01	0.63	0.799	1.306	0.335	5.3

Case 5	0.02	0.85	0.511	1.811	0.300	4.4
Case 6	0.026	0.9	0.260	2.505	0.250	2.9
Case 7	0.0265	0.58	0.196	3.013	0.230	2.4

Note: V_z is dimensionless settling velocity of the sediments, \tilde{C}_b and \tilde{C}_t are the dimensionless mean volume concentration of sediments at the bed and the top boundary, and κ (Von Karman variables) and B are the best fit constants for the velocity log law. β is the parameter from Rouse profile.

Table B.1 lists all the different simulations analysed in this work to address the mechanism of turbulence damping in turbidity currents. Six different cases of stratified flows are considered. Cases 2–7 correspond to the simulations where the settling velocity of sediments is increased from $V_z = 0.48 \times 10^{-2}$ to $V_z = 2.65 \times 10^{-2}$. Case 1 with $V_z = 0$, is the reference case, since its solution corresponds to turbulent channel flow driven by a uniform body force. The corresponding velocity profile is shown in Figure B.2 (the group of green triangles), and in wall units. A very good agreement is observed regarding to the wall law ($u^+ = z^+$) for $z^+ < 5$, and with a slightly over-predicted mean velocity in the region of the log law for $z^+ > 30$.

IV. Mean values and turbulent flux in the stratified flows

Figure B.2 presents the velocity profiles on log-linear scales. The logarithmic law of the wall $u^+ = 1/\kappa \log(z^+) + B$ for case 0 and 5 with adjusted constants is also included in this figure. The best-fit values of κ and B for all cases are listed in Table B.1. The velocity profiles for cases 1–6 show a definite turbulent nature with a definite logarithmic region for $z^+ > 30$. The deviation from the fully turbulent logarithmic law (case 1) is only in terms of the constant values. This change in the constants can be attributed to the damping of turbulence because of stratification (Cantero et al., 2009). Case 7, on the other hand, does not display a logarithmic region. Figure B.2 also shows the laminar solution computed for the same set of parameters used for case 7.

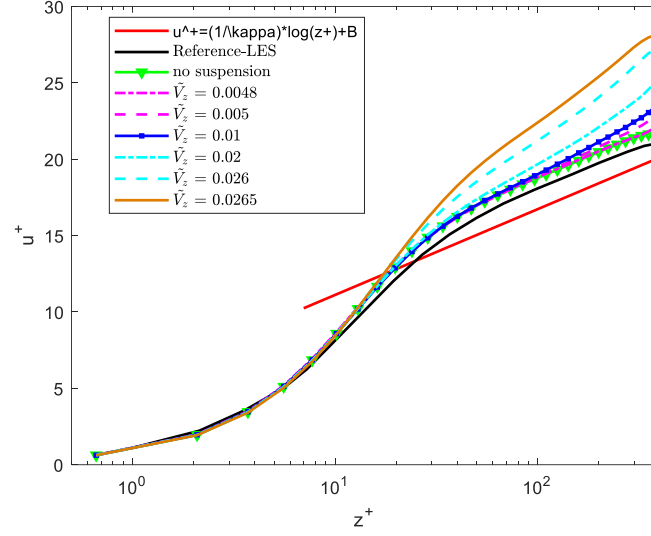
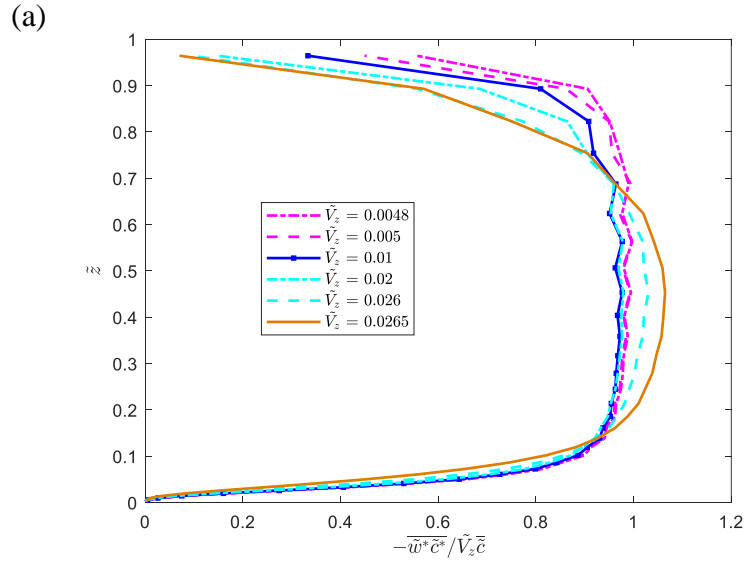


Figure B.2: Mean velocity profiles in wall units. The red color corresponds to log law.

The balance between the settling flux of sediments $V_z \bar{c}$ and turbulent flux of sediments $(\overline{\tilde{w}'\tilde{c}'})$ can be obtained from Eq.(B.11) as

$$\tilde{V}_z \bar{c} = \overline{\tilde{w}'\tilde{c}'} - \frac{1}{\text{Re}_\tau S_c} \frac{d\bar{c}}{d\tilde{z}}. \quad (\text{B.13})$$



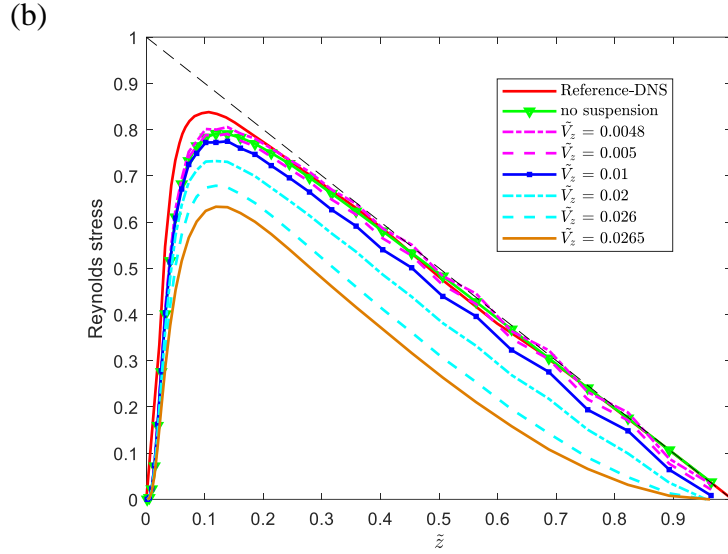


Figure B.3: (a) Profiles of the ratio of sediment turbulent flux to settling flux (b) profiles of Reynolds stress.

The settling flux of sediments will increase when settling velocity increases. In order to keep the sediments well mixed in the flow ($d\tilde{c}/d\tilde{z} \approx 0$), there must be a proportional increase in the turbulent flux of sediments. In other words, in a well mixed channel the ratio of turbulent flux to settling flux of sediments approaches 1. The relative importance of turbulent flux of sediments can be seen in Figure B.3(a), which shows the variation of the ratio of turbulent flux to settling flux in the bed-normal direction. From Figure B.3(a) it is evident that the increase in turbulent flux is not proportion to settling flux for all the cases. This ratio shows a decreasing trend with increasing settling velocity of sediments. In addition, the decrease is not uniform throughout the channel: it is more pronounced near the top boundary than near the bed. This asymmetry is due to reduction of turbulent transport from near the bed, where turbulence production occurs, to the upper part of the channel. Figure B.3(b) shows profiles of the Reynolds stress $-\overline{u'v'}$ for cases 1-5. The small reduction in Reynolds stress with increasing settling velocity of sediments suggests that the effect of stratification is weak. The corresponding DNS results of Kim et al. (1987) for pure channel flow are also shown in this figure. The good enough agreement between our results and the DNS ones, for no suspension case using coarse mesh serves as validation of the simulation procedure and the grid resolution employed in this work.

Turbulent intensity velocity fluctuations are shown in Figure B.4. The variation of all *r.m.s.* velocity fluctuations becomes smaller for case 1 to case 7. Thus, the stratification

effects successful suppress the wall-normal and spanwise velocity fluctuations, and thereby all momentum and mass transport in wall-normal and spanwise directions.

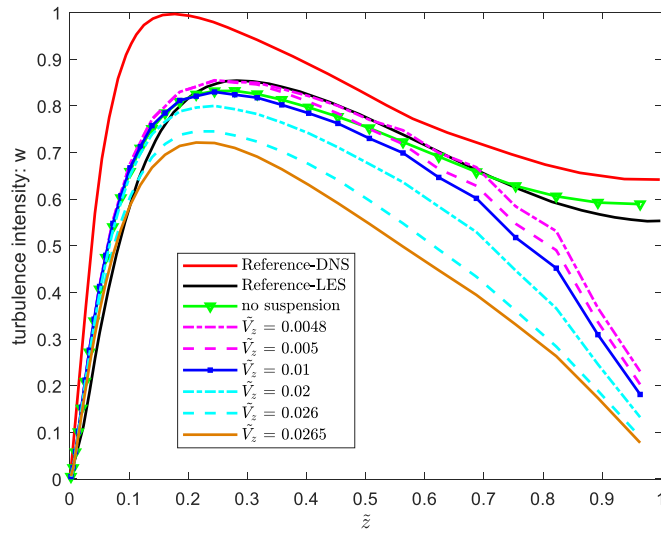
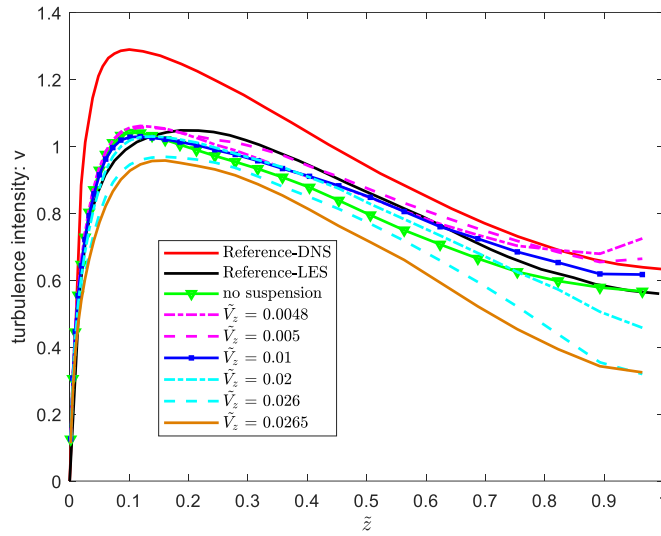
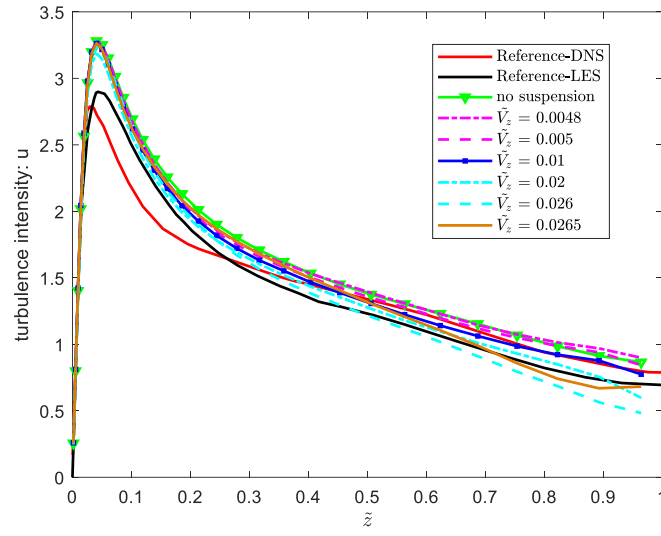
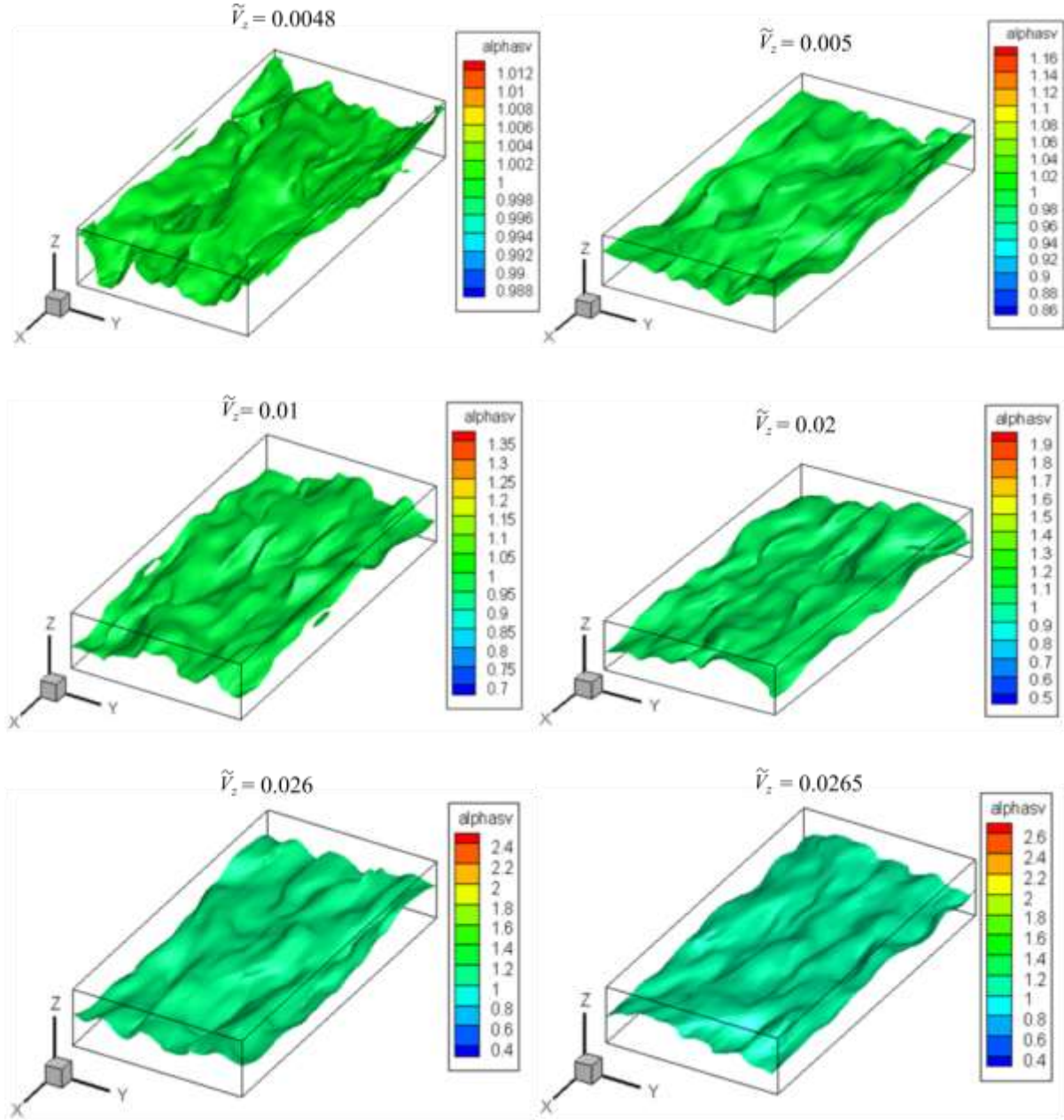


Figure B.4: Turbulence intensity: (a) u_{rms} ; (b) v_{rms} ; (c) w_{rms} .Figure B.5: Sediment concentration surface at middle value ($\bar{c} = 1.0$).

Sediment concentration iso-surfaces at middle value ($\bar{c} = 1.0$) are shown in Figure B.5 and the mean concentration profiles of the selected cases given in Table B.1 are shown in Figure B.6. As the settling velocity of sediments increases, the resulting concentration profile increasingly deviates from the reference profile $\bar{c} = 1.0$. The resulting non-uniform mean concentration of sediments is skewed towards the bed, which affects the flow in two ways. First, the streamwise driving force is also correspondingly skewed towards the bed. Second, the stable stratification induced by concentration gradients tends to dampen turbulence. The

effect of a skewed driving force is not so strong, and the stratification effect is the dominant mechanism responsible for complete turbulence suppression. All the cases show a well-mixed concentration profile, compared with their corresponding Rouse profiles (B.9). Rouse profile is an approximation for the concentration profile achieved by characterising the turbulent mixing term in Eq.(B.5) by eddy diffusivity. Rouse profiles here are evaluated using the modified von Karman constant given in Table B.1. This quantifies the effect of stratification on the turbulent mixing in the channel. From the figure it is clear that when $V_z=0.02$ and $V_z=0.026$, our simulations are closer to Rouse profile with β closer to 1, while the other cases over-predict the turbulent mixing in stratified flows, leading to fuller concentration profiles.

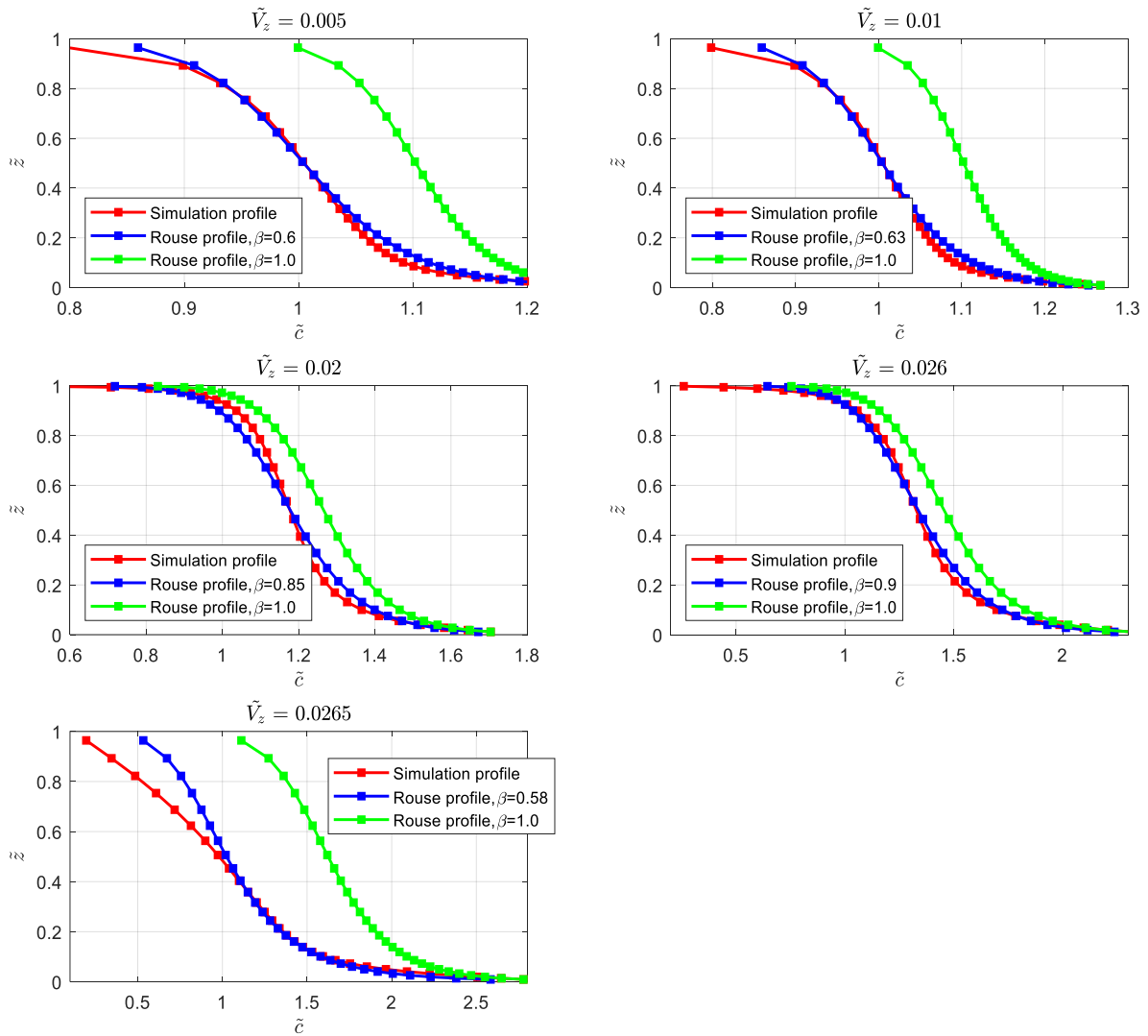


Figure B.6: Sediment concentration profile.

Figure B.7 plots of streamwise velocity (\tilde{u}'), bed-normal velocity (\tilde{w}') and concentration (\tilde{c}') fluctuations for cases 6 ($V_z=0.026$) in the x - y (streamwise–spanwise) plane at $z^+\approx 12$, where maximum turbulent kinetic energy production and maximum Reynolds stress happens.

The plots of concentration and streamwise velocity fluctuations show long streamwise aligned streaky structures in both cases. It can be observed that \tilde{u}' and \tilde{c}' distributions are negatively correlated. In other words, the sediment concentration is higher (lower) along the low-speed (high-speed) streaks. The bed-normal velocity fluctuations are also well correlated with the streamwise velocity and concentration fluctuations. But since \tilde{w}' does not show a long streaky structure, the correlation is not as obvious. In the concentration contours, the regions of positive large values are long and spread over the entire plane.

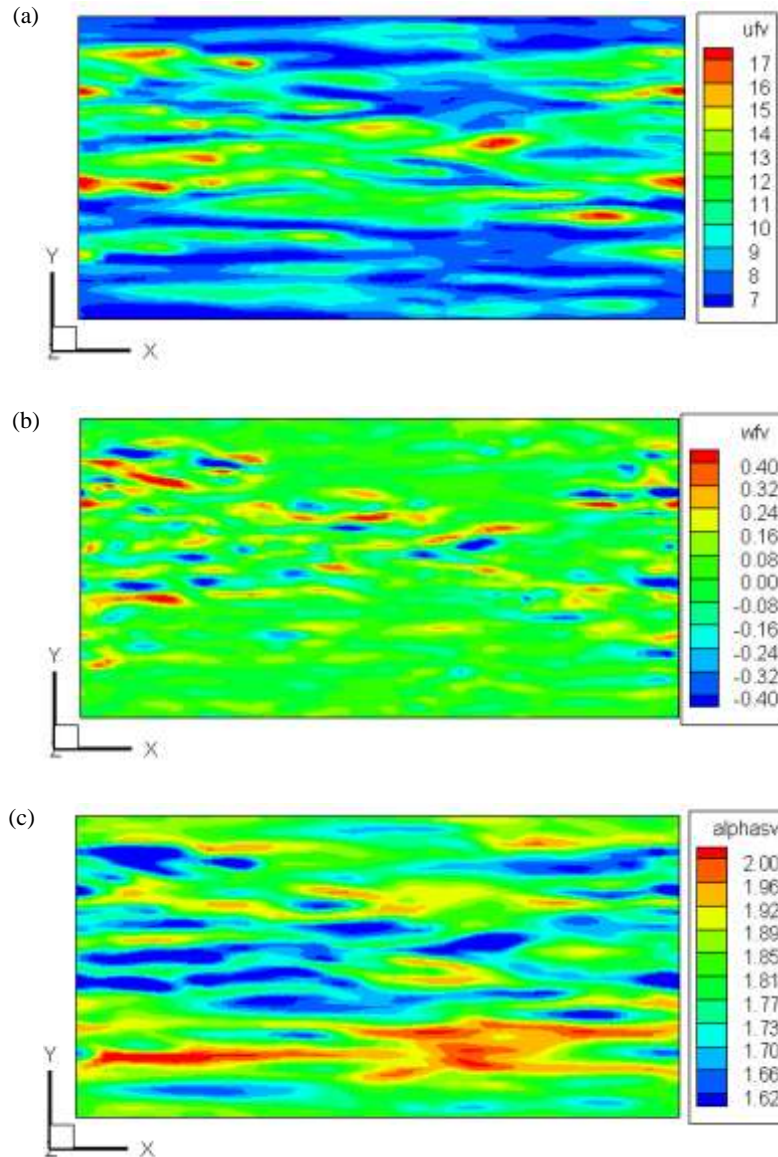


Figure B.7: (a) Streamwise velocity fluctuations. (b) Bed-normal velocity fluctuations. (c) Fluctuations in the concentration of sediment. Results for case 6 ($v_z=0.026$) at $z^+\approx 12$.

Figure B.8 shows iso-surfaces of Q criterion for cases 3 and 6, presenting the vertical structures of the turbulent flow at a selected time instant. Both cases show a dense

distribution of tube-like and inclined quasi-streamwise vortices in the flow. With increasing settling velocity, the stratification of the flow increases and the structures become sparse, showing the turbulence suppression. A substantial decrease in the density of the structures is seen but the flow remains turbulent. This implies that some of the existing structures in the flow are intense enough to spawn the next generation of structures to sustain turbulence.

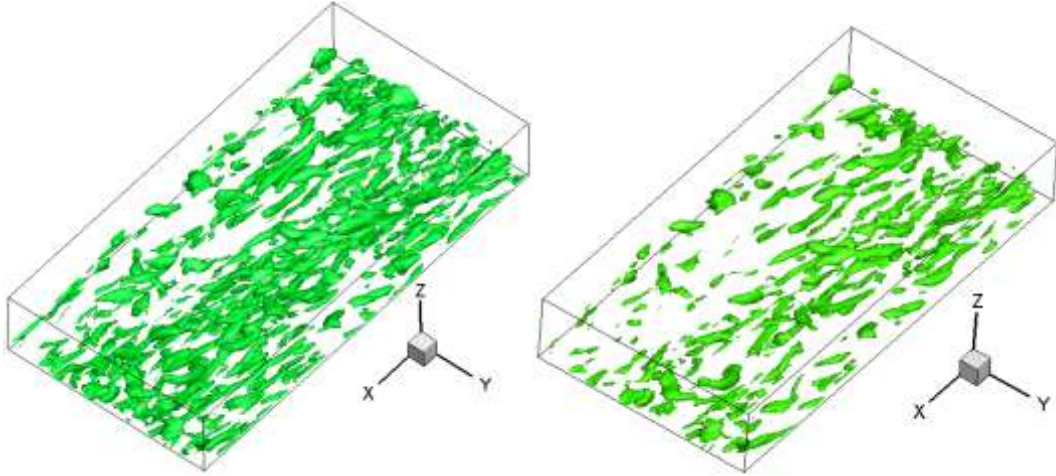


Figure B.8: Iso-surface of $Q = 400$ for case 3 ($v_z = 0.005$) and case 6 ($v_z = 0.026$).

The vertical profiles of velocity computed by NSMP3D from turbulent channel flows using DNS and LES are in a good agreement with previous studies, which permits simulations of non-hydrostatic flows at moderate Reynolds numbers.

Dilute turbidity currents driven by suspension of sediments in an inclined channel flow are modelled. The suspended sediments under the influence of gravity drive the flow in the channel and simultaneously settle towards the bed. The interaction of sediments and turbulence lead to (i) skewing of the streamwise driving force towards the bed, and (ii) stable stratification that damps bed-normal momentum and mass transport. Several simulations using NSMP3D were carried out to understand the two effects and their role in turbulence suppression.

Stratification is the manifestation of the balance between turbulent mixing and the settling of the sediments. With increasing the settling velocity, flow turbulence is less able to keep the sediments in suspension, and the flow in the channel tends towards the laminar solution, which is clearly shown by the mean velocity and mean concentration profiles.

Appendix C.

Thesis-related published and
revised papers